PRECISE EARTHQUAKE SOURCE PARAMETER ESTIMATION

A DISSERTATION

SUBMITTED TO THE DEPARTMENT OF GEOPHYSICS

AND THE COMMITTEE ON GRADUATE STUDIES

OF STANFORD UNIVERSITY

IN PARTIAL FULFILLMENT OF THE REQUIREMENTS

FOR THE DEGREE OF DOCTOR OF PHILOSOPHY

Annemarie Susan Baltay

December 2011

This dissertation is online at: http://purl.stanford.edu/gg510rh4255

I certify that I have read this dissertation and that, in my opinion, it is fully adequate in scope and quality as a dissertation for the degree of Doctor of Philosophy.

Gregory Beroza, Primary Adviser

I certify that I have read this dissertation and that, in my opinion, it is fully adequate in scope and quality as a dissertation for the degree of Doctor of Philosophy.

Mark Zoback, Co-Adviser

I certify that I have read this dissertation and that, in my opinion, it is fully adequate in scope and quality as a dissertation for the degree of Doctor of Philosophy.

Eric Dunham

I certify that I have read this dissertation and that, in my opinion, it is fully adequate in scope and quality as a dissertation for the degree of Doctor of Philosophy.

Thomas Hanks

Approved for the Stanford University Committee on Graduate Studies.

Patricia J. Gumport, Vice Provost Graduate Education

This signature page was generated electronically upon submission of this dissertation in electronic format. An original signed hard copy of the signature page is on file in University Archives.

Abstract

The question of whether earthquakes, as they increase in size, radiate seismic waves more efficiently is at the core of our understanding of the physics of faulting, as well as our ability to mitigate the effects of strong ground motion. If earthquakes have some intrinsic time or length scale that could be observed or modeled, then seismologists could determine the ultimate size of an earthquake just as it begins to rupture. On the other hand, if earthquakes are self-similar, with no intrinsic time or length scale, than any information learned about the plethora of small and intermediate earthquakes can simply be scaled up to predict parameters, such as ground motion, for larger, more devastating earthquakes.

Many studies find that apparent stress and stress drop increase with seismic moment, yet others find an independence of these parameters with moment, obeying self-similar earthquake source physics. Source measurements are controversial due to the inherent difficulty in correcting the radiated waves to negate path and site effects, such as attenuation, scattering or amplification. Independent studies of the same earthquake may find seismic energies that differ by an order of magnitude. Methods to estimate source parameters need to account for these effects, or quantify the range of validity for estimates made with uncorrected seismic records.

In this work, I precisely estimate the source parameters radiated seismic energy, apparent stress and stress drop, using both relative spectral measures from empirical Green's functions, and close distance acceleration records.

Using relative empirical Green's functions, I can handily negate source and path effects, without explicit consideration of anelastic attenuation. Working with data from 8 sequences of earthquakes in the western US and Honshu, Japan, ranging from *M 1.8* to M_w *7.1*, I find no clear trend of a dependence of apparent stress or stress drop with moment, finding a constant scaled energy, E_R/M_o of 3.5×10^{-5}, or apparent stress of ~ 1 MPa, to fit the data well. The average Brune stress drop for these data is ~5 MPa. By using many stations and relative measures, I statistically show self-similar earthquake scaling. However, there are anomalous enervated and energetic events that show individual departure from the overall trend, representing the true variability in earthquake source parameters.

I revisit the a_{RMS} stress drop using recent broadband stations and strong motion accelerometers. The a_{RMS} stress drop samples an inherently different portion of the earthquake spectrum than the Brune stress drop, and can be directly related to *PGA* and hence high-frequency ground motion. While the a_{RMS} stress drop is much simpler and faster to measure, it does not model attenuation, and hence suffers from loss of signal at distances > ~20 km. At close stations, and for large earthquakes, the a_{RMS} stress drop values are very similar to those of the Brune stress drop, yet with reduced error base on corner frequency uncertainty. That the a_{RMS} method yields stable stress drops supports the assumptions behind the formulation: that earthquake acceleration records can be considered random, band-limited, white Gaussian noise, and overall, a self-similar earthquake model.

The last portion of this work focuses on five great earthquakes, $M_w > 8.5$, over the past 7 years. Because they are so rare, seismologists don't have much information about these devastating events. Understanding how they relate to smaller earthquakes will aid in hazard mitigation. I estimate the radiated seismic energy and apparent stress, using a novel, teleseismic empirical Green's function deconvolution. At near distances, great

earthquake are too big to model, as effects from one end of the rupture will interfere with those from other parts, and local recordings are often saturated. But at far distances, ~3000 km – 9000 km, I show that moderate earthquakes, M_w *6.5 – 7.5* can be used as Green's functions, and are used to correct the mainshocks from path and site effects. Use of several different eGf earthquakes demonstrates the limitations on the method, but also increases the precision of the energy estimates. I find that both *P* and *S* waves give consistent energy estimates when using eGf events. Azimuthal dependence of radiated energy indicates expected rupture directivity, and can be modeled using Haskell line sources to understand the rupture process.

Acknowledgments

I would foremost like to thank Greg for being an amazing advisor. He continually turns what I fear is a bad result into something inspiring, and I always leave his office excited to run back upstairs and try a new idea. At the same time he encourages me to work hard, yet enjoy my time in graduate school, and I can't imagine having worked on a PhD with any other advisor.

I also thank my committee members. Mark Zoback has attended nearly all of my committee meetings and qualifying exam from the beginning, and always offers genuine suggestions, looking beyond the minute details of the analysis to bring me back to the bigger picture. I'm very glad that Eric Dunham started up a series of seminars to help me explore some of the more theoretical background of my research. Tom Hanks has been really fun to work with, and taught me to check everything with your intuition, and not rely on what the computer might tell you. Also thanks to Jesse Lawrence and Paul Segall who occasionally sat on my committee and offered a few very key suggestions, which turned into central figures.

I've also benefitted from very encouraging co-authors. German Prieto pulled me through the details of my first project, especially when I thought nothing was ever going to work, and without him I would still be completely lost sometimes. It was a joy to visit Satoshi Ide at the University of Tokyo, and I am always amazed by his attenuation to detail and to those he works with.

All the folks at the USGS have shown continual interest in my budding seismological curiosities, continually giving me encouragement in my work, and I've enjoyed all the chances to chat in Menlo Park. Participating in PEER meetings at Berkeley have been exciting, and I always hope that something I say will be implemented in a building code. Everyone with whom I worked one summer at RMS was positive and supportive, even though I was only there for the summer, and helped to put all of our scientific work into perspective, and also aided me in taking a break for a summer to hang out in Newark and get a taste of corporate life. I'm also grateful to the other students and researchers at Todai and ERI who helped to make my stay in Tokyo rewarding both scientifically and culturally.

No one ever said working on a PhD would be easy, but it was certainly made more painless and fun with the help of the geophysics department, especially Mitchell 4th floor and my awesome office mates. Pretty much any programming problem could be fixed by someone on the 4th floor, and it was great to have people to always bounce ideas off of, whether about an algorithm, a conceptual idea, or the color scheme for a figure. I'd especially like to thank the earthquake seismology group, for fun outings and group lunches; for being available for commiseration; and for getting really excited about earthquakes. I definitely wouldn't have made it through 5+ years at Stanford without Justin, for scientific collaboration and as a partner in crime outside of the office. Thanks for putting up with my quirks!

In addition, all my friends at Stanford outside of the department helped me enjoy the nights, weekends, and the occasional skip day. I've grown so much as a person while at Stanford, encouraged on by all the amazing people around me. It's always been fun to come home to my roommates, and they've been very tolerant of my cooking experiments. I've loved it all, and won't forget any of the parties, trips or adventures.

My family has always been my support network, including my brothers and their families. Spending time with them always reminds me that there is so much more to life than work, and they are always up for something zany. My parents have been my cheer leaders, my pit crew, and my role models. I know I can always look to them for advice,

help, or support, with absolutely anything. I honestly wouldn't be finishing a PhD right now if it weren't for my mom and dad.

Lastly, I'd like to thank Eric for being my companion through all of this, supporting me when I'm at my wits end, celebrating a good result, or just distracting me on a weeknight. He's taught me how to really enjoy California; I'm really grateful every time I'm dragged to the top of yet another peak; excited whenever we pull into a charming old town; and always anxious to be skiing down The Wall next to Eric. I look forward to so many more adventures together.

Contents

List of Tables

List of Figures

CHAPTER 1

Introduction

Earthquakes are natural hazards that can cause huge loss of life and much property damage. Seismologists are tasked with understanding earthquakes to ultimately reduce the risk associated them, be it from strong ground motion or tsunami generation. Approximately one magnitude 8 or larger event, a great earthquake, occurs every year. For the casual observer this may sound like a large number; however due to the varied tectonic setting of earthquakes and the inconsistent coverage of seismic networks, we still do not completely understand how large earthquakes start, grow, or arrest, or just how big their ground motion will be. In order to determine how damaging a very large earthquake may be, we need to analyze the more abundant recordings of small to moderate earthquakes and relate those findings to great earthquakes.

So, is a great earthquake of magnitude ~9 simply a large version of a magnitude 3 earthquake? Or are there inherent differences in the underlying parameters of earthquakes, so that the physical processes of large earthquakes are intrinsically different? The question of whether or not earthquakes, as they increase in size, have fundamentally different physical behavior is at the core of our understanding the physics of faulting as well as our ability to mitigate the effects of strong ground motion, and is the basis of this thesis.

The seismic moment, M_o, is the most elementary measure of the size of an earthquake. *Aki* [1966] defined seismic moment as the product of the shear modulus, area of rupture, the average slip during the event: $M_o=\mu A\bar{D}$, but in practice is determined from the zero-frequency asymptote of the displacement source spectra. The moment magnitude, $M_w=(log_{10}\ M_o - 9.05)/1.5$, is the only magnitude scale which does not saturate due to deconstructive interference at large magnitudes, unlike all of the previous magnitudes (eg. M_L, M_s, m_b) [*Hanks and Kanamori*, 1979]. Although seismic moment is an excellent way to measure the overall size of an earthquake, it is a static measure and does not tell us anything about the dynamic processes occurring during faulting. In the extreme, a large slow slip event lasting for many days with no damage may be considered to have the same moment as a highly destructive strike slip earthquake with very large recorded accelerations [eg. *Kostoglodov et al,* 2007]. Radiated seismic energy and stress drop, however, are dynamic measures of the size of an earthquake. These parameters are directly related to earthquake ground motion and hazard, and also inform earthquake dynamics.

The seismic energy is only a fraction of the total potential energy released during an earthquake, however. Consider the energy budget of an earthquake. Long-term plate motions cause a buildup of strain energy (ΔW) across a fault, creating a potential energy source for the earthquake. When the rupture occurs, energy is expended as fracture energy (E_G), the energy needed to initiate and propagate shear failure; frictional energy, E_F, the energy dissipated as heat; and radiated seismic energy, E_R, the broadband energy that is radiated through waves. Thus,

$$\Delta W=E_G+E_F+E_R. \quad (1)$$

Figure 1.1, modeled after that of *Kanamori and Venkataraman* [2004], graphically illustrates the balance of energy in an earthquake. During the relaxation of built up stresses, the resisting stress, σ_f, shown as the thick black line, varies with slip. The shear stress on a fault drops from the initial level, σ_o, to a final stress of σ_1 as slip proceeds to some critical value D_c. This is considered the static stress drop, $\Delta\sigma$, or Brune stress drop [*Brune,* 1970]. In the model on the left, considered the Orowan case, the stress drop

occurs instantaneously, and the fracture energy, $E_G=0$ [*Orowan,* 1960]. The second, perhaps more realistic case, describes earthquakes more generally. The resisting stress drops to the final value, σ_1 as the rupture progresses, over some critical length D_c. The fracture energy is then not zero, and the radiated energy is less than of that in the first case.

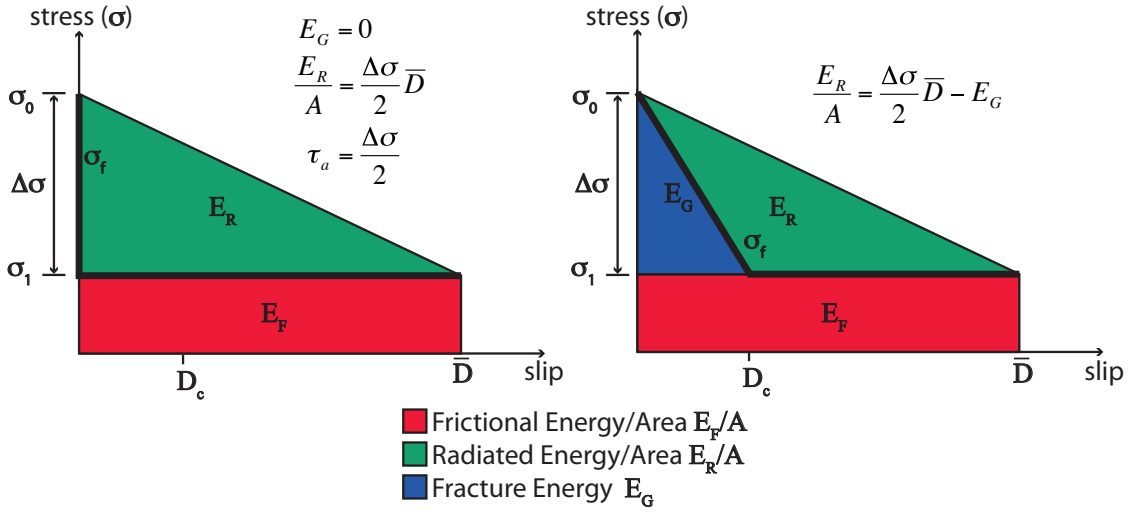

Figure 1.1 Two models of earthquake rupture, showing stress vs. slip. The thick black line is the resisting stress, σ_f. The left model is a simple case in which the resisting stress falls instantaneously, and the fracture energy E_G =0, the Orowan model (*Orowan,* 1960). The right is the more general case in which the resisting stress falls to the final value as slip increases to D_c, the critical slip length.

Constraints on this energy balance may come from a magnitude dependence on E_R or E_G. If the energy needed to initiate shear fracture, E_G, is the same for all earthquakes, then a small earthquake may use a large portion of its total ΔW to initiate failure, radiating proportionally less E_R. By contrast, a large earthquake may use a smaller fraction of its total energy on failure, more efficiently radiating seismic wave energy. Other processes may have an effect on the fracture energy, such as weakening or melting. Fracture energy can be tied to the macroscopic parameters, such as radiated energy and stress drop, to determine microscopic parameters, such as the critical length scale, or any weakening processes.

Earthquake self-similarity means that there is no intrinsic length or time scale of earthquake physics; the phenomenon appears the same when scaled with space and time. Then stress drop and apparent stress, $\mu E_R/M_o$, the shear modulus times the ratio of

radiated energy to moment, are constant, with some inherent variability, for all earthquakes, and any source information we can estimate from the plethora of smaller earthquakes can be scaled up for great earthquakes, for which we have much less data. Ground motion predictions for large, hazardous events, could be understood from recorded ground motion of many smaller earthquakes.

On the other hand, if earthquakes are not self-similar, this would be diagnostic of a characteristic length scale. Imagine that a larger earthquake more effectively radiates energy. Then, a bigger, more destructive event may be distinguishable from its smaller kin from the onset of the rupture, an appealing idea for obvious reasons. If, at the point of nucleation it could be determined that an event was a magnitude 8, rather than a much smaller earthquake, risk could be mitigated through the use of early warning systems. Understanding the relationship between seismic moment, radiated energy and stresses can help seismologists to relate all earthquakes, small and large.

Seismic energy, E_R, is radiated by waves leaving the earthquake source, which travel through the earth and may be attenuated, amplified, scattered, or geometrically spread, before being recorded. E_R is the integral of the squared velocity seismogram, and most of the energy is concentrated near the spectral corner frequency, equal to the inverse of the faulting duration, of the earthquake.

$$E_R = \frac{1}{4\pi^2 \rho \beta^5} \int_0^\infty |\omega \cdot M(\omega)|^2 d\omega \tag{2}$$

The relationship between radiated seismic energy and moment has been controversial due to the difficulty in its measurement. Seismic waves are generated with strong angular variations at the source due to both the radiation pattern and source directivity. As these waves propagate they attenuate, scatter and focus/de-focus and are subject to strong frequency-dependent site effects in the near-surface. All of these factors influence wave amplitude, and because they are difficult to correct for accurately, independent studies of the same earthquake may find seismic energies that differ by an order of magnitude [*Singh and Ordaz*, 1994].

Many studies have found that the apparent stress varies systematically with earthquake size, in violation of self-similar physics [e.g., *Kanamori et al*, 1993; *Abercrombie*, 1995; *Mayeda and Walter*, 1996; *Mori et al*., 2003; *Walter et al*., 2006]. On the other hand, other researchers find a magnitude-independent value of apparent stress across many orders of moment [e.g., *Choy and Boatwright*, 1995; *Ide and Beroza*, 2001; *Prieto et al*., 2004; *Yamada et al.,* 2007]. While stress drop has been found to be variable between earthquakes, it is generally accepted that it is a constant within a range of 1 – 10 MPa, with a lower limit of ~0.1 MPa and upper limit near 100 MPa, and not dependent on magnitude [e.g. *Thatcher and Hanks,* 1973; *Kanamori and Anderson,* 1975; *Hanks*, 1977; *Allmann and Shearer,* 2009].

The seismogram measured at a station is a convolution of the earthquake source, the effects of the path traveled through the earth, and any local site or instrument effects. To accurately measure earthquake source parameters, only source information should be analyzed. Instrumental effects are documented and easily removed; path and site effects need to be negated. Typically, path corrections have been made assuming an earth structure, and correcting records for attenuation and spreading [e.g. *Boatwright and Choy,* 1986; *Convers and Newman*, 2011]. Another method makes use of co-located earthquakes, close enough so that they share common path and site effects. Small earthquakes can be assumed to be point sources, or empirical Green's functions, and can be deconvolved from the larger earthquake of interest, to estimate the source function [e.g. *Hartzell,* 1978; *Hough,* 1997]. The eGf method is appealing, as explicit information about the attenuation structure of the earth is not necessary.

Brune stress drop, $\Delta\sigma$, can be measured in practice from the earthquake source size, either from actual source, or from waveform modeling. If earthquakes are considered circular cracks, the radius $r = \frac{2.34\beta}{2\pi f_c}$, where the corner frequency $f_c=1/T_d$, the faulting duration, and β is the shear wave velocity [*Brune,* 1970].

$$\Delta\sigma = \frac{7M_o}{16}\left(\frac{2\pi f_c}{2.34\beta}\right)^3 \tag{3}$$

With this model, a constant stress drop implies a trade-off of M_o with f_c^3. In practice, corner frequency is measured, often with some uncertainty, from the corrected source spectra. Because the Brune stress drop is dependent on f_c^3, stress drops can be highly variable [e.g. *Sonley and Abercrombie*, 2006]. *Hanks* [1979] developed another representation of the stress drop, dependent only on the high frequency RMS acceleration record of earthquakes, based on the knowledge that acceleration time histories are random, Gaussian white noise in the frequency band higher than the corner frequency.

$$\Delta\sigma_{a_{RMS}} = a_{RMS}\frac{106\rho R}{2R_{\theta\phi}(2\pi)^2\sqrt{2}}\sqrt{\frac{f_c}{f_{\max}}} \tag{4}$$

This a_{RMS} stress drop was quickly adopted for use as the "stress parameter" in many ground motion prediction equations in engineering [e.g. *Boore*, 1983]. One advantage of the a_{RMS} stress drop is that it is only dependent on the square root of f_c, so that uncertainties in corner frequency map into smaller uncertainties in stress drop. A second advantage is that the a_{RMS} is a computationally simple quantity to measure, and no corrections for path or site are necessary.

In this thesis, I make use of the empirical Green's function deconvolution to estimate source spectra, and then radiated energy, corner frequency, and stress drop. The main assumption is that a small earthquake can be considered an ideal point source, with an impulse, delta function source. Any difference from a delta function in that eGf, then, can be attributed to path effects as the waves from that event travel to a station. The eGf source function is deconvolved from the main, larger event of interest. Deconvolution in time is simply subtraction in log-log frequency space.

In reality, an empirical Green's function is not purely a delta function and actually has some width, T_d, the faulting duration. Hence its spectrum has a decay, which begins at the corner frequency, f_c equal to the inverse of the duration. *Brune* [1970] showed that far-field shear wave displacement spectra, *u(f)*, decay with a slope of ω^{-2},

$$u(f) = \frac{M_o}{1+(f/f_c)^2}. \tag{5}$$

This spectral model can be described by just the moment, M_o, and stress drop, or using Eq. 3, corner frequency.

Figure 1.2 illustrates ideal, self-similar Brune spectra and example earthquakes, for given magnitudes, assuming a constant stress drop of 3 MPa. The top shows ideal Brune displacement spectra, where the long period level is the moment, and the high frequencies decay as f^2. The corner frequency $f_c \sim M_o^{-1/3}$. Overlain in black are examples of three earthquakes studied in this thesis: Tohoku-Oki 2011 M_w *9.1*, Cerro Prieto 2008

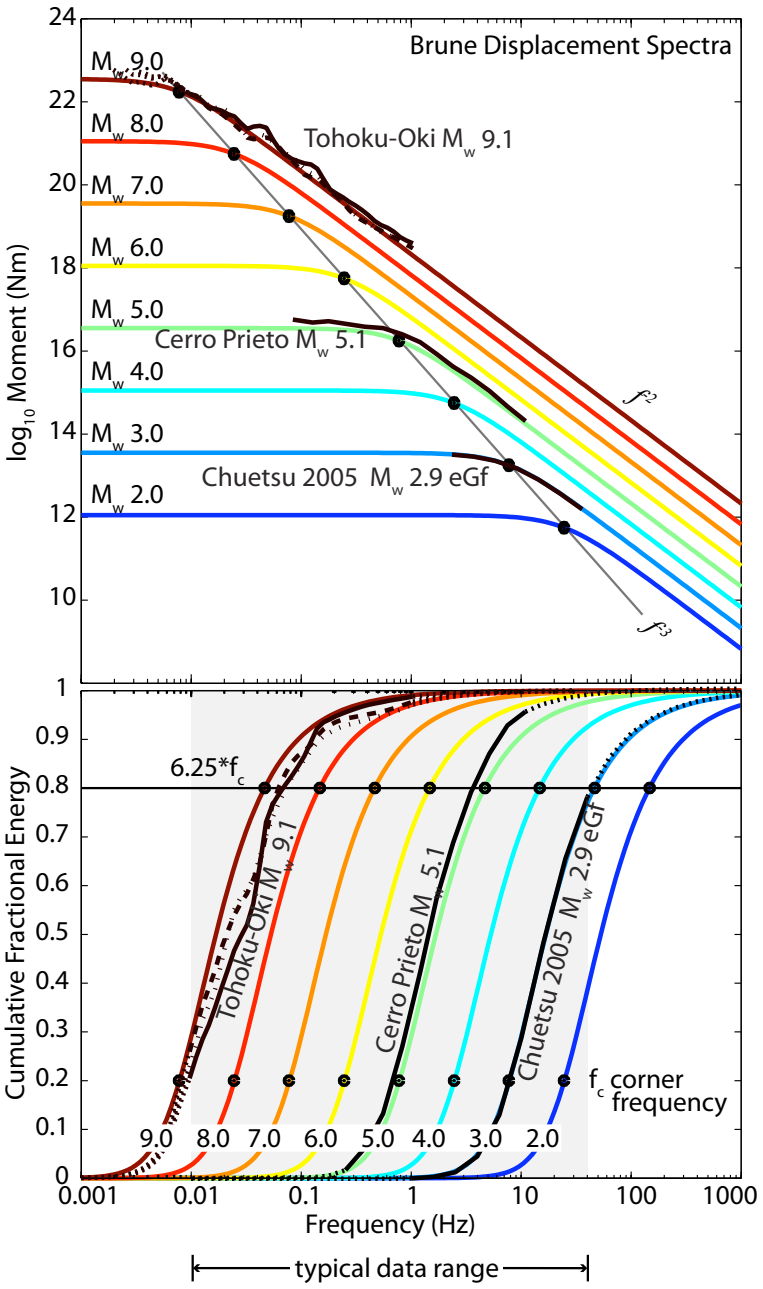

Figure 1.2 (top) Brune spectra for given magnitudes, assuming stress drop of 3 MPa. Overlain in black are three earthquakes studied in this thesis, showing their corrected spectra and modeled corner frequencies. Tohoku-Oki spectra are extrapolated into frequencies lower than 0.01 Hz, the lower data limit. (bottom) Ideal cumulative fractional energy, showing which frequencies contain energy for each magnitude earthquake. About 20% of the energy is contained below the corner frequency; 50% of the energy within 3.12 * f_c; and 80% within 6.25 * f_c. Typical instruments record up to 20 to 100 Hz; the upper frequency limit is the Nyquist, which is as small as 10 Hz, and up to 50 Hz in Japan. For the very large events, we are missing information in the lower frequencies, making corner frequency determination difficult. It is apparent that even small deviations away from ideally Brune can cause larger effects on the ideal cumulative energy, as witnessed by the Tohoku-Oki and Cerro Prieto events, which are very Brune-like in the top plot.

M_w *5.1*, and the M_w *2.9* eGf event used in the Chuetsu 2004 analysis. Radiated energy is measured from the square of the velocity spectrum, and corner frequency is fit

assuming a Brune shape. The bottom plot is the cumulative fractional energy, illustrating which frequencies contribute to the total radiated energy. About 20% of the energy is contained below the corner frequency, and 80% below *6.25** f_c. Typical upper limits on instrumental recording frequency are 20 – 100 Hz; the highest frequency used is the Nyquist, which is as low as 10 Hz. The lower frequency limit is set by the noise level of the empirical Green's functions, but is only limiting for the great earthquakes. In the case of Tohoku-Oki M_w *9.1*, the lower cutoff is ~0.01 Hz, meaning the corner frequency for that event is not resolvable. When calculating radiated energy, extrapolation into the high and low frequencies is necessary to capture all of the energy [e.g. *Ide and Beroza,* 2001].

In this thesis, I shed light on the controversy surrounding the scaling, or lack thereof, of radiated seismic energy. One method in particular using the seismic coda continually finds a non-self similar model [e.g. *Mayeda et al*, 1993], and so I develop a similar model in order to test those findings. I use empirical Green's functions to correct for path and site effects, to estimate true source spectra. By using relative measures, the estimates I make are very precise, although we may never be able to say what the true source is. I start by developing an eGf coda methodology to estimate source parameters for western US earthquakes of magnitude ~ 3 to M_w *7.1*, using the smallest earthquakes as eGf events, over local source-site distances, < 200 km. I find no evidence for a dependence of E_R/M_o on moment. I then extend the method to earthquakes of similar size in Honshu, Japan, finding self-similar behavior as well. In Chapter 5, I challenge the eGf assumptions on a teleseismic scale, using M_w *6.5 – 7.5* earthquakes as empirical Green's functions to correct great (M_w *>8.5*) earthquakes. I find that this method is valid, and that even the largest of earthquakes have apparent stresses very similar to the smallest of earthquakes. Chapter 4 takes a new look at the a_{RMS} stress drop of *Hanks* [1979] with recent data, in comparison with the eGf results from Honshu, Japan, where there are co-located velocity and acceleration instruments. I find that while the a_{RMS} stress drop is precise at close source-site distances (R < ~20 km), at farther distances attenuation

corrections become necessary. The further emphasizes the power of the eGf deconvolution to remove path effects.

The seismic coda refers to the waves that arrive after the direct arrivals. Because these waves are scattered and spread before being recorded at a station, they average the sampled earth structure and are more stable. In Chapter 2, I utilize the averaging properties of the coda to create more robust source spectra. I then use ~M 3 earthquakes as eGf events to iteratively correct the larger earthquakes for path and site effects. I study four earthquake sequences in the western US: Hector Mine 1999 M_w *7.1*; Parkfield 2004 M_w *6.0*; Wells, NV M_w *6.0*; and the Cerro Prieto swarm of 2008, whose largest events were M_w *5.1*. I estimate radiated energy and apparent stress for 225 earthquakes. Overall, I find no compelling evidence for an increase of apparent stress with moment, supporting self-similarity. For each sequence, I show the best fit line of E_R/M_o vs. M_o, which includes the zero-slope fit for three out of four sequences, and a very slight increase of E_R/M_o for the fourth. I find an average value of E_R/M_o of 3.5×10^{-5} fits the data well, which is very similar to global averages. I use up to 30 stations for each estimate, and show the inter-station scatter as non-parametric box plots. Because the study of radiated energy and how it relates to moment is currently controversial, it is important to quantify the observations of self-similarity.

In Chapter 3, I extend the method developed in the previous chapter to Honshu, Japan, studying again four sequences of earthquakes: Chuetsu 2004 M_w *6.7*; Iwate-Miyagi 2008 M_w *6.9*; Chuetsu-Oki 2004 M_w *6.6*; and the deep, Kamaishi repeating sequence, with largest magnitude M_w *4.7*. The denser instrumentation and higher sampling rate lead me to simplify some of the techniques, making the method more general. I measured radiated energy and apparent stress, as well as modeled corner frequency and stress drop for 89 earthquakes spanning a magnitude range of *1.8* to *6.9*. I find no systematic dependence of apparent stress or stress drop on seismic moment, and use the same statistical metrics as in Chapter 2 to back up the observations. I compare stress drop and apparent stress and find their ratio is constant and similar to the theoretical ratio. However, there are several anomalous events – both energetic and enervated – that show sharply different spectral signatures from the rest of the population.

These events indicate that much of the variation in apparent stress and stress drop is statistically significant, which may have important implications for seismic hazard analysis.

Chapter 4 revisits the a_{RMS} formulation of *Hanks* [1979], for the first time in at least 20 years, using recent, improved data. At the time, the a_{RMS} method was a huge improvement over current methods of estimating stress drop, because it was only dependent on the square-root of the corner frequency, a parameter that can be highly uncertain. I measure the a_{RMS} stress drops for the Chuetsu 2004 and Iwate-Miyagi 2008 sequences in Honshu, Japan, where there are co-located broadband velocity instruments, used in Chapter 3, and strong motion accelerometers. The a_{RMS} stress drop is much simpler to compute and can be used on an event-by-event basis, as there is no need to use eGf events, making it appealing for rapid source parameter estimation, as well as engineering ground motion prediction. At close source-site distances (R<~20 km), the a_{RMS} stress drop compares very well to the eGf Brune stress drop. However, because it does not make attenuation corrections, the stress drops are underestimated at farther stations. Furthermore, I relate the *PGA* to the a_{RMS} using random vibration theory, and show that given a very simple stress drop distribution as an input, *PGA* is very predictable, especially for large events or at close distances. This could be important for understanding the theoretical basis of ground motion prediction.

Last, but not least, Chapter 5 pushes the limits on empirical Green's functions to study great earthquakes. In Chapter 2 and 3, I use ~M 3 earthquakes as eGf events, which have source dimension *r~100 m*, recorded at local distances < 200 km, to estimate the source parameters for earthquakes as large as M_w *7.1*. For great earthquakes, however, we cannot study the entire process up close, but at teleseismic distances, >3000 km, magnitude 6.5 – 7.5 earthquakes look like point sources, with source dimension *r~10 km*. I analyze five recent great earthquakes: Tohoku-Oki 2011 M_w *9.1* in Japan*;* Sumatra, Indonesia 2004 M_w *9.2;* Maule, Chile 2010 M_w *8.8;* Nias, Indonesia 2005 M_w *8.7;* and Bengkulu, Indonesia 2007 M_w *8.5*. For each mainshock, I use 3 – 5 different large eGf events and deconvolve the spectra to remove path and site effects. The different eGf events, and different stations, give precise radiated energy estimates, validating this new

teleseismic method. The energies are very similar with those of other researchers, found for these great earthquakes. I show that both *P* and *S* waves can be used in teleseismic energy estimates, whereas previously only *P* waves were typically used. The azimuthal distribution of radiated energy shows trends consistent with the overall directivity of these great events, and simple modeling of Haskell line sources matches the observations well. Finally, the apparent stress of these five great events is in the range of 0.4 to 0.8 MPa, near the global mean of 1 MPa, showing no increase of apparent stress with earthquake size. Even these largest of earthquakes appear to behave under self-similar physics.

References

Abercrombie, R. E. (1995), Earthquake source scaling relationships from −1 to 5 ML using seismograms recorded at 2.5-km depth, *J. Geophys. Res.*, *100*(B12), 24015.

Aki, 1966 K. Aki, Generation and propagation of G-waves from the Niigata earthquake of June 16, 1964, 2. Estimation of earthquake moment, released energy, and stress-strain drop from G-wave spectrum. *Bull. Earthquake Res. Inst., Tokyo Univ.*, **44** (1966), pp. 73–88.

Allmann, B. P., and P. M. Shearer (2009), Global variations of stress drop for moderate to large earthquakes, *J. Geophys. Res.*, *114*(B1).

Brune, J. N. (1970). Tectonic stress and the spectra of seismic shear waves from earthquakes, *J. Geophys. Res., 75,* 4997-5009.

Boore, D. M. (1983). Stochastic simulation of high-frequency ground motions based on seismological models of the radiated spectra, *Bull. Seism. Soc. Am., 73*, 1865-1894.

Choy, G. L., and J. L. Boatwright (1995), Global patterns of radiated seismic energy and apparent stress*, J. Geophys. Res., 100*(B9), 18205–18228.

Convers, J. A., and A. V. Newman (2011), Global evaluation of large earthquake energy from 1997 through mid‐2010, *J. Geophys. Res*., 116, B08304, doi:10.1029/2010JB007928

Hanks, T. C. (1977), Earthquake stress drops, ambient tectonic stresses and stresses that drive plate motions, in *Pure and Applied Geophysics*, vol. 115, pp. 441-458-458, Birkhäuser Basel.

Hanks, T. C., (1979), b-values and ω-γ seismic source models: implications for tectonic stress variations along active crustal fault zones and the estimation of high-frequency strong ground motion, *J. Geophys. Res., 84*, 2235-2242.

Hanks, T. C. and H. Kanamori (1979), A moment magnitude scale, Jour. Geophys. Res, 84(B5) 2348 – 2350

Hartzell, S. H. (1978). Earthquake aftershocks as Green's functions*, Geophys. Res. Lett. **5**,* 104.

Hough, S. E. (1997), Empirical Green's function analysis: Taking the next step, *J. Geophys. Res., 102*(B3), 5369-5384.

Ide, S., and G. C. Beroza (2001), Does apparent stress vary with earthquake size?, *Geophys. Res. Lett., 28*(17), 3349.

Kanamori H., and D. L. Anderson (1975), Theoretical basis of some empirical relations in seismology, *Bull. Seism. Soc. Am., 65,* 1073-1096.

Kanamori, H, J. Mori, E. Hauksson, T. H. Heaton, L. K. Hutton and L. M. Jones (1993), Determination of earthquake energy release and ML using TERRAscope, *Bull. Seism. Soc. Am., 83*, 330-346.

Kostoglodov, V., S. K. Singh, J. A. Santiago, S. I. Franco, K. M. Larson, A. R. Lowry, and R. Bilham (2003), A large silent earthquake in the Guerrero seismic gap, Mexico, *Geophys. Res. Lett.*, 30(15), 1807, doi:10.1029/2003GL017219.

Mayeda, K., and W. R. Walter (1996), Moment, energy, stress drop, and source spectra of western United States earthquakes from regional coda envelopes, *J. Geophys. Res., 101*(B5), 11195 – 11208.

Mori, J., R. E. Abercrombie, and H. Kanamori (2003), Stress drops and radiated energies of aftershocks of the 1994 Northridge, California, earthquake, *J. Geophys. Res., 108*(B11), 2545, doi:10.1029/2001JB000474.

Orowan, E. (1960), *Mechanism of Seismic Faulting in Rock Deformation,* Geological Society of America Memoir 79, pp. 323-345, Geological Society of America, Boulder, CO

Prieto, G. A., P. M. Shearer, F. L. Vernon, and D. Kilb (2004), Earthquake source scaling and self-similarity estimation from stacking P and S spectra, *J. Geophys. Res., 109*, B08310, doi: 10.1029/2004JB003084.

Singh, S. K., and M. Ordaz (1994), Seismic energy release in Mexican subduction zone earthquakes, *Bull. Seism. Soc. Am., 84*, 1533– 1550.

Sonley, E., and R. E. Abercrombie (2006), Effects of Methods of Attenuation Correction on Source Parameter Determination, in *Earthquakes: Radiated Energy and the Physics of Faulting, Geophys. Monogr. Ser., vol. 170,*, edited by R. Abercrombie et. al., pp. 91 – 97, AGU, Washington, DC.

Thatcher, W., and T. C. Hanks (1973), Source parameters of southern 13alifornia earthquakes, J. Geophys. Res, 78, 35, 8547 – 8676

Venkataraman, A. and H. Kanamori (2004), Effect of directivity on estimates of radiated seismic energy, *J. Geophys. Res., 109*, B04301, doi:10.1029/2003JB002548.

Walter, W. R., K. M. Mayeda, R. Gok and A. Hofstetter (2006), The scaling of seismic energy with moment: simple models compared with observations, in *Earthquakes: radiated energy and the physics of faulting*, Geophysical Monograph Series, 170, 25-41, doi:10.1029/170GM05.

Yamada, T., J. J. Mori, S. Ide, R. E. Abercrombie, H. Kawakata, M. Nakatani, Y. Iio, and H. Ogasawara (2007), Stress drops and radiated seismic energies of microearthquakes in a South African gold mine, *J. Geophys. Res., 112*, B03305, doi:10.1029/2006JB004553.

.

CHAPTER 2

Radiated Seismic Energy from Coda Measurements Indicates no Scaling in Apparent Stress with Seismic Moment

Abstract

The seismic coda consists of scattered waves that leave the earthquake source in a variety of directions. This averaging of source radiation leads to stable ground motion spectra that we use as the basis for a robust measurement of radiated wave energy. We apply an empirical Green's function (eGf) method to the seismic coda in order to investigate scaling of the radiated seismic energy. We correct for path effects in the spectra of earthquakes using a stack of closely located, small earthquakes as an eGf. We apply this approach to four earthquake sequences in western North America that span a magnitude range from *Mw 3.0 – Mw 7.1*. Our estimates of scaled energy are consistent with independent measurements, where available. We find no dependence in individual seismic energy estimates on source-station distance, which validates the eGf approximation. We find that a constant scaled energy provides a reasonable fit to the data, with no dependence of the scaled energy on seismic moment.

2.1 Introduction

A long-standing discrepancy exists in studies of radiated seismic energy. Some studies find that the scaled energy – the ratio of seismic energy to seismic moment –

Baltay, A., G. Prieto, and G.Beroza (2010), Radiated seismic energy from coda measurements and no scaling in apparent stress with seismic moment, *J. Geophys. Res.* **115**(B8), doi: 10.1029/ 2009JB006736.

varies systematically with earthquake size [e.g., *Kanamori et al*, 1993, *Abercrombie*, 1995, *Mayeda and Walter*, 1996, *Mori et al*., 2003, *Walter et al*., 2006] while others find that it does not [e.g., *Choy and Boatwright*, 1995, *Ide and Beroza*, 2001, *Prieto et al*., 2004, *Yamada et al.,* 2007]. The scaling of seismic energy is an important issue for both the physics of earthquake faulting and for strong ground motion prediction. For earthquake physics, a break in scaling might be diagnostic of a characteristic length scale in the faulting process. For strong ground motion prediction, if large earthquakes radiate seismic energy more efficiently than do small earthquakes, then they have the potential to generate more intense strong ground motion.

The controversy in energy scaling arises because, even though radiated energy is a scalar quantity, it is difficult to measure accurately. Seismic waves are generated with strong angular variations at the source due to both the radiation pattern and source directivity. As these waves propagate they attenuate, scatter and focus/de-focus and are subject to strong frequency-dependent site effects in the near surface. All of these factors influence wave amplitude, and because they are difficult to correct for accurately, independent studies of the same earthquake may find seismic energies that differ by an order of magnitude [*Singh and Ordaz*, 1994].

Many sources of variability exist between different studies [*Ide et al.* 2003], and it is difficult to correct consistently for wave propagation effects over many orders of magnitude, and across different tectonic settings. Some studies have found no evidence that scaled energy increases with seismic moment. *Ide and Beroza* [2001] compiled previous studies, applied adjustments that would correct for probable bias in measurements of the radiated energy, and found that although scaled energy varies widely for a given earthquake size, it does not show a systematic trend with seismic moment. *Prieto et al.* [2004] used spectral stacking and came to a similar conclusion for small earthquakes. *Imanishi and Ellsworth* [2006] found constant scaled energy for even smaller earthquakes.

Other studies have come to the opposite conclusion, finding that scaled energy increases systematically with increasing seismic moment. *Mori et al.* [2003] found an

increase in scaled energy with moment for aftershocks of the 1994 Northridge earthquake. *Takahashi et al.* [2005] found an even stronger scaling, with scaled energy increasing as $Mo^{0.44}$ for earthquakes in Japan. Perhaps the strongest evidence for dependence of the scaled energy on seismic moment comes from energy estimates based on the scattered waves of the seismic coda.

Mayeda [1993], *Mayeda and Walter* [1996] and *Mayeda et al.* [2003] have developed a method to isolate the coda source spectra by empirically correcting for path and site effects. In this method, narrowband envelopes of the coda are created. Then, the decay shape of the coda envelope with time is modeled as $t^{-\gamma} exp(-bt)$, and the parameters b and γ are parameterized with distance. Empirical envelopes are created with the parameters, and are fit again to the data. Their coda spectral amplitude is determined as the linear term in the fit of the synthetic envelopes to the observed envelopes. *Mayeda and Walter* [1996] use an eGf correction technique to estimate the scaled energy, and conclude that it increases as $Mo^{0.25}$, a very strong trend. *Mayeda* [2005] find scaling with an exponential slope of 0.12 to 0.38 for four distinct geographical areas. In addition, *Mayeda et al* [2007] extend their empirically derived coda spectra to a spectral ratio method, and find that spectra are not self similar. Until these disparate conclusions are reconciled, the question of whether scaled seismic energy varies systematically with seismic moment must be considered unresolved.

In this study we measure seismic energy using the scattered waves of the seismic coda without empirically fitting the envelope decay shapes. A distinct advantage of coda waves is that because they are scattered, they average factors such as directivity and radiation pattern to give a more stable amplitude measurement [*Mayeda*, 1993, *Mayeda et al.,* 2007]. A major benefit of this method lies in the simplicity behind it. Without having to empirically make the envelope shape corrections we make many fewer assumptions in the analysis. We compare the coda for different earthquakes recorded at the same station using what amounts to an empirical Green's function technique to remove sources of common-mode error, primarily propagation effects, from the measurement. The result is a stable measure of relative wave amplitudes over a wide frequency range that can be used to estimate the radiated energy. We apply this technique to four earthquake

sequences in western North America that, taken together, span a magnitude range of $3 \leq M_w \leq 7.1$. Our results agree with other energy estimates for the larger earthquakes in our sample, and we find that scaled energy does not increase with seismic moment for this data set. Examination of a larger earthquake catalog will determine whether this result generalizes.

2.2 Empirical Green's Function Approach for Coda Spectral Amplitude

Waves generated by an earthquake attenuate, focus/de-focus and scatter as they propagate through the complex geology of the Earth. The seismograms that result are a mixture of source and propagation effects. The empirical Green's function approach assumes that the predominant differences for earthquakes located close to one another arise from source effects [*Mueller,* 1985]. We use this principle to isolate source effects, and in particular, to examine the relative energy radiation of closely spaced events.

We first assume that a small event has an ideal Brune spectral shape, obeying

$$u(f) = \frac{\Omega_o}{1 + (f / f_c)^2} \tag{1}$$

where $u(f)$ is the far-field displacement spectra, Ω_o is the long period amplitude level, proportional to seismic moment, and fc is the corner frequency [*Aki*, 1967, *Brune*, 1970]. The use of a similar ω^{-2} model [*Boatwright*, 1978] yields no effect on the scaled energy, but due to a sharper corner frequency the Boatwright model estimates energies of ~13% higher as compared to the Brune model. Next, we assume that this small event, typically $M_w \sim 3$, has a short duration, and hence a high corner frequency near 8 – 10 Hz, below which the eGf can be considered to approximate the point source response. The eGf can then be used to extract the spectral source characteristics of the larger events at frequencies below the eGf corner frequency. When using direct waves or individual events, stable results depend strongly on the choice of the Green's function event. Because we use the spectra of the seismic coda, and an average of many smaller events as our eGf, our estimate is less dependent on the choice of eGf than other methods.

We filter the displacement records with a 2 pass, 4 pole Butterworth filter in narrow bands between 0.01 Hz and just less than the Nyquist frequency of the instruments (10 Hz for Hector Mine and Parkfield and 20 Hz in the case of Cerro Prieto and Wells) (Figure 2.1a). 20 Hz is the limit of useful data recorded at surface stations in Southern California and the western US, known as f_{max} [*Hanks,* 1982]. Any aliasing that may occur due to data pre-processing affects each event by proportionally the same amount that cancels out when we compare relative spectral amplitudes of the events. We then take the envelope as the distance between the filtered record and its Hilbert transform,

$$E(t,f) = \sqrt{u(t)^2 + h(t)^2}\,. \tag{2}$$

Data and envelopes are visually checked to ensure that there are no clipped records, dropouts, spikes, or aftershocks in the coda. In some cases we use the accelerometer data in place of the broadband for the large events at close distances. The coda spectra are then created from a window in time over the length of the coda envelope (Figure 2.1a).

The coda window starts just after the S-wave arrival. We vary the window lengths with frequency in order to maximize the duration of the useful signal, but avoid a possible bias for large vs. small events by keeping window lengths constant across magnitude. The coda envelope reaches the noise threshold sooner for smaller events, such that the maximum length for the smallest event considered at each station sets the window length for all of the events. Because we use smaller events, our method is limited to shorter window lengths for the larger events than are often used in other coda studies [e.g., *Mayeda* 1996]. Shorter window lengths may increase the interstation variability and reduce the stability of the coda. We compensate for any loss in variance by including many stations in each analysis, up to 10 times as many as in previous coda studies. Coda envelope durations are measured empirically over magnitudes, frequencies and station-event distances, and the model is applied to all observed events within each sequence. The coda spectra value at each frequency is the time average of the narrow-band window for each frequency (Figure 2.1b). Once we measure the coda spectra, we stack events by magnitude. We stack events below magnitude 4.5 into bins that span approximately 0.25 magnitude units.

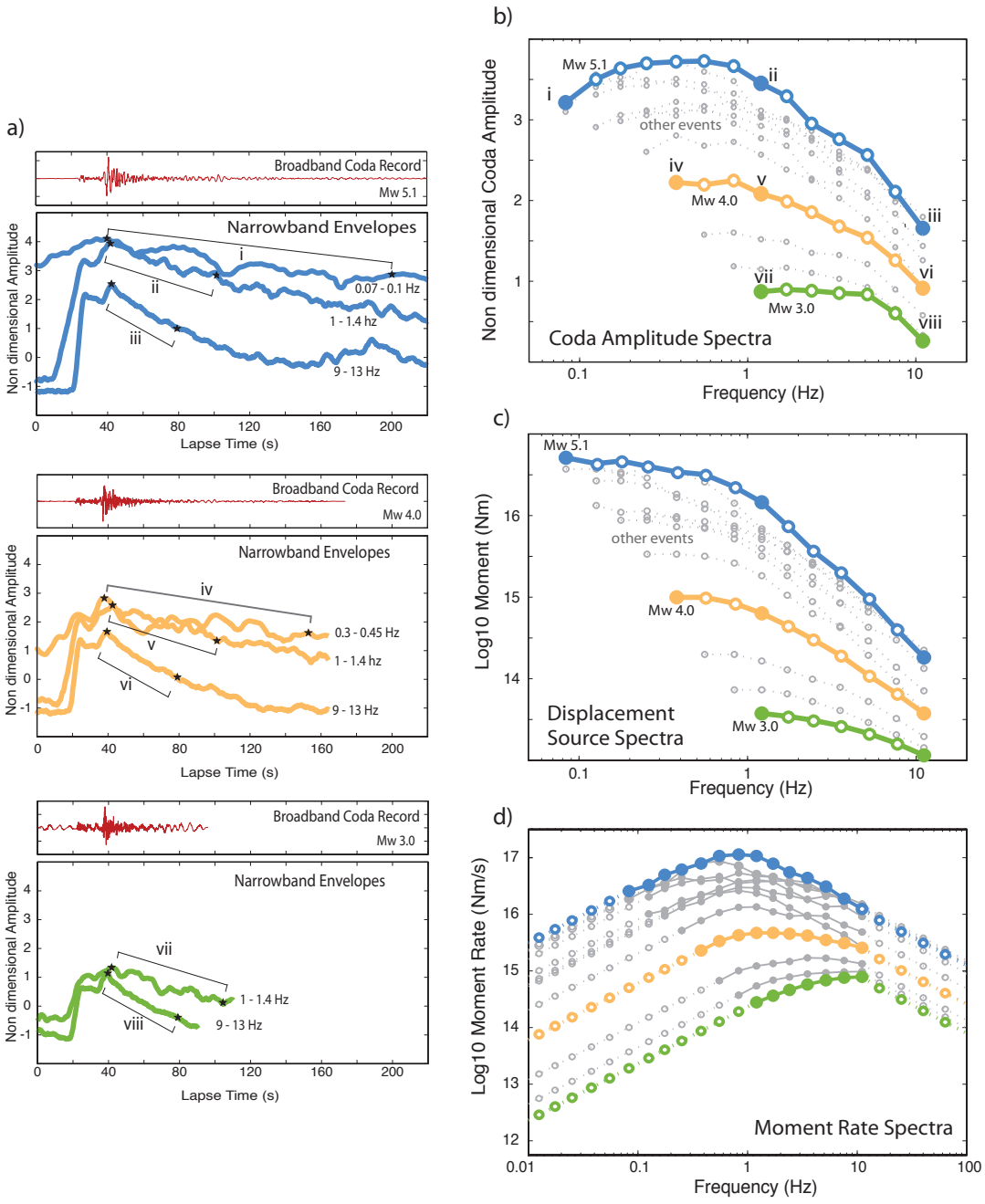

Figure 2.1 (a) Broadband coda seismogram and narrowband envelopes for three representative events at one station are shown for two/three schematic narrow pass-bands. Empirically derived starting and ending points of the envelope amplitude measurements are shown with stars. (b) Coda amplitude values at each frequency are found from the average of the narrowband envelope over the windows I – viii between stars. Representative frequency bands are indicated by numerals I – viii; other frequencies not shown in (a) indicated by open circles. Other events shown in grey; coda amplitudes found in the same manner as for the other events. (c) Displacement source spectra created by fitting the M_w 3.0 eGf event to an ideal Brune shape after calculating its corner frequency. Larger events are adjusted by flattening the left-most point of each next larger event, and propagating the correction upward. Finally spectra are adjusted up on a log scale to match the moments, while preserving spectral ratios. (d) Multiplication by ω yields velocity source spectra. Spectra are extrapolated to high and low frequencies. Energy is calculated from the integral of the

moment rate spectra. An ω^{-2} decay in displacement spectra, ω^{-1} in velocity, is assumed for all events for frequencies greater than our measurement window and this follows the asymptotic shape of the larger events nicely. However for the smallest events, the spectra has not yet reached that decay shape, so the ω^{-2} decay is conservatively underestimating the spectra, which may actually lead to underestimation of the energy in the smaller events.

Source spectra are isolated using a stack of several small events ($3 < M < 3.25$) as an empirical Green's function. The eGf is assumed to have a short duration and hence a high corner frequency. We estimate its corner frequency assuming a stress drop of $\Delta\sigma$=3 MPa and the relationship

$$f_o = \left(\frac{\Delta\sigma}{8.5 M_o} \right)^{1/3} \beta \tag{3}$$

after *Hanks and Thatcher* [1972]. We tested various choices of stress drops, ranging from 0.10 MPa to 10 MPa and found that the scaled energy is dependent on this initial choice of stress drop. A very small stress drop implies a very low corner frequency, causing the smaller events to have proportionally less energy. As the assumed stress drop increases, the scaling exponent decreases (Table 1). We use a stress drop of 3 MPa in this analysis, as that is the most common and yields a corner frequency most appropriate for the $\sim M_w$ *3* events. The eGf in each case has a corner frequency between 6.5 and 9 Hz and asymptotically approaches a flat spectra at low frequencies and a decay of ω^{-2} at high frequencies, so it is not exactly flat in our instrument bandwidth, especially near the corner frequency.

The eGf is fit to an ideal Brune spectral model over the frequency band we work in, and all the larger events are adjusted accordingly, to correct for propagation effects. Spectra of larger events are adjusted so that the observed spectral ratio between the eGf and larger events is maintained at all frequencies. Due to the limited signal-to-noise ratio of the smaller events, we can't do this over the entire range of frequencies. Each time we use a larger event, we flatten the lowest spectral measurement to match the second lowest measurement, and adjust all larger events proportionally. This proceeds in a stepwise manner to events of increasing seismic moment until all measurements have been adjusted. Finally, the spectra are shifted such that the long period end of the spectra fit their seismic moment, by assuming a moment only for the largest event, and allowing all

Table 2.1 Function of Assumed Stress Drop on the Scaling Exponent. The stress drop is assumed in each case, and the corner frequency and duration are calculated for the smallest EGF event according to equation (3) and the relationship of duration as the inverse of the corner frequency. The scaling exponent is found from the best fit line to the scaled energy from the stacked spectra across all stations. A 95% confidence interval is from the fit, and the standard deviation describes the residuals. The scaling parameter " [after *Kanamori and Rivera*, 2004] describes the deviation from no scaling, so that a value of " = 0 represents self-similarity. In contrast, *Mayeda et al.* [2003] have found a scaling exponent of 0.25 and " = 1. The scaling exponent is equal to "/("+3). The shaded areas indicate stress drops, corner frequencies, and durations that are unreasonable for the small earthquake.

Hector Mine

Assumed for smallest event			Derived			
*Stress Drop (MPa)	*Corner Frequency (Hz)	*Duration (s)	Scaling Exponent	95% Conf. Interval	STD	ε
1	4.80	0.21	0.265	0.07	0.29	1.080
3	6.93	0.14	0.091	0.08	0.22	0.300
5	8.21	0.13	0.075	0.08	0.23	0.242
10	10.35	0.10	0.058	0.09	0.23	0.185

*magnitude 3.1 event

Parkfield

Assumed for smallest event			Derived			
*Stress Drop (MPa)	*Corner Frequency (Hz)	*Duration (s)	Scaling Exponent	95% Conf. Interval	STD	ε
1	4.50	0.22	0.073	0.09	0.16	0.236
3	6.48	0.15	0.001	0.09	0.16	0.004
5	7.68	0.13	−0.025	0.09	0.16	−0.073
10	9.68	0.10	−0.053	0.09	0.16	−0.150

*magnitude 3.2 event

Cerro Prieto

Assumed for smallest event			Derived			
*Stress Drop (MPa)	*Corner Frequency (Hz)	*Duration (s)	Scaling Exponent	95% Conf. Interval	STD	ε
1	4.95	0.20	0.088	0.08	0.14	0.287
3	7.13	0.14	0.016	0.09	0.15	0.049
5	8.46	0.12	−0.010	0.09	0.16	−0.029
10	10.66	0.09	−0.037	0.10	0.17	−0.108

*magnitude 3.1 event

Wells, NV

Assumed for smallest event			Derived			
*Stress Drop (MPa)	*Corner Frequency (Hz)	*Duration (s)	Scaling Exponent	95% Conf. Interval	STD	ε
1	6.30	0.16	0.080	0.10	0.18	0.259
3	9.08	0.10	0.022	0.10	0.19	0.068
5	10.77	0.09	−0.001	0.10	0.19	−0.003
10	13.57	0.07	−0.027	0.10	0.20	−0.080

*magnitude 2.9 event

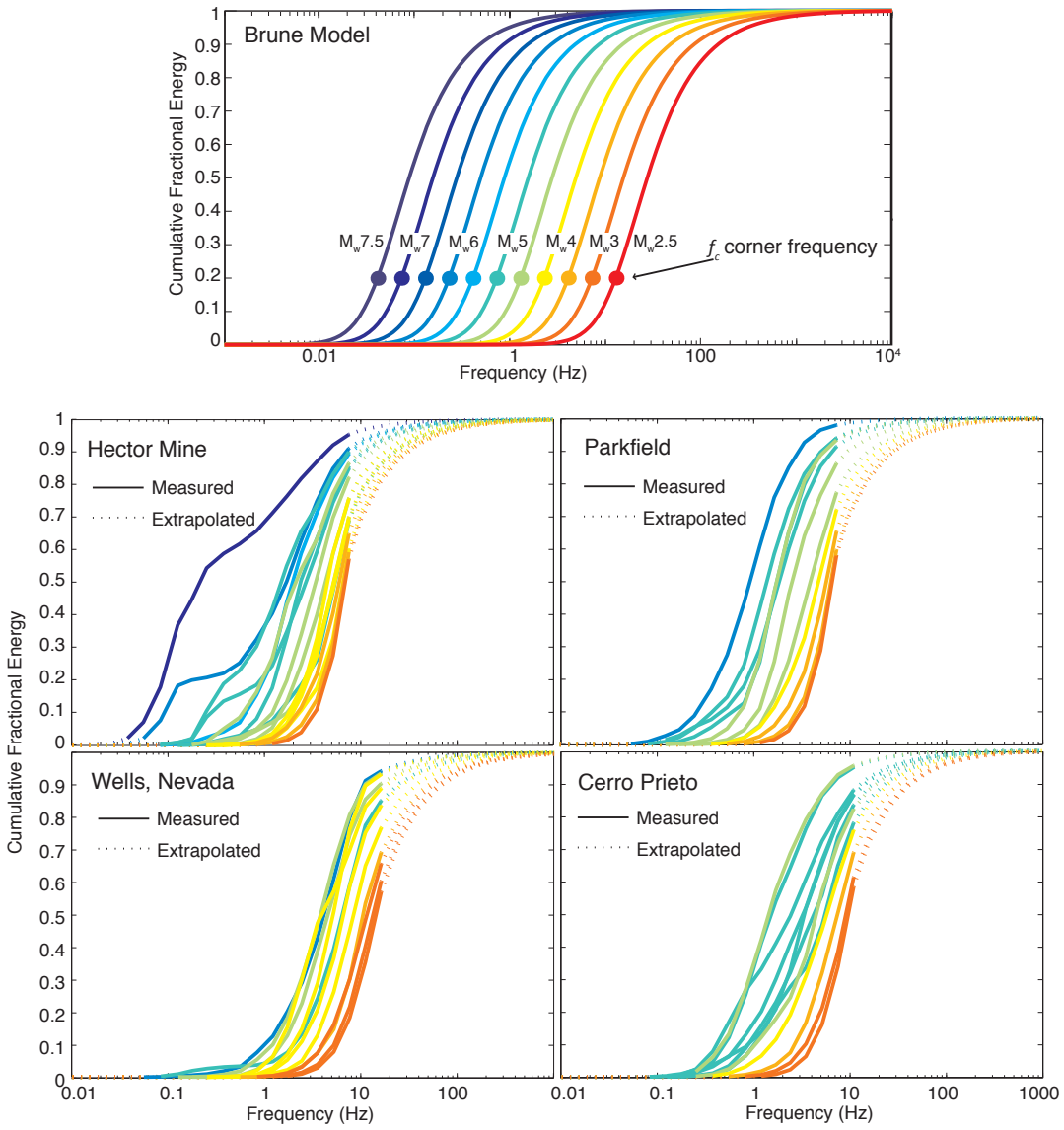

Figure 2.2 Cumulative fractional energy with frequency. (a) Ideal Brune ω^{-2} models for a range of magnitudes. Energy measured up to the corner frequency represents only 20% of the total energy. (b) Cumulative energy for all of the events in the four study areas. Colors of the data cumulative energy indicate the magnitude as shown in the Brune model in (a). Solid lines indicate the measurement range, while dashed lines indicate the extrapolated portion of the energy estimate, analogous to the dotted lines in Figure 2.1-d. For some of the smallest events, only 55% of the energy is contained in the instrument bandwidth, implying that extrapolation into higher frequencies is required to completely measure the radiated energy.

the smaller events to follow (Figure 2.1 b – c). Once displacement source spectra are determined for all events and stations, the spectra of all events at each station are adjusted in what amounts to a station correction for amplitude, to best fit the stacked spectra

across all stations. In this process, the relative spectral amplitudes for all earthquakes as recorded at each station are always preserved.

Radiated energy is calculated from the integral of the velocity spectrum, $\omega \cdot M(\omega)$, where ω is the angular frequency and $M(\omega)$ is the moment-rate spectrum. To estimate the energy, spectra should be integrated over all possible frequencies; however, the 40 samples per second sampling rate for many of the stations limits our analysis to a Nyquist frequency of 20Hz. For some of the earthquakes, a significant fraction of the total radiated energy will be contained in frequencies higher than this. Thus, the moment-rate spectra are extrapolated to both the upper, and lower, frequency limits. Following the ω^{-2} decay of the displacement spectra, we model the velocity spectra to decay as ω^{-1} above the corner, and ω^{1} below (Figure 2.1d). Finally, energy is estimated from area under the square of the velocity spectra, using the constants ρ, material density, as 2700 kg/m^3 and β as the *S*-wave velocity, 3.5 km/s [e.g., *Mayeda and Walter* 1996]

$$E_R = \frac{1}{4\pi^2 \rho \beta^5} \int_0^\infty \left| \omega \cdot M(\omega) \right|^2 d\omega \qquad (4).$$

We examine the effect of limited bandwidth on energy estimation in our data, as over 80% of the seismic energy may be radiated at frequencies greater than the corner frequency [*Ide and Beroza*, 2001]. The cumulative fractional energy indicates the proportion of energy measured as a function of frequency (Figure 2.2). In the Brune model, it can be seen that about 20% of the energy is measured below the corner frequency, which is near the instrument bandwidth for very small events. Our data indicates as little as 55% of the energy is in the instrumentally measured bandwidth for our smallest events, near $M_w \sim 3$. Even for intermediate sized events, a substantial fraction of the radiated energy is not measurable directly. This is an unavoidable consequence of the broadband character of the radiated energy, due to the high-frequency limitation of recorded data. Some extrapolation to higher frequencies is required. The shapes of the cumulative energy function for the events we analyze are similar to the ideal model. The Hector Mine mainshock, however, was a complex rupture with a duration of over 10

seconds, occurring on a branching fault system, and thus we are not surprised that it does not follow the ideal Brune shape.

2.3 Four Study Areas

The method requires earthquakes close enough together that they share common path effects [e.g., *Hough,* 1997]. We analyze four earthquake sequences from western North America: the M_w *7.1* 1999 Hector Mine sequence; the M_w *6.0* 2004 Parkfield earthquake sequence; the 2008 swarm near the Cerro Prieto geothermal field in Mexico with several events of M_w *5*; and the M_w *6.0* 2008 Wells, Nevada sequence (Figure 2.3). In each case, the moment magnitudes are determined from the global CMT catalog, for larger events, and NEIC catalogs for the smaller event. These four data sets include events with both a range of magnitude over which moment-dependent energy scaling has been observed previously, and a diversity of mechanisms. For each sequence, at least 40 events occur in close proximity to one another, and are well recorded on broadband seismic networks. The Hector Mine mainshock and aftershocks are the most spatially distributed due to the long and complex rupture, but about 80% of the events are within 25 km of each other, and with the exception of the closest station (HEC), the nearest stations are 80 km away. At Parkfield, the events are again distributed along the fault trace, with 80% within 10 km of each other, and with the exception of one close station at Parkfield (PKD) the stations are at least 50 km away. The Wells events are the most tightly clustered, with 90% within 10 km of each other, and in Cerro Prieto, 85% are within 20km from each other. We analyze $M_w > 4$ earthquakes

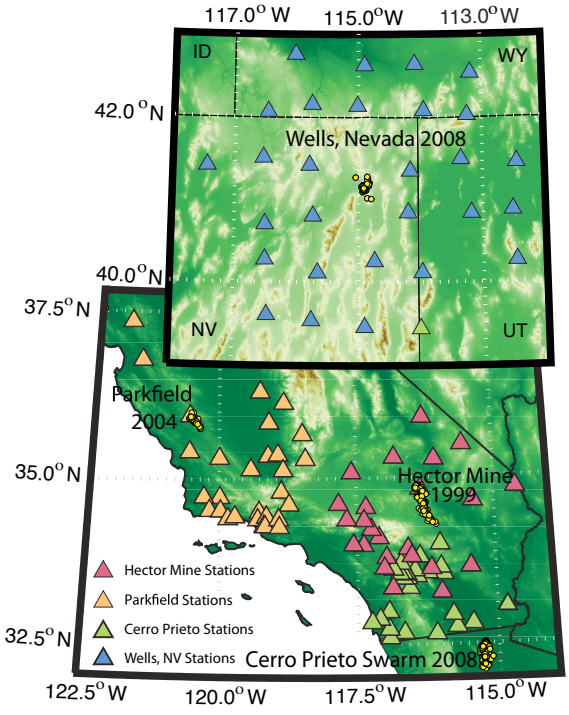

Figure 2.3 Study areas and stations used in analysis.

individually, and groups of smaller events in a stacked aggregate, the smallest of which is used as the eGf [*Prieto et al.,* 2004]. We believe that these distances are adequate to use in the eGf method given that we stack many smaller events to create the eGf, and because we use the more stable coda in the spectra. At close stations for the large events, instrument-response-corrected low-gain recordings are used; while for smaller events and at larger distances, instrument-response-corrected broadband high-gain recordings are used. We repeat the analysis at approximately 30 stations for each earthquake sequence, at distances ranging from several kilometers to 250 km. The large number of stations reduces the variability in the averaged measurements.

2.4 Scaled Energy vs. Moment

In total, we analyzed 225 events spanning a magnitude range from M_w *2.8* to M_w *7.1*. Once we stack over the smaller magnitude bins, we have estimates of radiated energy for 53 events. The tectonic settings vary from right-lateral strike-slip on the San Andreas to normal faulting in the basin and range province [NEIC moment tensor solutions, http://neic.usgs.gov/]. We find that the apparent stress, defined as

$$\tau_a = \mu \frac{E_R}{M_o} \tag{5}$$

with shear modulus μ (*Wyss*, 1970), for the four earthquake sequences we studied varies between about 0.1 MPa and 1 MPa, but shows no dependence on seismic moment (Figures 2.6 and 2.7).

The range of interstation measurements can be seen on Figure 2.4 as dots, and are represented statistically in Figure 2.5 with box plots. Box-and-whisker plots compactly and non-parametrically display the dispersion in data. The middle bar is the median; the top and bottom of the box indicate the 25th and 75th percentiles, the difference of which is the interquartile range; whiskers show the distance to the farthest data point within the interquartile range; and pluses are outlying data points, defined as farther than 1.5 times the interquartile range. The individual measurements are closely clustered with few outliers,

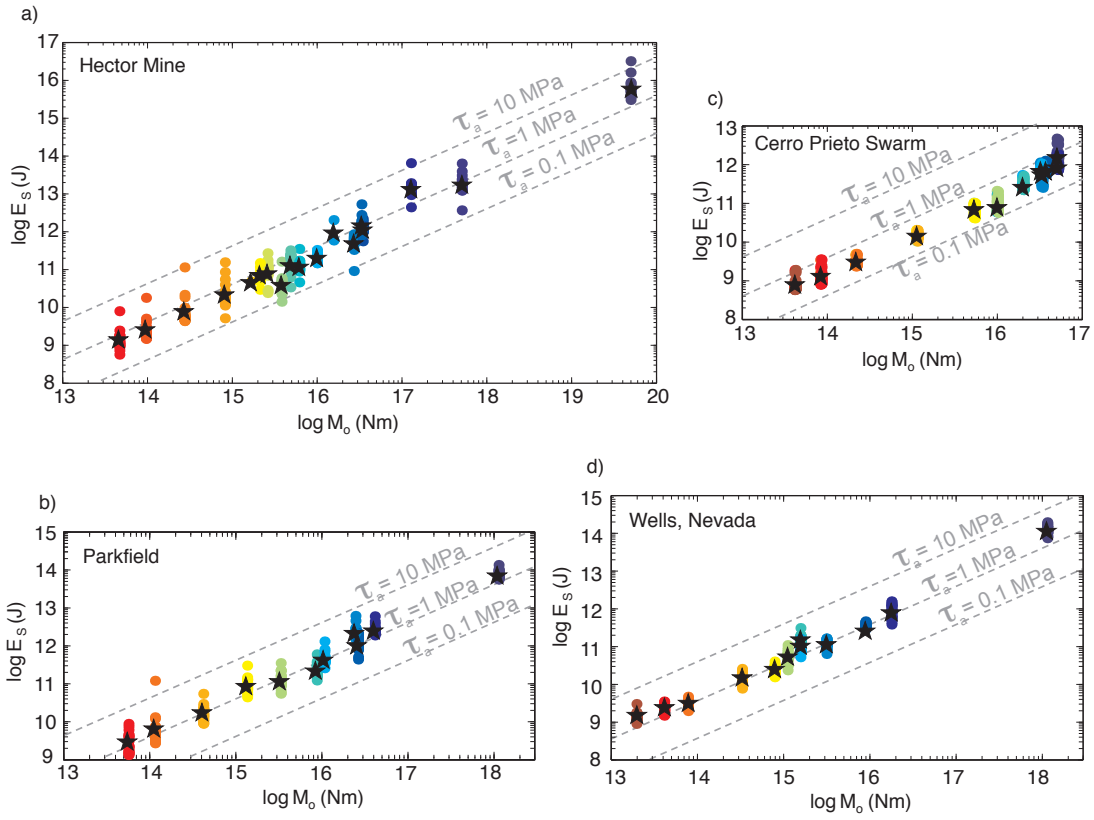

Figure 2.4 Radiated energy versus moment for the four study areas. Circles show the energy estimates at individual stations for each event. Black stars indicate the mean of the station estimates. Energy estimated from the spectra stacked across stations is not shown explicitly here as it is within the symbol size of the mean energy shown in stars. Dashed lines show constant apparent stress.

outliers, and interquartile ranges are small. Best-fit lines to the stacked spectra are shown in Figure 2.5 as well as the 95% confidence interval on the fits.

The Hector Mine mainshock and its aftershocks have apparent stress around 1.0 MPa. We find that the energy of the M_w *7.1* Hector Mine mainshock is 6.1×10^{15} J, which is within a factor of three of independent studies that find the energy to be 3×10^{15} J (*Venkataraman et al.*, 2002) and 3.4×10^{15} J (*Boatwright et al.,* 2002), as well as the published NEIC radiated energy of 1.9×10^{15} J (http://neic.usgs.gov/). These three estimates fall within the inter-station scatter for this earthquake. The average E_R/M_o ratio is 4.1×10^{-5} for this sequence, which translates to an apparent stress of 1.1 MPa. Our least squares fit to the data is $E_R/M_o \sim M_o^{\,0.091+/-0.08}$, which includes the zero-slope exponent. We analyze 77 events in the Hector Mine mainshock – aftershock, the smaller of which stack into four magnitude bins between M_w *3.0* and *Mw 4.0*, for 18 total energy

measurements. The mainshock has a near vertical, right-lateral strike-slip mechanism, consistent with the sense of motion in southern California.

The Parkfield events have a slightly higher apparent stress. The inter-station scatter for this sequence is low. The average scaled energy is 5.6 x 10^{-5}, or an apparent stress 1.8 MPa. The relationship found for the Parkfield subset is $E_R/M_o \sim M_o^{0.001+/-0.09}$, which again is consistent with zero slope. We find the energy of the M_w *6.0* mainshock to be 8.1 x 10^{13} J. This is higher than what was found by *Ma et al*. [2008], who estimated the energy of the mainshock as 1 x 10^{13} J, but their estimate is based on a dynamic rupture model of the mainshock, which only provides a lower bound on the radiated energy. Similar to the Hector Mine sequence, the Parkfield mainshock was nearly pure right-lateral strike-slip

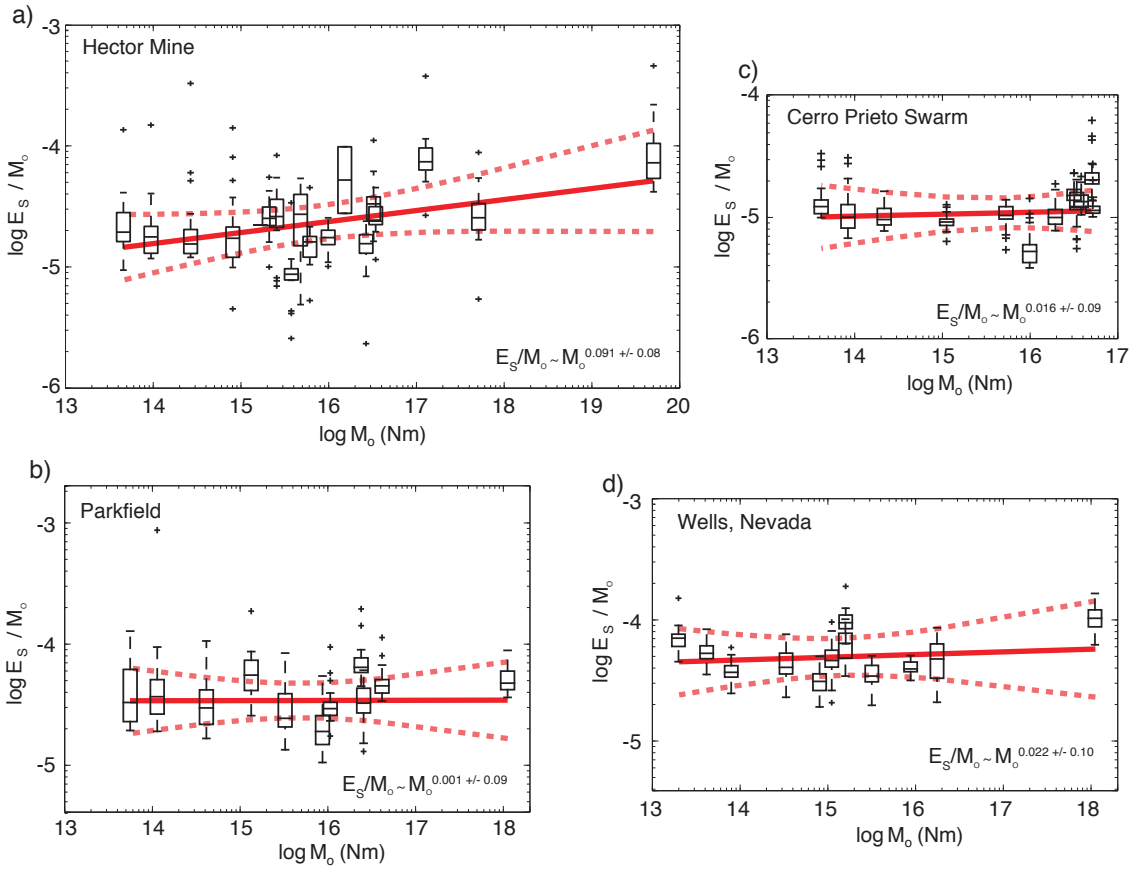

Figure 2.5 Scaled energy vs. moment for the four study areas. Data range is given by the box and whisker plot, where the middle bar is the median and the box indicates the 25th and 75th percentiles, the difference of which is the interquartile range. The whiskers show the distance to the farthest data point within the interquartile range and the pluses are outlying data points, defined as more than 1.5 times the interquartile range. For most events the whiskers are small and few, if any, outliers exist, showing that the interstation scatter is tight. The heavy black line shows the best fit to the stacked spectra (also shown in Table 1) and the dashed grey lines are the 95% confidence intervals on the fit.

along the San Andreas fault. The aftershocks number 47, and after the binning of the 39 smallest events, between M_w *2.8* and M_w *4.0*, there are 11 final energy estimates.

The Wells, Nevada 2008 sequence has the lowest inter-station variability, possibly due to the even azimuthal station spacing and similarity of the US Array instruments. For the M_w *6.0* mainshock we find an energy of 1.2 x 10^{14} J, about an order of magnitude higher than the NEIC estimate of 8.9 x 10^{12} J. All of the events in this sequence have a stress drop near 1 MPa, and the average E_R/M_o ratio is 5.7 x 10^{-5}, which corresponds to an apparent stress of 1.8 MPa. The least squares fit to the data is $E_R/M_o \sim M_o^{\,0.022+/-0.10}$. The Wells, Nevada, M_w *6.0* mainshock occurred in a normal faulting regime, consistent with the active tectonics of the Basin and Range. We included 56 events within the aftershock sequence, which we binned to yield 12 radiated energy estimates.

The earthquakes in the Cerro Prieto sequence also have low inter-station scatter. Here again the apparent stress for all of the events falls between 0.1 MPa and 1 MPa and the average scaled energy is 1.7 x 10^{-5}, which corresponds to an apparent stress 0.55 MPa, the lowest of all of the sequences. This lower apparent stress may be explained by a difference in the actual shear wave velocity, β, or possibly material density, ρ, in the Cerro Prieto area. We hold β constant between study areas, yet the Cerro Prieto area is comprised of softer sediments, and is geothermically active, which may warrant a smaller β value. There is no obvious trend of increasing apparent stress with increasing moment. We found the relationship $E_R/M_o \sim M_o^{\,0.016+/-0.09}$ for the best fit to the Cerro Prieto data. 43 total events in the sequence are analyzed, from M_w *2.8* to M_w *5.1*, with several events in the M_w *5* range. The 35 smallest events are binned into four small magnitude bins, resulting in 12 total estimates. The Cerro Prieto earthquakes have oblique normal/right-lateral strike-slip motion, and occur near the Cerro Prieto geothermal field on the west side of a step over on the southern end of the San Andreas fault system, an area of both extension and right lateral movement.

Taken all together, our results are consistent with each other (Figure 2.8a) and with scaled energy from events that have been analyzed previously by other methods (Figure 2.8b), which supports the reliability of our empirical Green's function method. Our energy

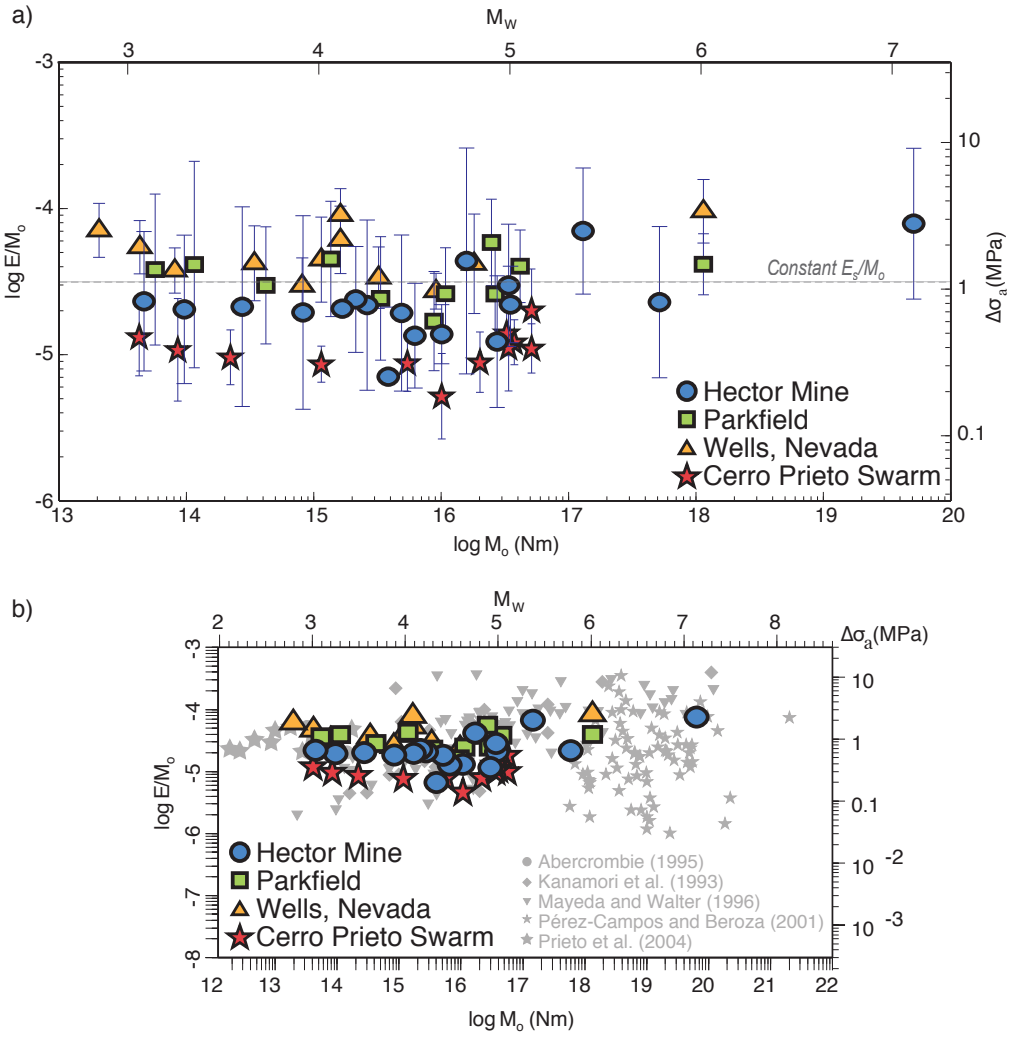

Figure 2.6 Scaled energy for all four data sets. A) Large symbols show mean value of scaled energy for each location and event. Grey error bars show 5% and 95% intervals on the inter-station scatter. B) Large dark symbols indicate the average scaled energy for each data set overlain on Ide and Beroza [2001]. Estimates from this study agree well with the previous results.

estimates indicate constant E_R/M_o, with an average scaled energy for all events of ~3.5 x 10^{-5}, which corresponds to an apparent stress of 1.2 MPa. We do not have enough events to fit to a non-linear or step-wise shape. The best fit to our observations, for each sequence and for all the sequences in aggregate, include the case of no scaling of scaled energy with seismic moment, that is $E_R/M_o \sim M_o{}^0$. We find an ε, as defined by *Kanamori and Rivera* [2004] close to 0, indicating self-similarity.

2.5 Validation of eGf Assumptions

We assume that for each seismic station, propagation effects are common to each earthquake in a sequence, such that spectral ratios are controlled by source effects. Using this assumption we estimate the energy for each event at each station from the coda source spectra, then stack the spectra across all of the stations. The result is a stable solution, but we can use several aspects of the result and the residuals to confirm that the assumptions that went into our analysis are reasonable.

To test the path assumptions, we examine the energy measurements from stations at varying distances from the events (Figure 2.9). We find no systematic behavior in the trends of the scaled energy estimates with distance, which indicates the eGf assumption properly accounts for wave propagation effects in the coda at all the distances considered. We also find that the inter-station scatter is similar at all distances. Both of these observations support our assumption that the coda spectral ratio measurements reflect source effects.

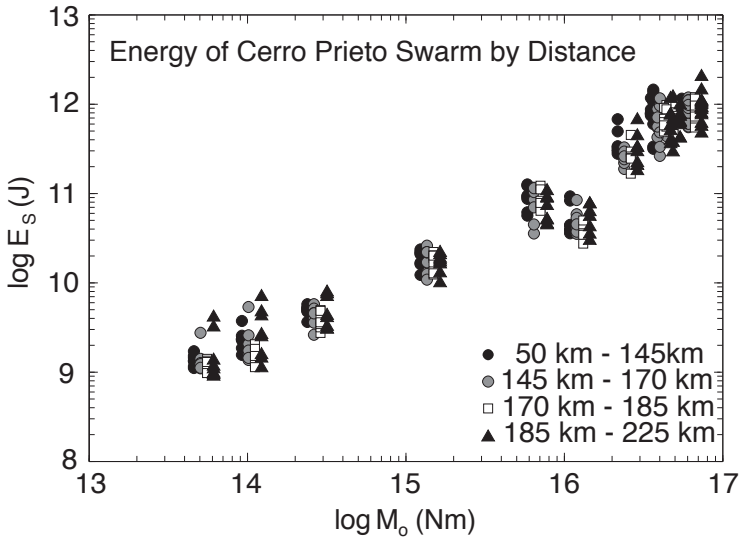

Figure 2.7 Energy from the Cerro Prieto data compared to station-to-event distance. Different symbols (black circle, grey circle, white square and black triangle) show energy estimates for increasing station-event distances. The different symbols for each are separated along the moment scale for visual clarity. The estimates show similar scatter and no distance dependence in the method.

Another measure of the reliability of our results is the scatter in the estimates at different stations. The scatter in individual station measurements is consistent within an order of magnitude or less for these events. Once we average over stations, the uncertainty is greatly reduced. Furthermore, the station-averaged spectra follow the widely observed ω^{-2} decay at frequencies higher than the corner (Figure 2.10).

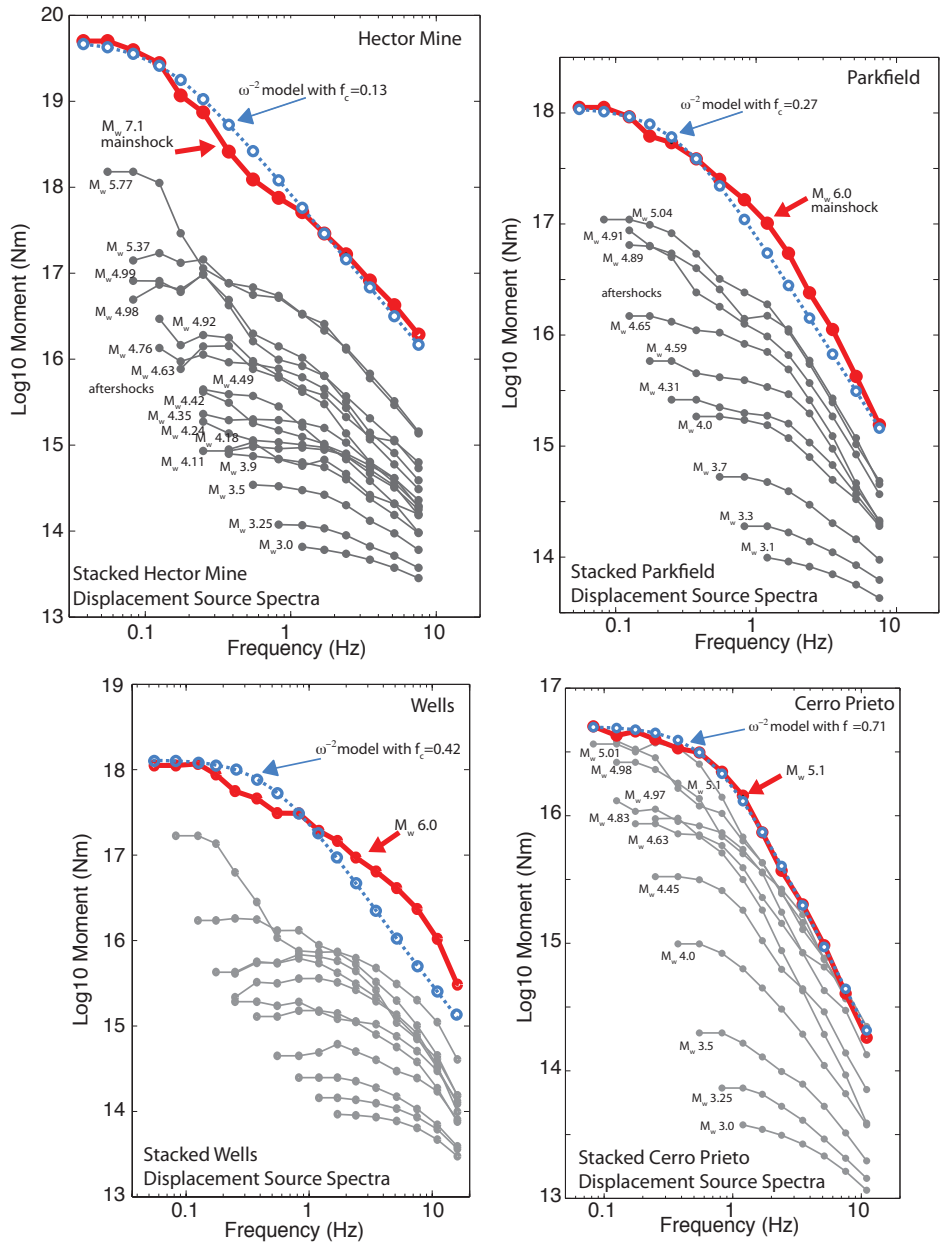

Figure 2.8 Stacked displacement (moment) source spectra for each sequence. The mainshock is shown in red, and aftershocks shown in light grey. All events are stacked over recordings at all stations used in the study. An idealized Brune ω^{-2} spectrum is shown with blue dashed line. In some cases, especially for the smaller events, the corrected mainshock is very Brune-like. The Wells event, however, does not show typical Brune spectral behavior.

In all cases, we have made several key assumptions. The first is to model the eGf event with a Brune spectrum with an ω^{-2} high frequency spectral decay and a smooth variation in amplitude near the corner frequency, following equation (1). To find this shape, we use a stress drop of 3 MPa and the Mw from the average magnitude of the

stacked smaller events, in equation (3). The amount of scaling found in this analysis is dependent on the initial assumption of stress drop, illustrated in Table 1. If the assumed stress drop used to model the eGf is low, less than 1 MPa, then the scaled energy depends on seismic moment. Likewise, if we assume a very high stress drop, greater than 10 MPa, then we find negative scaling. The choice of 3 MPa is consistent with stress drops found in numerous other studies. Although we assume a shape for the smallest event, the Brune-like behavior for the larger events (Figure 2.8) is derived from the data, not assumed.

Our second assumption is made while correcting for the path effects after the eGf is modeled. Because the spectra of the eGf is band limited, we propagate the corrections for each larger spectra upwards. However, we only correct one frequency point for each successively large event. In each sequence, the smaller events are stacked into four event bins, the smallest of which is modeled to the eGf. The remaining three bins each incur one corrected frequency point in removing the path effects. Another 16 unstacked, larger events over the four sequences each have one corrected frequency point, out of 37 total events. The other large events are corrected by the same amount. Finally, we tie all of the spectra to an absolute moment, using the magnitude of the largest event, which is well determined from several independent studies in each case. All other events are shifted by the same moment.

2.6 Conclusion

We use an empirical Green's function method assumption on the seismic coda to estimate seismic energy. We take advantage of the averaging properties of the coda by creating spectra over a coda envelope time window, which is more stable than a single direct measurement. The eGf method makes few assumptions, and is validated by consistency with independent energy measurements, and by the lack of systematic behavior in the residuals. In the four earthquake sequences we studied, we find that scaled energy does not vary systematically with earthquake size over the range $3 \leq M_w \leq 7.1$. Although we neglect particular site effects such as directivity or small differences in focal mechanism, we average our energy estimates over many stations in each study area covering a wide range of azimuths.

Our results support an earthquake model of self-similarity, also implying that other parameters, such as frictional energy per area or rupture velocity, do not vary strongly with earthquake size. The parametric scaling relations used to predict the level of high-frequency strong ground motion for potentially damaging earthquakes are largely based on measurements from earthquakes of more modest size. In such estimates, self-similarity is assumed. If this were not the case, the strong ground motion for hypothetical larger events might currently be underestimated. Because constant scaled energy is consistent with constant stress drop, our results support the current practice of using constant stress drop for strong ground motion modeling in that we do not find higher scaled energy in larger events.

The strong dependence of E_R on size suggested by *Mayeda et al*. [1996] and *Mayeda et al.* [2005] is not supported by our energy estimates. For each of the four study areas, our best-fit trend indicates a constant scaled energy, or an exponent of zero. Using our coda methodology outlined above, our results disagree with the results presented by Kevin Mayeda and colleagues [*Mayeda* 1996, *Mayeda et al*, 2000, 2003, 2005, 2007, *Morasca et al*. 2005, *Malagnini et al*. 2008]. They have consistently obtained a non-self similar scaling between apparent stress and seismic moment, while we haven't. There are two important differences between their analysis and the one presented in this paper, namely coda shape parameters and number of stations.

First, *Mayeda et al.* [2003] estimate coda shape parameters and distance corrections using available stations in order to fit a synthetic coda envelope to the measured coda envelopes, as an intermediate step in their analysis. From the best-fit envelopes they estimate the amplitude spectra. We also use coda envelopes, which decay over time; however, our coda spectral amplitude is a simple time-averaged value of the envelope. Because we use co-located events, we avoid the need to model the coda envelope decay parameters. By avoiding this middle step, and the adjustable parameters that it entails, our method makes fewer assumptions, rendering it more robust. Any disadvantage in our method due to shorter window lengths is more than compensated by the inclusion of up to 10 times as many stations in our analysis. As discussed above, we test the reliability of

our methodology by looking at effects of distance between source and receivers and the eGf assumptions made, and the results support our assumptions.

Second, in the results Mayeda and colleagues have presented so far, only a few stations have been used (2 – 7 stations) compared to at least 23 stations used in our study. While using more stations provides a way for obtaining reliable uncertainty measurements, it does not explain the discrepancy in scaling. The possibility that coda shape parameters using a few stations could bias the results could be tested be using the method of Mayeda with more stations or comparing predicted envelopes with observed ones with stations not used in the fitting step. These tests, although very relevant to the resolving of the scaling of earthquakes, are beyond the scope of our paper.

A second methodology employed by *Mayeda et al.* [2007] creates spectral ratios of the coda amplitude spectra to model the dependence of corner frequency on moment. Spectra are created as in *Mayeda et al.* [2003], but rather than making an eGf correction for the path, the spectral ratio is analyzed directly to determine the corner frequency and other source parameters. To determine the apparent stress, a reference event is used as benchmark and scaled using the found scaling parameter. The trade off in fitting between moment, corner frequency and the high frequency decay rate may be highly sensitive, and the choice of reference apparent stress will affect the final apparent stress. We do not employ this method here, as it doesn't directly estimate radiated energy, and the corner frequency and spectral fall-off fitting is highly dependent on each other and difficult using small events with limited spectral bandwidth.

While our results show that scaled energy is constant, this study is limited. Due to the eGf methodology, only events occurring in close proximity can be compared. The magnitude range is small, from $3 \leq M_w \leq 7.1$. M_w *3* is a lower limit due to noise, and M_w *7.1* is near the upper limit on the size of earthquakes recorded in the Western United States. Other studies using different methods have found constant scaled energy in smaller events, but it may not be prudent to compare studies. Thus, it is necessary to understand if this constant scaled energy is consistent in a single study over larger study

areas with a wider range of magnitudes to truly understand earthquake source physics and strong ground motion.

Acknowledgements

We thank Tom Hanks and Kevin Mayeda for helpful discussion. Comments from Rachel Abercrombie and Kevin Mayeda improved the manuscript. This research was supported by the Southern California Earthquake Center through the Extreme Ground Motion project group. SCEC is funded by NSF Cooperative Agreement EAR-0106924 and USGS Cooperative Agreement 02HQAG0008. The SCEC contribution number for this paper is 1287. Annemarie Baltay is supported by a Gabilan Stanford Graduate Fellowship. Data used in this analysis is from the CalTech, Anza, Berkeley and TA networks, accessed through the IRIS Data Management Center and the SCEC Data Center.

References

Abercrombie, R. E. (1995), Earthquake source scaling relationships from −1 to 5 ML using seismograms recorded at 2.5-km depth, *J. Geophys. Res.*, *100*(B12), 24015.

Aki, K. (1967), Scaling law of seismic spectrum*, J. Geophys. Res., 72*, 1217–1231.

Boatwright, J. (1978), Detailed spectral analysis of two small New York State earthquakes, *Bull. Seism. Soc. Am., 68*, 1177-1131.

Boatwright, J., G. L. Choy and L. C. Seekins (2002), Regional estimates of radiated seismic energy, *Bull. Seism. Soc. Am., 92*, 1241-1255.

Brune, J. N. (1970). Tectonic stress and the spectra of seismic shear waves from earthquakes, *J. Geophys. Res., 75,* 4997-5009.

Choy, G. L., and J. L. Boatwright (1995), Global patterns of radiated seismic energy and apparent stress*, J. Geophys. Res., 100*(B9), 18205–18228.

Hanks, T. C. (1982), fmax, *Bull. Seism. Soc. Am., 72*, 1867-1879.

Hanks, T. C. and W. Thatcher (1972), A graphical representation of seismic source parameters, *J. Geophys. Res., 77*, 4393-4405.

Hough, S. E. (1997), Empirical Green's function analysis: Taking the next step, *J. Geophys. Res., 102*(B3), 5369-5384.

Ide, S., and G. C. Beroza (2001), Does apparent stress vary with earthquake size?, *Geophys. Res. Lett., 28*, 3349-3352.

Ide, S., G. C. Beroza, S. G. Prejean, and W. L. Ellsworth (2003), Apparent break in earthquake scaling due to path and site effects on deep borehole recordings, *J. Geophys. Res., 108*(B5), 2271, doi:10.1029/2001JB001617.

Imanishi, K., and W. Ellsworth (2006), Source scaling relationships of microearthquakes at Parkfield, CA, determined using the SAFOD pilot hole seismic array, in *Earthquakes: radiated energy and the physics of faulting*, Geophysical Monograph Series, 170, 81-90, doi:10.1029/170GM10.

Kanamori, H, J. Mori, E. Hauksson, T. H. Heaton, L. K. Hutton and L. M. Jones (1993), Determination of earthquake energy release and ML using TERRAscope, *Bull. Seism. Soc. Am., 83*, 330-346.

Kanamori, H. and L. Rivera (2004), Static and Dynamic Scaling Relations for Earthquakes and Their Implications for Rupture Speed and Stress Drop, *Bull. Seism. Soc. Am., 94*, 314-319.

Ma, S., S. Custodio, R. J. Archuleta, and P. Liu (2008), Dynamic modeling of the Mw 6.0 Parkfield, California, earthquake, *J. Geophys. Res., 113* (B02301), doi:10.1029/2007JB005216.

Malagnini, L., L. Scognamiglio, A. Mercuri, A. Akinci, and K. Mayeda (2008), Strong evidence for non-similar earthquake source scaling in central Italy, *Geophys. Res. Lett., 35,* L17303, doi:10.1029/2008GL034310.

Mayeda, K. (1993), Mb(LgCoda): A stable single station estimator of magnitude, *Bull. Seism. Soc. Am., 83*, 851-861.

Mayeda, K., and W. R. Walter (1996), Moment, energy, stress drop, and source spectra of western United States earthquakes from regional coda envelopes, *J. Geophys. Res., 101*(B5), 11195 – 11208.

Mayeda, K., A Hofstetter, J. L. O'Boyle and W. R. Walter (2003), Stable and transportable regional magnitudes based on coda-derived moment rate spectra, *Bull. Seism. Soc. Am., 93*, 224-239.

Mayeda, K., R. Gok, W. R. Walter, and A. Hofstetter (2005), Evidence for non-constant energy/moment scaling from coda-derived source spectra, *Geophys. Res. Lett., 32,* L10306, doi:10.1029/2005GL022405.

Mayeda, K., L. Malagnini, and W. R. Walter (2007), A new spectral ratio method using narrow band coda envelopes: Evidence for non-self-similarity in the Hector Mine sequence, *Geophys. Res. Lett., 34*, L11303, doi:10.1029/2007GL030041.

Morasca, P., K. Mayeda, L. Malagnini and W. R. Walter (2005), Coda-derived source spectra, moment magnitudes and energy-moment scaling in the western Alps, *Geophys. J. Int., 160,* 263-275.

Mori, J., R. E. Abercrombie, and H. Kanamori (2003), Stress drops and radiated energies of aftershocks of the 1994 Northridge, California, earthquake, *J. Geophys. Res., 108*(B11), 2545, doi:10.1029/2001JB000474.

Mueller, C. S. (1985), Source pulse enhancement by deconvolution of an empirical Green's function, *Geophys. Res. Lett., 12*(1), 33-36.

Prieto, G. A., P. M. Shearer, F. L. Vernon, and D. Kilb (2004), Earthquake source scaling and self-similarity estimation from stacking P and S spectra, *J. Geophys. Res., 109*, B08310, doi: 10.1029/2004JB003084.

Singh, S. K., and M. Ordaz (1994), Seismic energy release in Mexican subduction zone earthquakes, *Bull. Seism. Soc. Am., 84*, 1533– 1550.

Takahashi, T., H. Sato, M. Ohtake and K. Obara (2005), Scale dependence of apparent stress for earthquakes along the subducting Pacific plate in northeastern Honshu, Japan, *Bull. Seism. Soc. Am., 95*, 1334-1345, doi: 10.1785/0120040075.

Venkataraman, A., L. Rivera and H. Kanamori (2002), Radiated Energy from the 16 October 1999 Hector Mine Earthquake: Regional and Teleseismic Estimates, *Bull. Seism. Soc. Am., 92*, 1256-1265, doi: 10.1785/0120000929.

Walter, W. R., K. M. Mayeda, R. Gok and A. Hofstetter (2006), The scaling of seismic energy with moment: simple models compared with observations, in *Earthquakes: radiated energy and the physics of faulting*, Geophysical Monograph Series, 170, 25-41, doi:10.1029/170GM05.

Wyss, M., (1970), Stress estimates for South American shallow and deep earthquakes, J. *Geophys. Res., 75,* 1529-1544.

Yamada, T., J. J. Mori, S. Ide, R. E. Abercrombie, H. Kawakata, M. Nakatani, Y. Iio, and H. Ogasawara (2007), Stress drops and radiated seismic energies of microearthquakes in a South African gold mine, *J. Geophys. Res., 112*, B03305, doi:10.1029/2006JB004553.

Appendix 1: Data tables of events studied.

Table 2.2 Hector Mine 1999

Catalog Information							Determined Parameters										
Date	Time	Lat.	Long.	No.	Cat. Mag	Cat M_o (Nm)	E_R (J)	E_R/M_o x10^{-5}	τ_a	STD	SDE	M_o spectra	f_c	1σ conf.	σΔ (MPa)	1σ conf.
1999-10-16	9:46:44.13	34.59	-116.27	1	7.10	5.01E+19	6.06E+15	12.1	4.39	0.26	0.062	5.01E+19	0.12	0.02	16.02	0.06
1999-10-16	9:59:35.39	34.68	-116.29	2	5.77	5.07E+17	1.79E+13	3.5	1.28	0.26	0.065	1.58E+18	0.25	0.08	2.52	0.23
1999-10-16	12:57:21.06	34.44	-116.25	3	5.37	1.27E+17	1.37E+13	10.8	3.91	0.22	0.049	1.48E+17	0.80	0.07	12.24	0.22
1999-10-22	16:8:48.05	34.87	-116.41	4	4.99	3.43E+16	1.16E+12	3.4	1.23	0.13	0.030	4.93E+16	0.55	0.06	2.03	0.19
1999-10-21	1:54:34.17	34.87	-116.39	5	4.98	3.31E+16	1.52E+12	4.6	1.66	0.21	0.052	6.94E+16	0.61	0.11	2.49	0.32
1999-10-16	17:38:48.65	34.43	-116.25	6	4.92	2.69E+16	5.10E+11	1.9	0.69	0.22	0.054	1.35E+16	1.37	0.06	5.09	0.19
1999-10-16	10:20:52.66	34.36	-116.15	7	4.76	1.55E+16	1.04E+12	6.7	2.44	0.39	0.272	2.94E+16	1.20	0.23	4.96	0.68
1999-10-25	18:26:0.63	34.62	-116.24	8	4.63	9.89E+15	2.10E+11	2.1	0.77	0.10	0.023	7.70E+15	0.99	0.10	2.03	0.31
1999-10-19	12:20:44.27	34.71	-116.34	9	4.49	6.10E+15	1.27E+11	2.1	0.75	0.18	0.041	2.30E+15	2.53	0.09	6.44	0.26
1999-11-14	14:20:9.41	34.84	-116.41	10	4.42	4.79E+15	1.42E+11	3.0	1.08	0.27	0.063	4.45E+15	1.76	0.30	3.43	0.90
1999-10-18	11:2:19.91	34.86	-116.35	11	4.35	3.76E+15	4.11E+10	1.1	0.40	0.24	0.059	4.17E+15	1.50	0.21	1.66	0.62
1999-10-16	13:51:17.62	34.45	-116.23	12	4.24	2.57E+15	8.64E+10	3.4	1.22	0.29	0.070	1.88E+15	3.08	0.28	7.06	0.85
1999-10-16	11:27:53.76	34.37	-116.14	13	4.18	2.09E+15	7.68E+10	3.7	1.33	0.18	0.048	8.57E+14	3.89	0.35	10.54	1.06
1999-10-22	12:40:52.53	34.34	-116.21	14	4.11	1.64E+15	5.22E+10	3.2	1.15	0.00	0.000	8.92E+14	3.39	0.48	5.80	1.43
Stack1	--	--	--	S1	3.90	8.06E+14	2.41E+10	3.0	1.09	0.33	0.074	7.14E+14	2.90	0.10	3.08	0.31
Stack2	--	--	--	S2	3.50	2.68E+14	8.81E+09	3.3	1.19	0.34	0.076	3.02E+14	3.60	0.14	2.57	0.43
Stack3	--	--	--	S3	3.25	9.42E+13	2.96E+09	3.1	1.14	0.25	0.057	1.15E+14	5.18	0.25	2.97	0.75
Stack4	--	--	--	S4	3.00	4.55E+13	1.63E+09	3.6	1.30	0.24	0.053	6.43E+13	6.93	7.26 E-09	4.00	2.18 E-08

Table 2.3 Parkfield 2004

Catalog Information							Determined Parameters									
Date	Time	Lat.	Long.	No.	Cat. M_w	M_o (Nm)	E_R (J)	E_R/M_o x10^{-5}	τ_a	STD	SDE	M_o spectra	f_c	1σ conf.	σΔ (MPa)	1σ conf.
2004-9-28	17:15:25.09	35.81	-120.38	1	6.00	1.12E+18	8.10E+13	7.2	2.62	0.10	0.023	1.12E+18	0.37	0.03	9.04	0.09
2004-9-29	17:1:4.96	35.89	-120.51	2	5.04	4.07E+16	2.85E+12	7.0	2.54	0.12	0.027	1.10E+17	0.56	0.05	3.14	0.14
2004-9-28	17:24:15.4	35.80	-120.36	3	4.91	2.60E+16	1.18E+12	4.5	1.64	0.17	0.037	8.77E+16	0.62	0.09	2.34	0.28
2004-9-30	18:54:30.28	35.91	-120.53	4	4.89	2.43E+16	2.47E+12	10.2	3.69	0.15	0.032	6.47E+16	0.78	0.09	4.63	0.28
2005-5-16	7:24:38.07	35.89	-120.48	5	4.65	1.06E+16	4.82E+11	4.5	1.65	0.16	0.034	1.48E+16	1.07	0.07	3.22	0.22
2004-11-29	1:54:14.3	36.00	-120.52	6	4.59	8.61E+15	2.54E+11	3.0	1.07	0.17	0.037	5.84E+15	1.68	0.11	4.59	0.33
2004-9-28	19:31:27.79	35.83	-120.40	7	4.31	3.27E+15	1.38E+11	4.2	1.53	0.21	0.046	2.61E+15	2.28	0.07	5.34	0.22
Stack1	--	--	--	S1	4.00	1.33E+15	1.05E+11	7.8	2.85	0.20	0.043	1.85E+15	2.46	0.10	5.08	0.30
Stack2	--	--	--	S2	3.75	4.12E+14	2.13E+10	5.2	1.88	0.20	0.044	5.29E+14	3.39	0.18	3.72	0.54
Stack3	--	--	--	S3	3.35	1.13E+14	8.11E+09	7.2	2.61	0.35	0.077	1.90E+14	5.12	0.21	4.70	0.64
Stack4	--	--	--	S4	3.15	5.56E+13	3.69E+09	6.6	2.41	0.26	0.056	9.90E+13	6.48	8.54 E-10	5.06	2.56 E-09

Table 2.4 Wells, NV 2008

Catalog Information							Determined Parameters									
Date	Time	Lat.	Long.	No.	Cat. M_w	M_o (Nm)	E_R (J)	E_R/M_o x10^{-5}	τ_a	STD	SDE	M_o spectra	f_c	1σ conf.	σΔ (MPa)	1σ conf.
2008-2-21	14:16:2.71	41.15	-114.87	1	6.00	1.12E+18	1.14E+14	10.1	3.67	0.11	0.020	1.12E+18	0.42	0.13	14.91	0.39
2008-2-21	14:20:51.63	41.11	-114.90	2	4.80	1.78E+16	7.88E+11	4.4	1.61	0.17	0.032	1.68E+17	0.92	0.29	8.67	0.88
2008-2-21	23:57:51.01	41.15	-114.93	3	4.60	8.91E+15	2.57E+11	2.9	1.05	0.06	0.014	1.72E+16	1.62	0.10	12.94	0.29
2008-2-22	23:27:45.26	41.10	-114.92	4	4.30	3.16E+15	1.13E+11	3.6	1.29	0.10	0.020	4.26E+15	2.52	0.19	16.25	0.57
2008-2-27	7:59:38.21	41.19	-114.83	5	4.10	1.58E+15	1.02E+11	6.5	2.34	0.12	0.022	2.16E+15	3.27	0.42	22.18	1.25
2008-2-21	14:34:41.87	41.00	-114.79	6	4.10	1.58E+15	1.51E+11	9.5	3.46	0.09	0.017	4.14E+15	2.51	0.26	18.46	0.77
2008-2-28	15:10:37.74	41.16	-114.93	7	4.00	1.12E+15	5.30E+10	4.7	1.72	0.15	0.027	1.93E+15	4.22	0.24	23.65	0.72

2008-2-22	1:50:5.23	41.14	-114.92	8	3.90	7.94E+14	2.49E+10	3.1	1.14	0.10	0.018	1.29E+15	3.63	0.23	13.20	0.70
Stack1	--	--	--	S1	3.65	3.35E+14	1.49E+10	4.5	1.62	0.13	0.024	4.48E+14	6.27	0.49	23.10	1.46
Stack2	--	--	--	S2	3.25	7.94E+13	3.16E+09	4.0	1.44	0.08	0.015	2.49E+14	5.80	0.11	9.15	0.32
Stack3	--	--	--	S3	3.00	4.22E+13	2.41E+09	5.7	2.08	0.09	0.017	1.45E+14	7.83	0.12	12.90	0.36
Stack4	--	--	--	S4	2.85	2.02E+13	1.51E+09	7.5	2.71	0.09	0.017	9.25E+13	9.08	1.31 E-08	13.02	3.93 E-08

Table 2.5 Cerro Prieto 2008

Catalog Information							Determined Parameters									
Date	Time	Lat.	Long.	No.	Cat. M_w	M_o (Nm)	E_R (J)	E_R/M_o x10^{-5}	τ_a	STD	SDE	M_o spectra	f_c	1σ conf.	σΔ (MPa)	1σ conf.
2008-2-9	7:12:4.5	32.36	-115.28	1	5.10	5.01E+16	1.41E+12	2.8	1.02	0.14	0.026	5.01E+16	0.77	0.03	3.77	0.08
2008-2-11	18:29:30.5	32.33	-115.26	2	5.10	5.01E+16	7.72E+11	1.5	0.56	0.08	0.015	3.65E+16	0.74	0.05	2.67	0.16
2008-2-19	22:41:29.7	32.43	-115.31	3	5.01	3.67E+16	6.23E+11	1.7	0.62	0.08	0.014	3.86E+16	0.87	0.10	3.05	0.30
2008-11-20	19:23:1.4	32.36	-115.36	4	4.98	3.31E+16	5.17E+11	1.6	0.57	0.15	0.029	1.31E+16	1.40	0.12	5.19	0.37
2008-2-12	4:32:39.2	32.45	-115.32	5	4.97	3.20E+16	6.25E+11	2.0	0.71	0.08	0.014	2.62E+16	1.00	0.12	3.69	0.37
2008-2-20	1:28:55.4	32.43	-115.31	6	4.83	1.97E+16	2.45E+11	1.2	0.45	0.10	0.019	8.65E+15	1.35	0.09	3.56	0.27
2008-9-5	21:54:33.6	32.35	-115.23	7	4.63	9.89E+15	7.18E+10	0.7	0.26	0.15	0.027	9.47E+15	0.72	0.04	0.78	0.11
2008-2-12	9:27:19.9	32.46	-115.31		4.45	5.31E+15	6.49E+10	1.2	0.44	0.10	0.018	3.33E+15	1.58	0.14	2.28	0.42
Stack1	--	--	--	S1	4.00	1.12E+15	1.35E+10	1.2	0.44	0.06	0.011	9.88E+14	2.10	0.14	1.56	0.43
Stack2	--	--	--	S2	3.50	2.17E+14	2.91E+09	1.3	0.49	0.09	0.017	1.98E+14	3.68	0.23	1.66	0.68
Stack3	--	--	--	S3	3.25	8.37E+13	1.26E+09	1.5	0.55	0.17	0.032	7.32E+13	5.14	0.21	1.82	0.62
Stack4	--	--	--	S4	3.00	4.17E+13	7.69E+08	1.8	0.67	0.13	0.024	3.77E+13	7.13	5.43 E-11	2.55	1.63 E-10

1. Date — Date of event origin, YEAR-MM-DD
2. Time — Time of event origin, HH:MM:SS.s
3. Lat. — Latitude of event

4. Long.	Longitude of event
5. No.	Event number for larger events. Smaller events are stacked into 4 bins by magnitude. Thus these do not have a specific time or location.
6. Cat Mag	Magnitude from the catalog used
7. Cat M_o	Moment corresponding to above mag: Mw = (log10(Mo)-9.05)/1.5
8. E_R (J)	Radiated Energy, Joules, from all-station stacked spectra
9. E_R/M_o	Scaled Energy, from all-station stacked spectra
10. τ_a (MPa)	Apparent Stress=mu*E_R/M_o, MPa, w/ mu below, from all-station stacked spectra
11. STD (log10)	Standard deviation of estimates at all stations for: E_S, E_S/M_o, ta
12. SDE (log10)	Standard Error of Mean from estimates at all stations for: E_S, E_S/M_o, ta
13. M_o spectra	Moment as determined in the fc fit, used in the SD calculation
14. f_c (Hz)	Corner Frequency from stacked source spectra, in Hz
15. 1σ conf	1-sigma Confidence interval from corner frequency residual fit, log10 units, +/-error bars
16. σΔ (MPa)	Brune Stress Drop, MPa, from moment and corner frequency
17. 1σ conf	1-sigma Confidence interval from fc fit, propagated to Stress Drop, log10 units

Notes:
10. mu = rho*beta^2. Rho=2800; beta=3600; mu= 3.63e+10 Pa;
12. Standard error = standard_deviation/sqrt(n) where n is number of stations
16. Brune_stress_drop = 8.47*Mo*fc^3/beta^3
17. 1sigma-confidence of stress drop is propagated from 1sigma-confindence of corner frequency, so that error(SD)=3*error(fc) because SD~fc^3

CHAPTER 3

Variability in Earthquake Stress Drop and Apparent Stress

Abstract

We apply empirical Green's function coda-based analysis to four earthquake sequences in Japan that span a magnitude range of *1.8* to *6.9*, to measure radiated energy, corner frequency and stress drop. We find no systematic dependence of apparent stress or stress drop on seismic moment for these sequences, and find they both are log-normally distributed; however, we identify several anomalous events – both energetic and enervated – that show sharply different spectral signatures from the rest of the population. These events indicate that much of the variation in apparent stress and stress drop is statistically significant, which may have important implications for seismic hazard analysis.

3.1 Introduction

Large earthquake populations reveal strong variations in stress drop, but little in the way of systematic behavior or dependence on seismic moment [e.g. *Aki*, 1972; *Hanks*, 1977; *Allmann and Shearer*, 2009]. Because static stress drop measurements depend on the corner frequency cubed, small uncertainties in corner frequency map into large uncertainties in the stress drop, and it's often unclear how much of this variability is

Baltay, A., S. Ide, G. Prieto, and G.Beroza (2011), Variability in earthquake stress drop and apparent stress, *Geophys. Res. Lett*., **38**, L06303, doi:10.1029/2011GL046698.

due to measurement error, rather than variability in source properties [*Sonley and Abercrombie*, 2006; *Prieto et al.*, 2007].

We expand on *Baltay et al.*, [2010] to measure seismic energy, corner frequency, and stress drop, using an empirical Green's function (eGf) coda based measurement that provides stable and robust source spectra. We apply this approach to four earthquake sequences in Honshu, Japan that are well recorded by seismic networks. As in *Baltay et al.* [2010], we find no systematic variation of apparent stress or stress drop with seismic moment; however, we do find several anomalous events with unusually high or low stress drops. The energetic events could have high stress drop and/or high rupture velocity, suggesting there could be a population of "rogue" earthquakes that have particularly intense strong ground motion for their size.

3.2 Empirical Green's Function Coda Spectrum Method

We follow *Baltay et al.* [2010] to create coda-based source spectra with path effects removed through an eGf correction. We apply it to each station individually, then stack spectra over all stations for each earthquake.

Narrowband envelopes are created from horizontally averaged displacement records. Non-dimensional coda spectra are constructed from the average envelope over a constant 20-second time window in the coda starting at the S-wave arrival. In Japan, we found a simple 20-second window reduced the inter-station scatter of scaled energy as much as the variable window lengths used in *Baltay et al.*, [2010], due to both better station coverage and borehole recordings for the smaller events.

We use the smallest event as an eGf, assuming an ideal Brune ω^{-2} spectrum, as in *Baltay et al.*, [2010] Eq. (1). For the eGf event we estimate corner frequency based on the Japan Meteorological Agency (JMA) magnitude and Eq. (3) of *Baltay et al.,* [2010], assuming a stress drop of 3MPa. We model the eGf event with a Brune spectrum; if we use a *Boatwright* [1980] spectra model instead, apparent stress increases by about 10% for all events. However, these assumptions are made for the eGf event only.

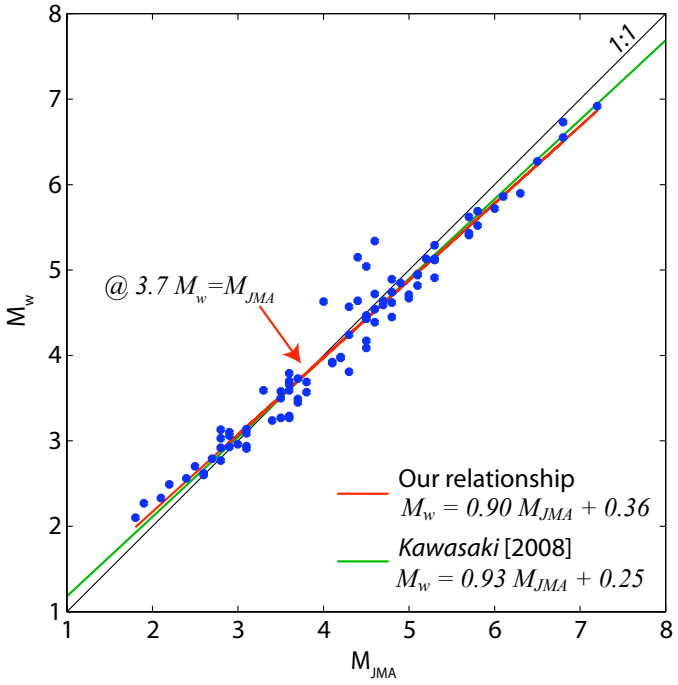

Figure 3.1 Relationship between M_w from moments determined here, and M_{JMA} from the catalog information. The two magnitudes are the same at M=3.7. Above that, the JMA magnitude over estimates the moment magnitude, and below 3.7 the JMA magnitude underestimates. The relationship from our data is very similar to that found in a larger study by *Kawasaki et al.,* [2008].

The spectra for the other earthquakes are sequentially corrected to remove path effects. To convert the coda spectra to absolute displacement spectra, we use the independently determined seismic moment of each main shock, from the National Research Institute for Earth Science and Disaster Prevention (NIED) in Section 4, below. The corrected spectral level then sets the moment, and M_w, of each smaller event. Getting a corrected M_w is important for earthquakes in Japan, especially smaller events without independent waveform modeling, as the Japanese Meterological Association magnitudes (M_{JMA}) are known to not correspond directly to M_w. We investigate the relationship between M_w and M_{JMA}, and find that they correspond at magnitude 3.7. The difference between the two magnitudes is the greatest for large events, M>6, for which the average $M_{JMA} - M_w = 0.21$. For small events M_{JMA} underestimates the magnitude, so that the mean difference is -0.09 for M<3. The relationship for our data of $M_w = 0.90\ M_{JMA} + 0.37$ is very similar to that of *Kawasaki et al.,* [2008], $M_w = 0.93\ M_{JMA} + 0.25$, who used many shallow crustal events in Japan (Figure 3.1).

We extrapolate the source spectra to the high and low frequencies and estimate the radiated seismic energy as

$$E_R = \frac{I}{4\pi^2 \rho \beta^5} \int_0^\infty \left| \omega \cdot \dot{M}(\omega) \right|^2 d\omega \quad , \qquad (1)$$

with $\dot{M}(\omega)$ the displacement source spectra, ρ =2800 kg/m^3, β = 3600 m/s (except for the Kamaishi sequence, where β = 4400 m/s), and I, the average mean-squared S-wave radiation pattern coefficient, assumed to be *2/5* [*Boore and Boatwright*, 1984].

3.3 Source Parameter Estimation

Once we determine the stacked source spectra, we model the spectral shape to determine the corner frequency. Each spectrum is fit with a Brune ω^{-2} model

$$u(f) = \frac{M_o}{1 + (f / f_c)^2}. \tag{2}$$

The corner frequency is found by minimizing the L-2 norm of the residuals. Using the circular crack model of *Eshelby* [1957] and the relationship between source dimension and corner frequency from *Brune* [1970], stress drop, moment and corner frequency are related as

$$\Delta\sigma = \frac{7M_o}{16}\left(\frac{2\pi f_c}{2.34\beta}\right)^3. \tag{3}$$

We compare Brune static stress drop ($\Delta\sigma$) to apparent stress, ($\tau_a = \mu\, E_R/M_o$) [*Wyss and Brune*, 1968]. Using the above assumptions under self-similarity, the theoretical relationship is

$$\frac{\Delta\sigma}{\tau_a} = 4.3, \tag{4}$$

[*Singh and Ordaz*, 1994].

For the larger events, we fit a Brune spectral model to measure the corner frequency. Fitting with a Boatwright spectral model yields negligible differences; however, the relationship between corner frequency and stress drop is model dependent [e.g. *Sonley and Abercrombie*, 2006]. Here we use a Brune stress drop, which allows for a straightforward comparison of our results with other studies.

3.4 Four Study Areas in Honshu, Japan

Our eGf method requires earthquakes close enough to share common path effects. We analyze four sequences in northern Honshu, Japan including three large main shock-aftershock sequences (Figure 3.2). We use only co-located, borehole recordings from Hi-net broadband and KiK-net strong motion network, which allows us to extend the analysis to higher frequencies and smaller magnitudes than possible from surface observations. In each sequence, only events recorded at 10 or more stations are analyzed, with 17 to 18 stations total for each sequence, an aggregate of 89 events.

The 2004 M_w *6.6* Chuetsu (mid Niigata) earthquake occurred in a highly active area of western Honshu at a depth of 13 km. The aftershock sequence was especially rich, with events of M_{JMA} *6.5*, *6.3* and *6.0*, and hundreds of smaller and intermediate-sized events, occurring on a complex system consisting of five reverse faults [*Hikima and Koketsu*, 2005]. We analyze 32 events total, at 18 stations. The mainshock moment determined by NIED is 7.5×10^{18} N-m, or M_w 6.55.

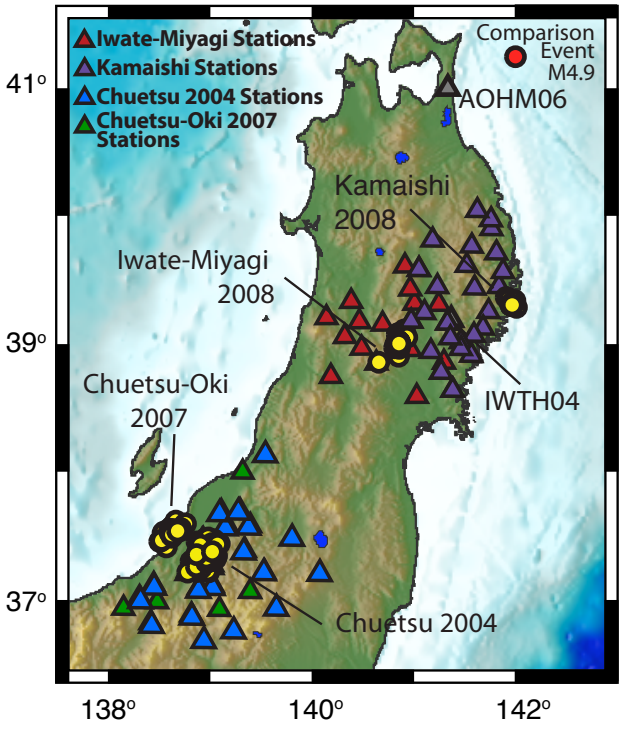

Figure 3.2 Event (yellow circles) and station (triangles) locations. Stations from two studies may overlap. Kamaishi comparison event (Fig. 4) in top right (circle).

The 2007 M_w *6.7* Chuetsu-Oki sequence received much attention due to its impact on the Kashiwazaki Kariwa nuclear power plant. The main shock and aftershocks occurred offshore Niigata prefecture on a shallow, southeast dipping thrust fault, with depths of 15-20 km [*Miyake et al.*, 2010]. We analyze 15 events in this sequence, recorded at 17 stations, with a mainshock seismic moment of 1.42×10^{19} N-m, or M_w *6.73* (NIED).

The 2008 M_w *6.9* Iwate-Miyagi Nairiku earthquake occurred between the Iwate and Miyagi prefectures in central northern Honshu at 8 km depth on a shallow inland crustal reverse fault, and is well known for a recorded acceleration in excess of 4 g [*Yamada et al.*, 2009]. The moment of the main shock is 2.7×10^{19} N-m (NIED), M_w *6.92*. We analyze 27 aftershocks at depths up to 12 km, recorded at 17 stations.

The repeating earthquake sequence offshore of Kamaishi, Iwate, has a main shock magnitude of 4.9 +/- 0.2 and recurs every 5 to 6 years. Between repeats, many smaller earthquakes rupture similar patches located on the deepest part of the inter-plate main thrust zone, at about 50 km depth [*Uchida et al.*, 2010]. The 2008 Kamaishi main event (08:00 on 01/11/2008) has moment 1.035×10^{16} N-m, M_w *4.64* [CMT catalog; Coordinating Committee for Earthquake Prediction in Japan, 2008]. We use the 16 events that have occurred since the local installation of 17 Hi-net stations in the area in 2002.

3.5 Radiated Energy and Apparent Stress Results

Scaled energies, E_R/M_o, for each sequence are compared to previous studies (Figure 3.3b). In all four sequences, the apparent stress shows no significant trend with moment. The best-fit parameters include zero-slope (no scaling) within the uncertainties. In particular, the radiated energy of the Chuetsu main shock is 2.9×10^{14} J, which falls between the USGS estimate of 1.4×10^{14} J (following *Boatwright and Choy*, 1986) and the estimate of 3.2×10^{14} J from *Izutani* [2005]. Our energy results and independent moment calculations from two of the larger aftershocks (*M5.7* and *M5.3*) compare closely with those of *Izutani* [2005]. Energy of the Chuetsu Oki 2007 main shock is 1.9×10^{15} J, larger than the USGS estimate of 1.4×10^{14} J, as is that of the Iwate-Miyagi main shock with a radiated energy of 1.8×10^{15} J compared to USGS energy estimate of 2.6×10^{14} J. In some of the sequences, we find that the main shock has higher scaled energy than most aftershocks.

Figure 3.3b reveals no obvious trend of increasing apparent stress over eight orders of magnitude in seismic moment. These four sequences follow the same scatter and mean as those of *Baltay et al.* [2010] for sequences in the Western US as well as the compilation

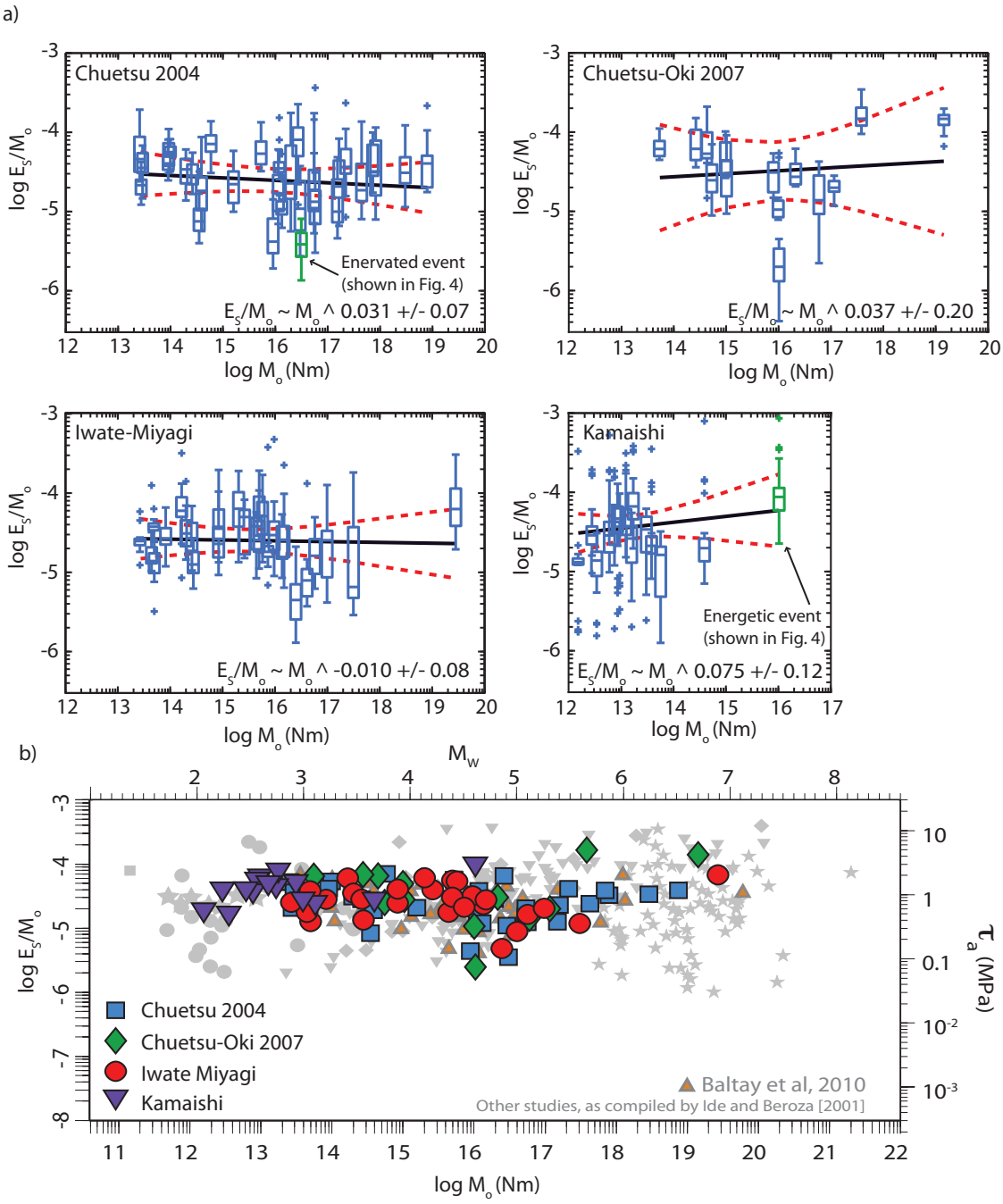

Figure 3.3 (a) Inter-station data range given by the non-parametric box and whisker plot: middle bar is the median; box indicates the 25th and 75th percentiles, the difference of which is the interquartile range; whiskers show distance to the farthest data point within 1.5x interquartile range; and pluses are outlying data. For most events, whiskers are small with few outliers, showing tight inter-station scatter. Black line is L2 norm fit of the mean scaled energy; red dashed lines are 95% confidence on the fit parameters. (b) Scaled energy and apparent stress for all events taken together, overlain on *Ide and Beroza* [2001] and *Baltay et al.* [2010] from the western United States.

of *Ide and Beroza* [2001]. Overall, apparent stress has a log mean of 1.15 MPa and log standard deviation of 0.95, very consistent with many previous studies that find an apparent stress near 1 MPa [*Ide and Beroza,* 2001].

3.6 Stress Drop Results

We find that Brune stress drop is log-normally distributed with a mean of 5.92 MPa. There is no dependence of stress drop on moment, however there are several events with stress drops higher than average, as well as events with very low stress drops (Figure 3.4). The Kamaishi sequence has higher stress drops, which may be due to the deeper

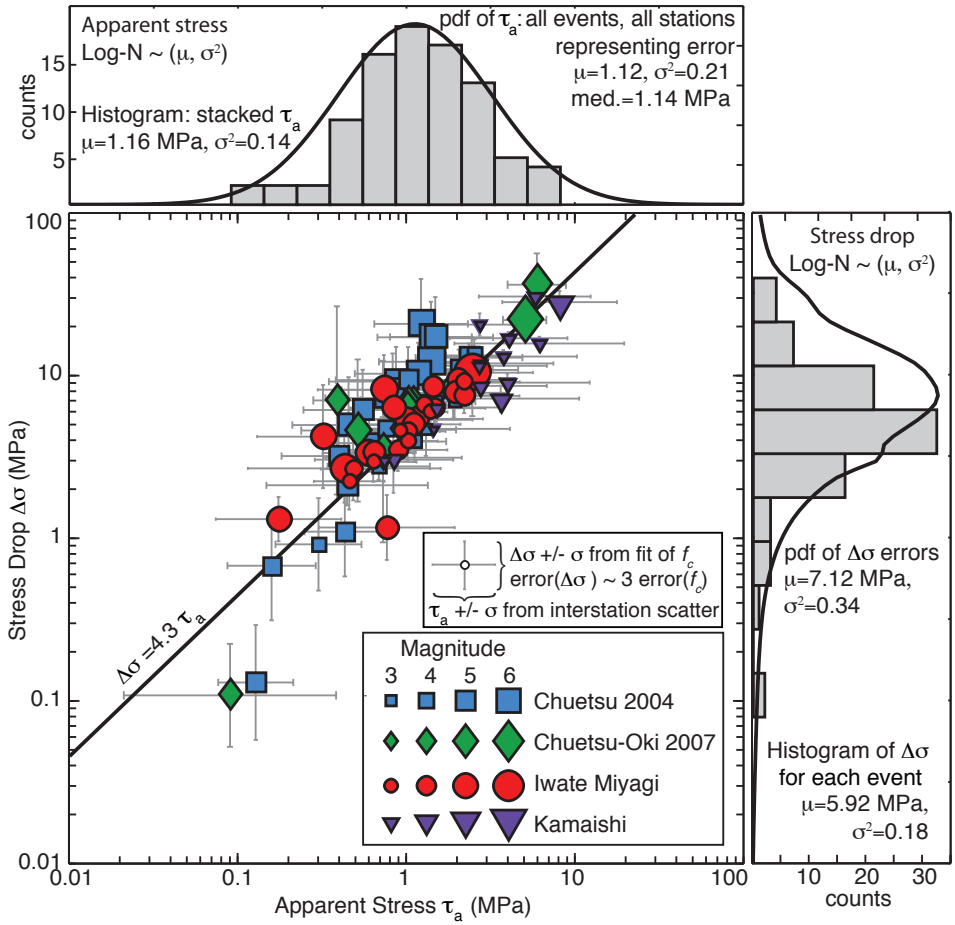

Figure 3.4 Apparent stress compared to stress drop with error bars, showing theoretical relation in black line. Enervated earthquakes have lower stress drop and apparent stress than expected (lower left) while energetic earthquakes have higher stresses (upper right). Histograms show log-normal distributions of events. Solid lines include the effect of station-to-station variation (apparent stress) and uncertainties in measurements (stress drop).

location of the events. While the mean value of stress drop is dependent and positively correlated with the assumed 3 MPa stress drop of the eGf, the distribution, relative variations, and the lack of scaling are not affected by the assumed eGf parameters (Figure 3.5).

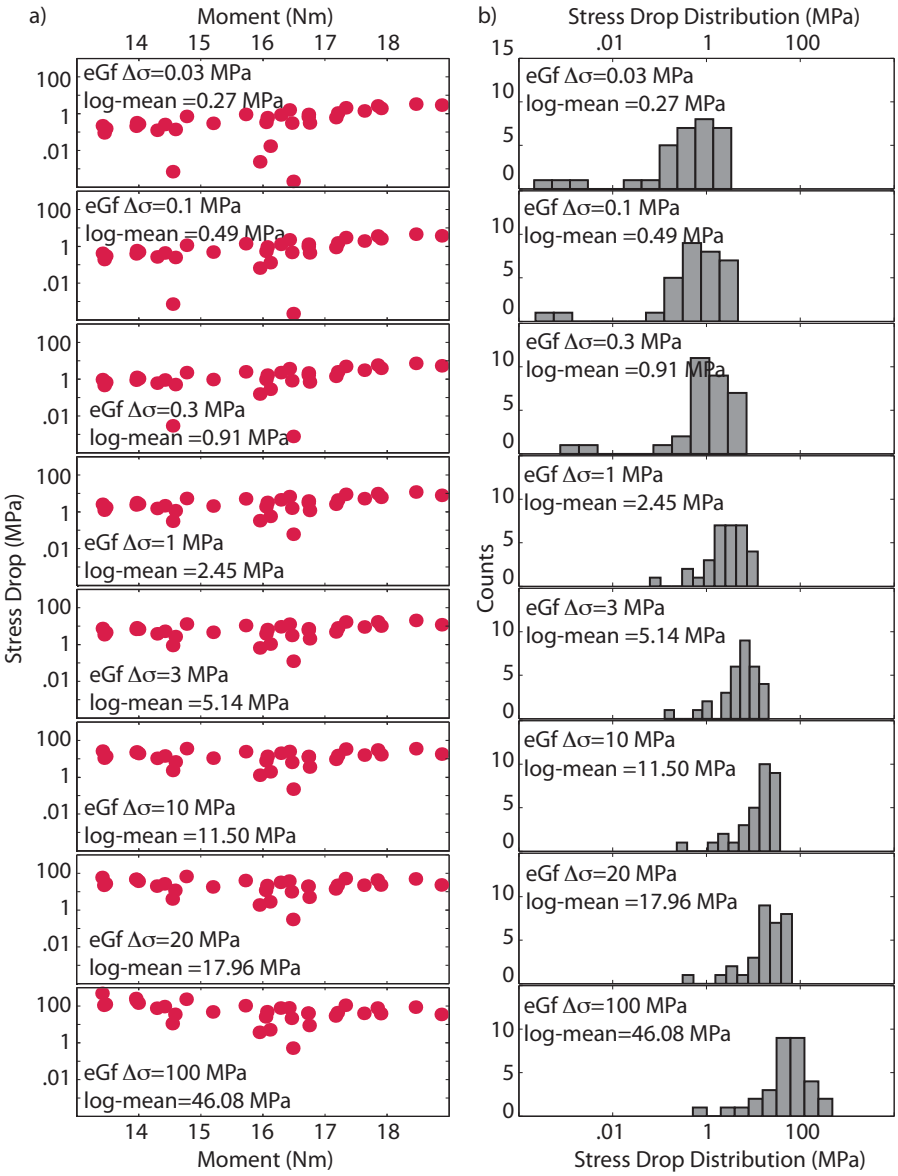

Figure 3.5 Effect of assumed stress drop of the eGf event. In each case, the eGf is assumed to have a certain stress drop, which sets the corner frequency and Brune shape of the eGf event. The rest of the spectra are then corrected iteratively by that eGf, and corner frequencies and stress drops are determined for all of the events. While the mean value of stress drop is dependent and positively correlated with the assumed stress drop of the eGf, the distribution, relative variations, and the lack of scaling are not affected by the assumed eGf parameters.

Our comparisons of stress drop and apparent stress are generally consistent with the relationship expected for constant stress drops, with the exception of two enervated events. The departure of some events from the expected ratio $\Delta\sigma/\tau_a = 4.3$ is due to higher corner frequencies of the spectra, which render higher stress drops than expected given the apparent stress. When considering the error, almost all of the events fall on the expected line (Figure 3.4).

The Kamaishi stress drop results are consistent with other findings on this repeating sequence. *Uchida et al.* [2010] found the smaller earthquakes in the sequence to have stress drops between 3 and 11 MPa, with a stress drop of 27 MPa for the 2008 main event. We find a stress drop of 28.72 MPa for the same 2008 main event, and a mean of 9.59 MPa for the rest of the Kamaishi events.

Our findings of non-scaling stress drop with moment, but with variations in stress drop values, are consistent with other studies. For global earthquakes from M_w *5.2* to *8.3*, *Allman and Shearer* [2009] estimated stress drops ranging from 0.3 to 50 MPa, with the median value of 4 MPa independent of moment. *Oth et al.* [2010] find a mean Brune stress drop of 1.1 MPa for crustal events ranging from M_{JMA} *2.7 – 8* in Japan, with stress drops ranging from 0.1 to nearly 100 MPa.

3.7 Energetic and Enervated Events

While our results point to a lack of scaling of either apparent stress or stress drop with moment, we find statistically significant departures from the average. Overall, both apparent stress and stress drop are log-normally distributed, as are their errors. This is not due to any shortcomings in the measurements, but rather because earthquakes do display real variations. To emphasize this variation, we highlight two particular events: an energetic event, as well as an enervated earthquake.

The M_w *4.64* Kamaishi main event from 2008 (left column of Figure 3.6) is highly energetic. The broadband record is similar in both amplitude and signature to a typical event at a similar depth on the same plate interface (column 2 of Figure 3.6); however, the low frequencies of the Kamaishi event are depleted, while the high frequencies of the

energetic Kamaishi earthquake are enriched. The main Kamaishi event has an apparent stress of 8.2 MPa, the highest of any event in this study, and a stress drop of 28.7 MPa.

The M_w *4.95* enervated event from the Chuetsu 2004 sequence (column 3 of Figure 3.6) has an apparent stress of only 0.12 MPa and low stress drop of 0.12 MPa, due to a low corner frequency of 0.24 Hz. While the low frequency record of the enervated event is very similar, in both amplitude and phase, to a standard event (column 4 of Figure 3.6), the broadband record has a different signature and a slower start than a typical event. The

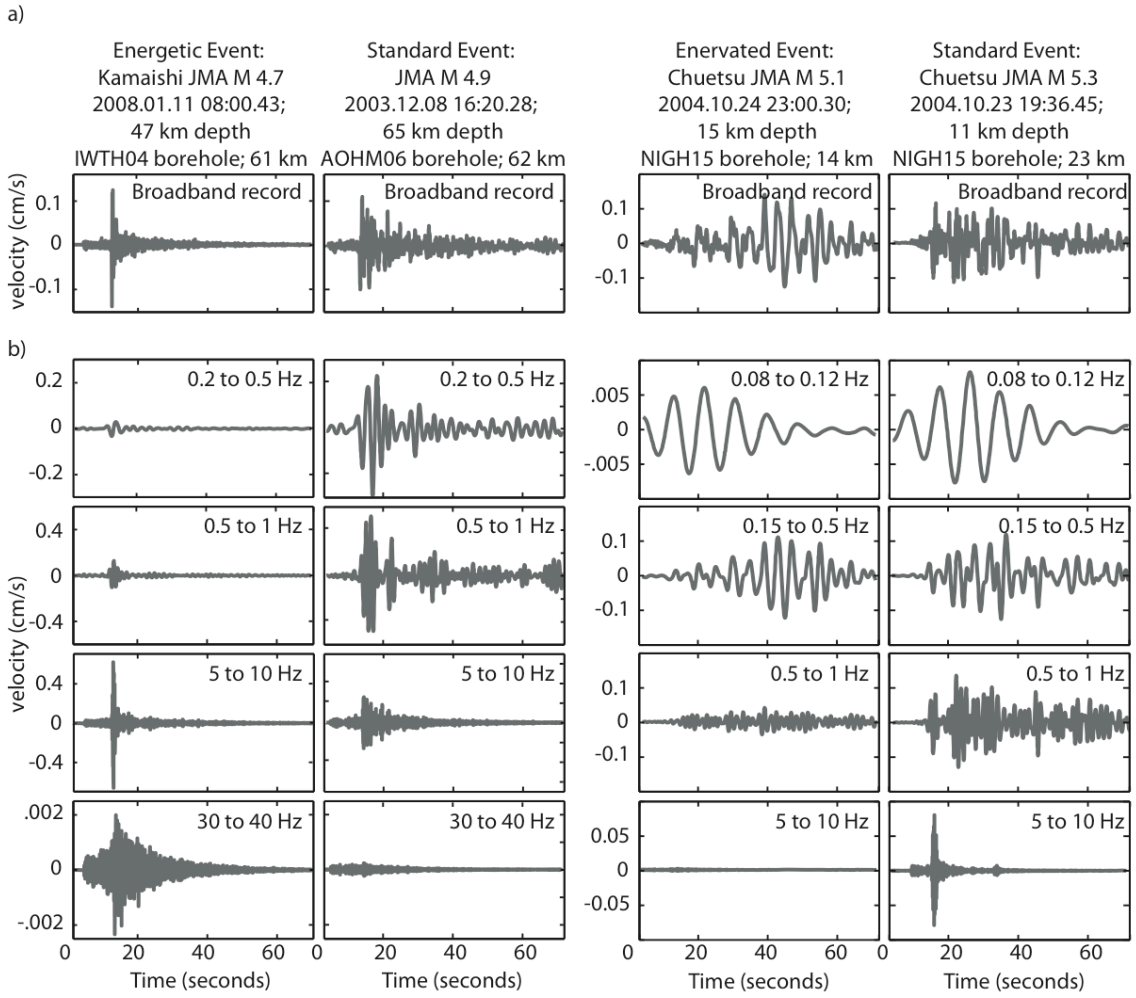

Figure 3.6 Anomalous energetic and enervated events: Kamaishi 2008 main event (column 1) and enervated event from Chuetsu 2004 sequence (column 3). Comparison events with same mechanism, similar magnitude, and similar event-station distance in column 2 and 4. A) Broadband borehole velocity seismograms, and b) Bandpassed seismograms. Pass bands are different in the energetic vs. enervated series to highlight the different trends.

event from Chuetsu 2007 of *Mw 4.64* has an apparent stress of 0.09 MPa and stress drop of 0.11 MPa, with a similarly low corner frequency of 0.31 Hz. These low values are comparable to those found for slow oceanic transform fault earthquakes [*Perez-Campos*, 2003].

These enervated and energetic events are not outliers due to difficulties or shortcomings in data processing; rather, their waveforms confirm that they are genuinely anomalies with energies and stress drops well outside the main population. While the enervated events may be scientifically interesting slow earthquakes, they are of little concern for seismic risk. The energetic events, however, have more high-frequency energy than otherwise predicted for their size. Understanding the origin of this high-frequency energetic event is important for accurate prediction of strong ground motion at low probability thresholds. The possibility that main shocks may also be slightly more energetic than their aftershocks could be important in hazard assessment, as the two groups of events are sometimes considered separately in ground motion prediction.

3.8 Conclusions

We estimate radiated energy and apparent stress of four earthquake sequences in Honshu, Japan, ranging from magnitude *1.8* to M_w *6.9*, using the methodology of *Baltay et al.* [2010]. The spectra are modeled to measure corner frequency and Brune stress drop. Overall, we find no dependence of apparent stress or stress drop on moment. The confidence on the best best-fit linear relationship between $\log_{10} E_S$ and $\log_{10}$ apparent stress includes a zero-slope, no dependence on moment, for each sequence. Apparent stress and stress drop follow the expected theoretical relationship. For all four sequences in aggregate, the mean apparent stress is 1.15 MPa, the scaled energy ratio is 2.96×10^{-5}, and the mean stress drop is 5.92 MPa.

Our results support a self-similar earthquake model and current practice of using a constant stress drop assumption for strong ground motion prediction. By utilizing the coda waves and averaging over many stations, we make robust estimations of the energy and stress drop of each event. Observations of scaled energy with moment show no

significant statistical departure from zero dependence. Many other studies that find a dependence of scaled energy on moment use small data sets or do not offer a statistical analysis sufficient to gauge the significance of their results. Furthermore, selection bias can introduce artificial trends in stress drop or energy with moment [*Ide and Beroza*, 2001; *Oth et al.,* 2010].

We show that both apparent stress and stress drop are log-normally distributed, and identify several enervated and energetic earthquakes. These anomalous earthquakes represent statistically significant differences in energy, apparent stress and stress drop. While the majority of our events follow a constant apparent stress, the anomalous events are outside of these ranges and are not predictable simply given their moment. Further understanding of these events will be important to completely quantify their associated hazard.

Acknowledgements

Thanks to R. Tajima and T. Hanks for helpful discussion; B. Goertz-Allman and A. McGarr for edits and comments; and JMA and NIED for use of HiNet and Kik-Net data. This research was supported by the SCEC Extreme Ground Motion project; SCEC number 1462. A. Baltay is grateful to the Japan Society for the Promotion of Science and the NSF for the opportunity to work at the University of Tokyo in summer 2009. A. Baltay is supported by a Gabilan Stanford Graduate Fellowship.

References

Abercrombie, R. E. (1995), Earthquake source scaling relationships from −1 to 5 ML using seismograms recorded at 2.5-km depth, *J. Geophys. Res.*, *100*(B12), 24015.

Aki, K. (1972), Scaling law of earthquake source time-function, *Geophys. J. Royal Astron. Soc.*, *31*(1-3), 3–25.

Allmann, B. P., and P. M. Shearer (2009), Global variations of stress drop for moderate to large earthquakes, *J. Geophys. Res.*, *114*(B1).

Baltay, A., G. Prieto, and G. C. Beroza (2010), Radiated seismic energy from coda measurements and no scaling in apparent stress with seismic moment, *J. Geophys. Res.*, *115*(B8), 1-12.

Boatwright, J. (1980), A spectral theory for circular seismic sources; simple estimated of source dimension, dynamic stress drop, and radiated seismic energy, *Bull. Seismol. Soc. Am.*, *70*(1).

Boatwright, J., and G. L. Choy (1986), Teleseismic Estimates of the Energy Radiated by Shallow Earthquakes, *J. Geophys. Res.*, *91*(B2), 2095-2112.

Boore, D., and J. Boatwright (1984), Average body-wave radiation coefficients, *Bull. Seismol. Soc. Am.*, *74*(5), 1615-1621.

Brune, J. N. (1970), Tectonic Stress and the Spectra of Seismic Shear Waves from Earthquakes, *J. Geophys. Res.*, *75*(26).

Eshelby, J. D. (1957), The Determination of the Elastic Field of an Ellipsoidal Inclusion, and Related Problems, *Proc. R. Soc. London, Ser. A, 241*(1226), 376-396.

Hanks, T. C. (1977), Earthquake stress drops, ambient tectonic stresses and stresses that drive plate motions, in *Pure and Applied Geophysics*, vol. 115, pp. 441-458-458, Birkhäuser Basel.

Hikima, K., and K. Koketsu (2005), Rupture processes of the 2004 Chuetsu (mid-Niigata prefecture) earthquake, Japan: A series of events in a complex fault system, *Geophys. Res. Lett.*, *32*(18), L18303.

Ide, S., and G. C. Beroza (2001), Does apparent stress vary with earthquake size?, *Geophys. Res. Lett.*, *28*(17), 3349.

Ide, S., G. C. Beroza, S. G. Prejean, and W. L. Ellsworth (2003), Apparent break in earthquake scaling due to path and site effects on deep borehole recordings, *J. Geophys. Res.*, *108*(B5).

Izutani, Y. (2005), Radiated energy from the mid Niigata, Japan, earthquake of October 23, 2004, and its aftershocks, *Geophys. Res. Lett.*, *32*(21).

Kawasaki, S., S. Matsuksai and Y. Fukushima (2008), A relation between Mjma and seismic moment (determined from a dense broad ad seismograph network) for shallow crustal events in Japan, *Eos Trans.* AGU *90*(52), Fall Meet. Suppl., Abstract S13C-1827.

Miyake, H., K. Koketsu, K. Hikima, M. Shinohara, and T. Kanazawa (2010), Source Fault of the 2007 Chuetsu-oki, Japan, Earthquake, *Bull. Seismol. Soc. Am.*, *100*(1), 384-391.

Oth, A., D. Bindi, S. Parolai, and D. Di Giacomo (2010), Earthquake scaling characteristics and the scale-(in)dependence of seismic energy-to-moment ratio: Insights from KiK-net data in Japan, Geophys. Res. Lett., 37, L19304.

Perez-Campos, X. (2003), Reconciling Teleseismic and Regional Estimates of Seismic Energy, *Bull. Seismol. Soc. Am.*, *93*(5), 2123-2130.

Prieto, G. A., D. Thomson, F. Vernon, P. Shearer, and R. Parker (2007), Confidence intervals for earthquake source parameters, *Geophys. J. Int*, *168*(3), 1227–1234.

Singh, S. K., and M. Ordaz (1994), Seismic Energy Release in Mexican Subduction Zone Earthquakes, *Bull. Seismol. Soc. Am.*, *84*(5), 1533-1550.

Sonley, E., and R. E. Abercrombie (2006), Effects of Methods of Attenuation Correction on Source Parameter Determination, in *Earthquakes: Radiated Energy and the Physics of Faulting, Geophys. Monogr. Ser., vol. 170,*, edited by R. Abercrombie et. al., pp. 91 - 97, AGU, Washington, DC.

Uchida, N., T. Matsuzawa, K. Shimamura, A. Hasegawa and W. L. Ellsworth (2010), Seismicity on and interplate asperity off-Kamaishi, NE Japan over two earthquake cycles, abstract S34B-04, 2010 Fall Meeting, AGU.

Walter, W., K. Mayeda, and R. Gok, A (2006), The Scaling of Seismic Energy With Moment: Simple Models Compared With Observations, in *Earthquakes: Radiated Energy and the Physics of Faulting, Geophys. Monogr. Ser., vol. 170,*, edited by R. E. Abercrombie, et al., pp. 25 - 41, AGU, Washington, DC.

Wyss, M., and J. N. Brune (1968), Seismic moment, stress, and source dimensions for earthquakes in the California-Nevada region, *J. Geophys. Res.*, *73*(14), 4681–4694.

Yamada, M., J. Mori, and T. Heaton (2009), The slapdown phase in High-acceleration records of large earthquakes, *Seismol. Res. Lett.*, *80*(4), 559-564.

Appendix 1: Data tables of events studied.

Table 3.1 Chuetsu 2004

Catalog Information							Determined Parameters											
No.	Date	Time	Lat.	Long.	Depth	JMA Mag	M_o (Nm)	M_w	E_R (J)	E_R/M_o x10^{-5}	τ_a	SDE	f_c	1σ conf.	σΔ (MPa)	1σ conf.	# S
1	10/23/04	56:00.3	37.29	138.87	13.1	6.8	7.59E+18	6.55	2.95E+14	3.89	1.419	0.068	0.226	0.203	12.28	0.073	18
2	10/23/04	34:05.7	37.31	138.93	14.2	6.5	2.88E+18	6.27	9.77E+13	3.39	1.238	0.093	0.484	0.278	21.09	0.065	18
3	10/23/04	03:12.7	37.35	138.98	9.4	6.3	7.94E+17	5.9	2.57E+13	3.31	1.192	0.064	0.477	0.191	10.38	0.089	18
4	10/27/04	40:50.2	37.29	139.03	11.6	6.1	6.92E+17	5.86	2.69E+13	3.89	1.417	0.072	0.672	0.217	17.5	0.057	16
5	10/23/04	11:56.8	37.25	138.83	11.5	6	4.27E+17	5.72	1.02E+13	2.40	0.88	0.072	0.614	0.215	9.26	0.094	16
6	10/25/04	04:57.6	37.33	138.95	15.2	5.8	2.14E+17	5.52	8.91E+12	4.17	1.504	0.083	1.022	0.249	17.42	0.083	18
7	10/23/04	07:30.9	37.35	138.87	14.9	5.7	1.48E+17	5.41	1.86E+12	1.26	0.459	0.099	0.756	0.296	5	0.081	16
8	10/23/04	45:57.2	37.3	138.88	12.3	5.7	1.58E+17	5.43	3.63E+12	2.29	0.839	0.075	0.833	0.225	8.24	0.074	17
9	10/23/04	57:26.3	37.21	138.86	7.5	5.3	5.37E+16	5.12	8.13E+11	1.55	0.558	0.083	1.097	0.249	6.18	0.083	17
10	10/23/04	36:45.0	37.22	138.82	11	5.3	5.62E+16	5.13	6.92E+11	1.23	0.451	0.041	0.656	0.124	2.12	0.12	10
11	10/23/04	34:45.7	37.32	138.91	19.9	5.3	2.63E+16	4.91	1.74E+12	6.61	2.382	0.029	1.516	0.088	13.04	0.077	17
12	10/25/04	28:08.9	37.2	138.87	10.1	5.3	5.37E+16	5.12	1.10E+12	2.09	0.75	0.057	1.08	0.171	7.34	0.085	17
13	10/24/04	00:30.0	37.18	138.95	14	5.1	3.02E+16	4.95	1.07E+11	0.355	0.129	0.118	0.24	0.355	0.13	0.07	16
14	11/6/04	53:21.4	37.36	139	0.2	5.1	2.88E+16	4.94	3.16E+11	1.10	0.401	0.085	1.001	0.254	3.21	0.08	17
15	11/8/04	32:17.3	37.39	139.05	5.8	5.1	1.91E+16	4.82	5.50E+11	2.88	1.037	0.068	1.706	0.204	9.47	0.101	17
16	11/1/04	35:49.1	37.21	138.9	8.5	5	1.15E+16	4.67	4.47E+11	3.80	1.395	0.055	1.613	0.164	6.66	0.053	18
17	11/9/04	15:59.7	37.35	139	10	5	1.12E+16	4.67	1.86E+11	1.70	0.609	0.059	1.4	0.178	3.87	0.06	18
18	10/24/04	21:34.0	37.24	138.83	11.5	5	1.29E+16	4.71	1.55E+11	1.20	0.437	0.092	0.701	0.277	1.09	0.058	18
19	10/24/04	28:04.0	37.22	138.89	12.2	4.8	5.25E+15	4.45	3.02E+11	5.75	2.078	0.04	2.468	0.121	11.06	0.049	17
20	11/15/04	39:33.4	37.38	139	0.4	4.7	8.71E+15	4.59	3.89E+10	0.447	0.161	0.113	0.789	0.338	0.67	0.062	18

21	11/6/04	16:50.0	37.37	139	1.2	4.5	1.55E+15	4.09	3.24E+10	2.09	0.763	0.055	2.869	0.166	4.73	0.058	18
22	11/12/04	24:00.2	37.24	138.93	9.8	4.3	5.75E+14	3.81	4.07E+10	7.08	2.562	0.034	5.224	0.101	13.44	0.04	17
23	11/1/04	58:20.3	37.39	139	10	3.8	2.57E+14	3.57	7.41E+09	2.82	1.028	0.022	5.006	0.066	5.39	0.037	18
24	10/27/04	30:02.6	37.23	138.84	11.9	3.8	3.80E+14	3.69	7.24E+09	1.91	0.694	0.028	3.485	0.085	2.77	0.074	18
25	10/27/04	35:40.3	37.22	138.92	8.2	3.7	1.95E+14	3.49	6.03E+09	3.09	1.131	0.042	4.983	0.127	3.95	0.047	18
26	12/17/04	48:38.5	37.33	138.99	2	3.6	3.47E+14	3.66	2.88E+09	0.832	0.305	0.095	2.187	0.286	0.91	0.06	18
27	11/8/04	52:48.6	37.39	139.06	18.9	3.6	9.12E+13	3.27	4.79E+09	5.25	1.918	0.035	7.772	0.106	8.32	0.039	18
28	10/28/04	29:14.3	37.19	138.89	8.5	3.6	9.77E+13	3.29	5.25E+09	5.37	1.955	0.035	7.546	0.106	6.98	0.031	18
29	10/28/04	52:08.2	37.34	138.95	4.3	3.5	8.91E+13	3.27	3.72E+09	4.17	1.512	0.04	8.43	0.121	6.91	0.037	18
30	11/5/04	53:36.7	37.44	138.94	19.3	3.1	2.57E+13	2.91	1.35E+09	5.25	1.915	0.048	11.18	0.143	7.62	0.065	17
31	11/8/04	45:03.2	37.38	139.04	1	3.1	2.88E+13	2.94	1.07E+09	3.63	1.324	0.054	8.739	0.161	4.67	0.042	18
32	10/30/04	48:50.2	37.38	139.02	10	2.9	2.75E+13	2.93	5.62E+08	2.09	0.752	1.50 E-10	8.687	4.60 E-10	3.53	0.037	18

Table 3.2 Chuetsu-Oki 2007

Catalog Information							Determined Parameters										
No.	Date	Time	Lat.	Long.	Depth	JMA Mag	M_o (Nm)	M_w	E_R (J)	E_R/M_o x10^{-5}	τ_a	SDE	f_c	1σ conf.	σΔ (MPa)	1σ conf.	# S
1	7/16/07	13:22.6	37.56	138.61	16.8	6.8	1.41E+19	6.73	2.00E+15	14.10	5.095	0.028	0.201	0.085	22.25	0.034	17
2	7/16/07	37:40.4	37.5	138.64	22.5	5.8	3.80E+17	5.69	6.31E+13	16.60	6.017	0.065	0.859	0.194	36.83	0.046	13
3	7/16/07	18:38.0	37.5	138.55	18	4.9	2.14E+16	4.85	6.61E+11	3.02	1.108	0.081	1.382	0.243	6.82	0.051	17
4	7/16/07	16:16.0	37.53	138.64	14	4.6	1.15E+17	5.34	2.34E+12	2.04	0.736	0.187	0.636	0.561	3.42	0.031	14
5	7/16/07	19:46.1	37.37	138.54	21.5	4.4	1.05E+16	4.64	2.63E+10	0.25	0.091	0.106	0.31	0.318	0.11	0.168	17
6	7/16/07	18:05.7	37.41	138.45	16.6	4.4	6.03E+16	5.15	8.51E+11	1.45	0.52	0.146	0.977	0.439	4.62	0.089	10
7	7/16/07	34:28.9	37.53	138.56	18.9	4.3	8.13E+15	4.57	2.34E+11	2.88	1.036	0.062	2.052	0.187	6.95	0.077	17
8	7/16/07	52:14.6	37.5	138.6	16.8	4.2	1.05E+15	3.98	2.95E+10	2.82	1.023	0.054	3.754	0.162	6.65	0.082	17
9	7/20/07	52:05.4	37.45	138.56	19.4	4.2	1.00E+15	3.97	4.90E+10	5.01	1.806	0.037	3.676	0.112	8.35	0.053	17
10	7/16/07	17:17.8	37.4	138.51	19.6	4	1.00E+16	4.63	1.07E+11	1.07	0.392	0.194	2.029	0.581	7.09	0.08	13

11	7/18/07	47:54.9	37.48	138.57	18	3.7	4.47E+14	3.73	2.88E+10	6.61	2.382	0.041	5.106	0.123	10.95	0.081	17
12	7/17/07	35:59.5	37.52	138.54	17.8	3.6	5.50E+14	3.79	1.38E+10	2.51	0.918	0.061	3.849	0.184	4.74	0.064	14
13	7/20/07	54:43.0	37.45	138.57	19.5	3.6	2.75E+14	3.59	1.86E+10	6.92	2.494	0.071	5.485	0.213	9.24	0.051	15
14	7/16/07	49:03.5	37.52	138.71	26.4	2.8	5.50E+13	3.13	3.63E+09	6.46	2.361	3.00 E-11	9.747	8.90 E-11	9.54	0.033	17

Table 3.3 Iwate-Miyagi 2008

Catalog Information							Determined Parameters										
No.	Date	Time	Lat.	Long.	Depth	JMA Mag	M_o (Nm)	M_w	E_R (J)	E_R/M_o x10^{-5}	τ_a	SDE	f_c	1σ conf.	σΔ (MPa)	1σ conf.	# S
1	6/14/08	43:45.4	39.03	140.88	7.8	7.2	2.69E+19	6.92	1.86E+15	6.76	2.475	0.074	0.13	0.221	10.54	0.088	17
2	6/14/08	20:11.9	38.88	140.68	6.4	5.7	3.09E+17	5.62	3.63E+12	1.20	0.434	0.071	0.426	0.212	2.69	0.139	13
3	6/16/08	14:38.4	39	140.84	10.8	5.3	9.55E+16	5.29	2.00E+12	2.04	0.745	0.072	1.018	0.215	8.25	0.095	17
4	6/14/08	27:32.8	39.14	140.94	10.8	5.2	5.62E+16	5.13	9.33E+11	1.66	0.599	0.033	0.731	0.1	3.35	0.065	11
5	6/14/08	07:20.8	39.12	140.89	11.3	4.8	2.45E+16	4.89	1.20E+11	0.49	0.177	0.046	0.755	0.137	1.31	0.096	17
6	6/14/08	39:59.0	38.93	140.89	6.3	4.8	9.55E+15	4.62	3.02E+11	3.24	1.166	0.043	1.489	0.129	5.45	0.095	11
7	6/14/08	42:32.4	39	140.89	10	4.8	1.48E+16	4.74	4.07E+11	2.75	1.009	0.036	1.356	0.109	5.38	0.096	14
8	6/14/08	52:42.3	39.09	140.91	12.9	4.6	1.35E+16	4.72	3.16E+11	2.34	0.85	0.056	1.759	0.168	6.36	0.071	11
9	6/17/08	05:03.3	39.14	140.94	11	4.6	4.37E+15	4.39	7.76E+10	1.78	0.648	0.025	1.883	0.074	3.39	0.267	17
10	6/26/08	51:11.1	39.08	140.97	6.9	4.6	7.24E+15	4.54	1.55E+11	2.14	0.776	0.067	0.789	0.2	1.16	0.112	14
11	6/14/08	49:05.7	39.11	140.94	11.5	4.5	3.98E+16	5.04	3.55E+11	0.89	0.324	0.106	1.317	0.319	4.23	0.104	13
12	6/14/08	00:16.0	39.03	140.91	12	4.5	4.90E+15	4.43	2.75E+11	5.62	2.041	0.035	2.302	0.104	9.49	0.067	17
13	6/14/08	39:06.5	39.12	140.93	11.3	4.5	5.75E+15	4.47	3.09E+11	5.50	1.974	0.02	2.227	0.06	7.9	0.084	17
14	6/18/08	55:01.1	39.04	140.86	12.3	4.5	2.00E+15	4.17	1.23E+11	6.17	2.227	0.035	2.748	0.106	7.56	0.099	17
15	6/18/08	04:33.5	39.1	140.93	11.5	4.5	4.90E+15	4.43	1.51E+11	3.09	1.111	0.028	2.018	0.083	5.05	0.075	17
16	6/14/08	35:16.9	39.02	140.89	9.6	4.3	2.63E+15	4.24	1.05E+11	3.98	1.452	0.017	2.208	0.052	8.57	0.087	17
17	6/14/08	11:56.4	38.87	140.86	8.9	4.1	8.32E+14	3.91	2.09E+10	2.45	0.901	0.043	2.85	0.129	3.5	0.071	14
18	6/17/08	30:57.9	39.11	140.94	11	4.1	8.32E+14	3.92	3.47E+10	4.07	1.484	0.04	3.471	0.121	6.34	0.074	17

19	6/14/08	13:55.9	39.04	140.89	12.1	3.7	1.66E+14	3.45	1.00E+10	6.17	2.212	0.019	6.402	0.057	9.23	0.081	17
20	6/14/08	42:22.0	39.04	140.87	9.4	3.5	2.00E+14	3.5	7.08E+09	3.55	1.284	0.038	5.683	0.114	6.63	0.075	17
21	6/26/08	20:02.2	39.04	140.89	10.9	3.5	2.63E+14	3.58	7.41E+09	2.82	1.033	0.027	4.503	0.082	4.56	0.054	10
22	6/15/08	14:34.6	39.01	140.89	10.1	3.4	8.32E+13	3.24	2.34E+09	2.82	1.031	0.042	6.143	0.125	3.97	0.043	17
23	6/18/08	55:44.1	39.04	140.89	10.4	3.3	2.75E+14	3.59	3.72E+09	1.35	0.49	0.064	4.06	0.193	2.67	0.058	13
24	6/15/08	56:37.8	39.03	140.89	10.7	3.1	4.90E+13	3.09	1.91E+09	3.89	1.398	0.018	9.119	0.054	6.01	0.031	17
25	6/14/08	13:33.1	39.05	140.88	10.4	2.9	5.01E+13	3.1	6.31E+08	1.29	0.464	0.058	6.425	0.175	2.24	0.051	14
26	6/15/08	06:36.6	39.04	140.87	11.7	2.9	4.47E+13	3.06	7.94E+08	1.78	0.644	0.041	7.121	0.124	2.96	0.062	15
27	7/3/08	59:32.2	39.04	140.9	11	2.8	2.69E+13	2.92	6.76E+08	2.57	0.924	1.80 E-11	9.747	5.30 E-11	4.6	0.035	17

Table 3.1 Kamaishi repeating sequence

Catalog Information							Determined Parameters										
No.	Date	Time	Lat.	Long.	Depth	JMA Mag	M_o (Nm)	M_w	E_R (J)	E_R/M_o x10^{-5}	τ_a	SDE	f_c	1σ conf.	$\sigma\Delta$ (MPa)	1σ conf.	# S
1	1/11/08	00:31.8	39.34	142.07	47.1	4.7	1.04E+16	4.64	1.57E+12	15.10	8.21	0.023	3.065	0.068	28.72	0.069	17
2	7/9/05	00:27.3	39.34	142.06	47.4	3.6	3.94E+14	3.7	2.67E+10	6.79	3.68	0.027	5.837	0.081	7.27	0.095	17
3	7/18/04	22:01.9	39.34	142.06	47.7	3.1	5.77E+13	3.14	9.04E+08	1.57	0.85	0.072	8.705	0.217	3.13	0.083	17
4	6/20/03	47:26.8	39.34	142.06	47.5	3	3.09E+13	2.96	2.30E+09	7.42	4.023	0.018	14.778	0.054	9.15	0.1	13
5	8/30/04	51:48.8	39.34	142.07	47.5	2.8	1.63E+13	2.77	4.57E+08	2.81	1.526	0.019	16.534	0.056	6.41	0.082	17
6	1/15/07	54:01.6	39.34	142.06	47.4	2.8	3.89E+13	3.03	1.98E+09	5.11	2.771	0.018	13.571	0.055	8.72	0.085	17
7	1/5/06	12:17.1	39.34	142.07	46.8	2.7	1.74E+13	2.79	1.88E+09	10.80	5.847	0.015	26.058	0.044	31.14	0.069	14
8	10/20/03	17:57.6	39.34	142.08	47.1	2.6	9.66E+12	2.62	1.11E+09	11.50	6.226	0.014	25.731	0.041	15.97	0.103	10
9	8/27/04	12:34.9	39.34	142.07	47.5	2.6	8.77E+12	2.6	4.47E+08	5.10	2.766	0.012	24.416	0.036	12	0.093	17
10	2/25/07	24:55.4	39.34	142.07	46.7	2.5	1.26E+13	2.7	9.51E+08	7.54	4.09	0.013	24.184	0.039	17.17	0.073	17
11	6/3/05	09:39.3	39.34	142.07	46.8	2.4	7.66E+12	2.56	3.84E+08	5.01	2.715	0.015	25.058	0.044	11.62	0.085	17
12	10/18/06	01:46.5	39.34	142.07	47.1	2.2	6.15E+12	2.49	4.31E+08	7.02	3.803	0.014	28.171	0.041	13.24	0.091	13
13	8/30/04	40:05.9	39.34	142.07	47.4	2.1	3.52E+12	2.33	4.84E+07	1.38	0.746	0.008	20.854	0.025	3.05	0.088	17

14	9/11/05	35:52.0	39.34	142.07	46.6	1.9	2.85E+12	2.27	1.45E+08	5.08	2.754	0.023	40.603	0.069	20.88	0.068	15
15	11/2/03	44:08.7	39.37	142.1	65.1	1.8	1.55E+12	2.1	4.19E+07	2.69	1.457	1.80 E-07	30.823	5.40 E-07	4.73	0.093	17

1. No. Event number
2. Date Date of event origin, YEAR-MM-DD
3. Time Time of event origin, HH:MM:SS.s
4. Lat. Latitude of event
5. Long. Longitude of event
6. Depth Event depth
7. JMA_mag Magnitude from the JMA catalog used
8. M_o (Nm) Moment as determined from eGf deconvolution, in N-m
9. M_w Mw corresponding to above moment: Mw = (log10(Mo)-9.05)/1.5
10. E_R (J) Radiated Energy, Joules, averaged from all stations
11. E_R/M_o Scaled Energy, averaged from all stations
12. τ_a (MPa) Apparent Stress=mu*E_R/M_o, MPa, w/ mu below, averaged from all stations
13. SDE (log10) Standard Error of Mean of Apparent Stress
14. f_c Corner Frequency from stacked source spectra, in Hz
15. 1σ conf 1-sigma Confidence interval from corner frequency residual fit, log10 units, +/-error bars
16. σΔ (MPa) Brune Stress Drop, MPa, from moment and corner frequency
17. 1σ conf 1-sigma Confidence interval from fc fit, propagated to Stress Drop, log10 units
18. # S Number of stations used for that event

Notes:
12. mu = rho*beta^2 For Chuetsu 2004, Chuetsu-Oki 2007 and Iwate-Miyagi, rho=2800; beta=3600; mu= 3.63e+10 Pa; For Kamaishi, beta=4400 (deeper

CHAPTER 4

RMS Stress Drop and Stress Drop Variability

Abstract

We estimate the a_{RMS} -stress drop [*Hanks*, 1979] using acceleration time records for 59 earthquakes from two earthquake sequences in eastern Honshu, Japan. These acceleration-based stress drops compare well to Brune stress drops calculated for the same events by *Baltay et al.* [2011] using an empirical Green's function based approach. This consistency supports the assumption earthquake acceleration time histories above the corner frequency can be considered white, Gaussian, noise. Although the a_{RMS}-stress drop is computationally simpler than the eGf method, and is used as the "stress parameter" to describe earthquake source in ground motion prediction equations, we find that it is only valid at source-station distances of ~20 km or less because it does not account for attenuation or scattering. The correlation between eGf-based Brune stress drop and a_{RMS}-stress drop is strong. Events with anomalously high and low stress drops obtained through the eGf method have similarly high and low a_{RMS}-stress drops. We find that the inter-event standard deviation of stress drop is similar for both methods, provided we apply the distance restriction on a_{RMS}-stress drop. This observation indicates that the observed variability is inherent to source variability, rather than uncertainties in stress drop estimates.

The material in this chapter is in preparation for publication in the *Bulletin of the Seismological Society of America* with co-authors G.C. Beroza and T.C. Hanks.

4.1 Introduction

Stress drop describes the difference between the initial and final stress of an earthquake rupture, and is a critical parameter both for describing earthquake source physics and for strong ground motion prediction. Because stress drop can be measured in the laboratory as well as from earthquakes, it can be related to other source parameters to understand faulting dynamics. Quantifying the relationship between earthquake moment and stress drop, and characterizing stress drop variability, is essential for ground motion prediction equations; however, because estimates of stress drop can be subject to large uncertainties, the relationship between moment and stress drop and the true intrinsic variability of stress drop remains uncertain.

Many sources of uncertainty exist in stress drop estimates. Different methods may yield difference results because they make different assumptions about source behavior, such as rupture velocity or the shape of the rupture area. The Brune model, for one, assumes instantaneous rupture, and hence the source dimension, $r \sim 12.81\beta/f_c$, while the dynamic Madariaga rupture model assumes $r \sim 2.4\beta/f_c$ [e.g.. *Venkataraman et al.* 2006; *Sonly and Abercrombie*, 2006]. The inherent difficulty in correcting for propagation effects in earthquake recordings and the need to consider a wide range of frequencies due to the broadband nature of earthquakes can also lead to uncertain stress drop estimates [e.g. *Ide and Beroza,* 2001, *Ide et al.* 2003]. Moreover, typical formulations for stress drop depend on the cube of the measure of source finiteness, whether corner frequency or source duration, such that modest uncertainties in the underlying measurement are greatly magnified in stress drop estimates.

Understanding the distribution of earthquake stress drops can illuminate other source parameter relationships to help constrain the mechanics of earthquakes; to resolve whether small and large earthquakes follow the same physical constraints; and to further quantify stress drop as an earthquake source term in engineering ground motion prediction equations [e.g. *Beeler*, 2006; *Kanamori and Anderson*, 1975; *Boore and Joyner*, 1989].

Hanks [1979] related the root-mean-square (RMS) value of acceleration time histories to earthquake stress drop. The traditional Brune stress drop is dependent on earthquake moment and corner frequency. It is usually modeled from a spectrum, and thus is influenced by the low and intermediate frequencies, close to the corner frequency. The a_{RMS}-stress drop developed by *Hanks* [1979] measures an inherently different part of the spectrum, from the corner frequency, f_c to the high frequency limit of the records, f_{max}. a_{RMS}-stress drop is dependent only on $\sqrt{f_c}$, while the Brune stress drop is proportional to f_c^3. For this reason, the a_{RMS}-stress drop measurements are much less susceptible to noise or errors in corner frequency, for any single event, than Brune stress drop.

McGuire and Hanks [1980] and *Hanks and McGuire* [1981] demonstrated that stress drops were independent of magnitude for California earthquakes based on a_{RMS} measurements and that it provided an improvement over traditional stress drop measurements in reducing variability. They also demonstrated that acceleration time histories can be modeled as band-limited white Gaussian noise and that peak acceleration (PGA or a_{max}) is predictable given a stress drop and corner frequency. Finally, these studies supported self-similar earthquake behavior and the use of a Brune ω^{-2} model for acceleration spectra, with no systematic variation of earthquake stress drop with earthquake magnitude.

The a_{RMS} relationships measure acceleration between the corner frequency and f_{max}, which is the frequency band of greatest interest to earthquake engineering and seismic hazard assessment. This work was some of the first to discuss duration-based acceleration metrics for seismic building design, and was quickly adopted by the seismic hazard community. a_{rms}-stress drop is currently used to describe the earthquake source in many ground motion prediction equations, where it is often referred to as the "stress parameter" [*Boore*, 1983]. However, since the original formulation of a_{rms}-stress drop, not much research on the topic has occurred

Revisiting the a_{RMS} based stress drop is of interest for several reasons. At the time of the original study, Brune stress drops were often estimated using crude corrections for attenuation or path effects, if any at all. Because source measurement variability is often

driven by corner frequency uncertainty, the a_{RMS} approach yielded much less variability. In our recent work, we use a robust eGf technique to remove path effects from stress drop estimates. By comparing the a_{RMS}-stress drop to the eGf-based stress drop we can better assess the viability of both methods and the uncertainties associated with each. Second, a_{RMS} is very simple to measure, and is only slightly dependent on the corner frequency, which may be known or roughly estimated. For that reason, each record can be analyzed independently, without waiting for aftershocks (eGf events) to occur, and could be used in areas without dense aftershock sequences, where eGf assumptions will not apply. The algorithm for a_{RMS}-stress drop is computationally less intensive, with fewer assumptions, and has potential to be developed for use in real time. In fact, RMS-acceleration is one of the most simple measurements that can be made on a single recording. Finally, a_{RMS}-stress drop, or "stress parameter", is used to describe the earthquake source in many ground motion prediction equations [*Boore,* 1983]. Empirically, the stress parameter is used as guide for magnitude scaling of ground motion [*Chiou and Youngs*, 2008]; it is also used as an input for simulated ground motions, especially in data-poor regions [*Peterson et al.,* 2008]. Understanding the relationship, and variability, of the a_{RMS} stress drop and other stress drop measurements is essential ground motion prediction efforts.

In this study, we test the relationships developed by *Hanks* [1979] using a recent, well-recorded, much larger data set of 59 earthquakes, spanning a large range of magnitudes and source-site distances. We measure the RMS-acceleration of two mainshock-aftershock sequences from KikNet accelerograms in eastern Honshu, Japan, which have been previously studied by *Baltay et al.* [2011], and compare these a_{RMS}-stress drops to eGf-based Brune stress drops.

We find that stress drop can precisely be computed from a_{RMS} measurements, which supports the analyses performed by *Hanks* [1979], *McGuire and Hanks* [1980] and *Hanks and McGuire* [1981]. While the algorithm behind the a_{RMS} method is computationally simple, the a_{RMS} approach for stress drop does not consider frequency dependent anelastic attenuation or other path and site effects, and suffers from loss of signal at farther stations. For small events, stress drop is underestimated at stations farther than ~20 km; however at closer stations, a_{RMS}-stress drop compares well to the eGf-stress drop.

Although earlier studies find that the a_{RMS} approach for stress drop was much less variable, our eGf-based stress drop estimates show a variability comparable to a_{RMS}-stress drop, and overall distribution of event stress drops is similar between methods, implying that the eGf method is an improvement over methods that do not consider path corrections. When considering corner frequency as the only source of uncertainty, the a_{RMS} stress drop for any single earthquake is smaller than that of the eGf method; however, there are other sources of uncertainty inherent in stress drop estimates.

We also estimate a_{max} (PGA) from a_{RMS} and compare the data to the theoretical PGA using the previously established relationships together with an input stress drop distribution from *Baltay et al.* [2011]. We find that PGA is predictable from a_{RMS}, and that data match the theoretical relations at close distances and for the larger earthquakes, for which attenuation is negligible. The ability to predict PGA given only an *a priori* stress drop distribution and knowledge of the source duration strongly supports the conjecture that acceleration time histories can be treated as Gaussian white noise above the corner frequency.

While we find the a_{RMS} method to be valid for estimating stress drops at close source-station distances ($R \leq 20$ km), the eGf method is more capable of using data from stations at greater distances. The computational simplicity of the a_{RMS} -stress drop method retains its appeal for some applications, such as real time source assessment, source parameter determination in data-sparse situations, and for use in engineering ground motion equations. Finally, our larger data set allows us to quantify the variability of stress drop. We find that measured variability is similar for the two approaches, which supports the notion that it is a result of intrinsic source variability, rather than measurement error.

4.2 Empirical Green's Function Stress Drops

Baltay et al. [2011] used an empirical Green's function (eGf) coda-based method to determine source parameters, including stress drop, for three crustal earthquake sequences in Honshu, Japan. They modeled source spectra stacked from recordings at many stations using a Brune ω^{-2} [*Brune*, 1970] spectrum to fit a corner frequency. The

Brune stress drop was estimated from the corner frequency as in *Baltay et al.* [2011], using β=3600 m/*s*,

$$\Delta\sigma = \frac{7M_o}{16}\left(\frac{2\pi f_c}{2.34\beta}\right)^3 . \quad (1)$$

The sequences analyzed by *Baltay et al.* [2011] include the 2008 M_w *6.9* Iwate-Miyagi Nairiku mainshock and 26 aftershocks, and the 2004 M_w *6.6* Chuetsu (mid-Niigata) earthquake and 31 aftershocks. The other two sequences studied by *Baltay et al.* [2011], Chuetsu-Oki 2007 and the off-Kamaishi repeating events, are not considered here as they are both off shore, and hence the source-station distances are too large to be of interest in the a_{RMS} method. For each earthquake, the source spectra were determined from a stack of the spectra at each station where HiNet broadband velocity data were available. In aggregate for all 59 events, stress drop follows a log-normal distribution with a mean of 5.0 MPa and $\log_{10}$ standard deviation of 0.4 (Figure 4.4 and Table S1 of *Baltay et al.* 2011).

4.3 RMS Stress Drop

The ω^{-2} model [*Aki,* 1967; *Brune,* 1970] for earthquake acceleration spectra is flat for frequencies $f>>f_c$, which is consistent with white noise if the phase can be considered random. *Hanks and McGuire* [1981] assumed that the phase of acceleration spectra are random white noise, consistent with a far-field ω^{-2} model, for the finite duration of the *S*-wave arrival window, from $t=0$ (*S*-wave arrival) to $t=T_d$, the duration of faulting. They noted, however, that there is an observational limit at some frequency, f_{max}, above which the spectrum decays rapidly. f_{max} was later explored by *Hanks* [1982], who concluded it was a property of local site or instrument conditions. *Hanks and McGuire* [1981] demonstrated that acceleration time histories were Gaussian in the finite duration window, positing that high-frequency acceleration is finite-duration, band-limited, white Gaussian noise, an assumption that has been central to ground motion prediction since. They also showed that the relationship between a_{RMS} and a_{max} was predictable using random vibration theory, providing a stringent test on the white Gaussian assumption. For

our study, f_{max} is important because it places an upper frequency limit at which acceleration can be considered to be white noise.

The root-mean-square value of acceleration time history can be related to stress drop (Eq. 1), corner frequency and f_{max}. Parseval's Theorem states that the Fourier transform is unitary, i.e.:

$$\int_{-\infty}^{\infty} |a(t)|^2 dt = \frac{1}{2\pi} \int_{-\infty}^{\infty} |\tilde{a}(\omega)|^2 d\omega \tag{2}$$

Assuming significant motion is recorded at close stations only for the duration of faulting, and that the signal is band-limited from f_c to f_{max}, we rewrite (2) as

$$\int_0^{T_d} |a(t)|^2 dt = \frac{2}{2\pi} \int_{2\pi f_c}^{2\pi f_{\max}} |\tilde{a}(\omega)|^2 d\omega \tag{3}$$

For spectra following a *Brune* [1970] model,

$$\tilde{a}(\omega) = \frac{\Omega_o \omega^2}{1 + (\omega/\omega_c)^2} \tag{4}$$

For $f_o \le f \le f_{max}$ (and hence $\omega_o \le \omega \le \omega_{max}$)

$$\tilde{a}(\omega) = \Omega_o \omega_c{}^2 = \Omega_o (2\pi f_c)^2 \tag{5}$$

The root-mean-square of acceleration, a_{RMS}, over the interval $[0, T_d]$ is defined as

$$a_{RMS} = \sqrt{\frac{1}{T_d} \int_0^{T_d} |a(t)|^2 dt} \tag{6}$$

Combining (4) – (6), with $f_{max} >> f_c$, so that $f_{max} - f_c \approx f_{max}$

$$a_{RMS} = \sqrt{\frac{1}{T_d} \frac{2}{2\pi} \int_{2\pi f_c}^{2\pi f_{\max}} |\tilde{a}(\omega)|^2 d\omega} = \sqrt{f_c \frac{1}{\pi} \left|\Omega_o (2\pi f_c)^2\right|^2 (2\pi f_{\max} - 2\pi f_c)} = \sqrt{2} (2\pi)^2 \Omega_o f_c{}^3 \sqrt{\frac{f_{\max}}{f_c}} \tag{7}$$

For the Brune ω^{-2} model, (e.g., *Hanks and Thatcher*, 1972), where $M_o = 4\pi\rho\beta^3 R\Omega_o$ (after *Keilis-Borok*, 1957)

$$\Delta\sigma = 106\rho R\Omega_o f_c^{\ 3} \tag{8}$$

$$a_{RMS} = 2R_{\theta\phi}(2\pi)^2 \frac{\Delta\sigma}{106\rho R}\sqrt{\frac{f_{\max}}{f_c}} \tag{9}$$

where the factor of $1/\sqrt{2}$ accounts for partitioning of ground motion primarily onto two horizontal components; the factor of *2* accounts for free surface amplification; $R_{\theta\phi}$=0.6 is the *rms* value of shear-wave radiation pattern; and we assume a density, ρ=2800 kg/m^3.

The stress drop can then be expressed in terms of a_{RMS}, f_{max} and f_o:

$$\Delta\sigma_{a_{RMS}} = a_{RMS}\frac{106\rho R}{2R_{\theta\phi}(2\pi)^2\sqrt{2}}\sqrt{\frac{f_c}{f_{\max}}} \quad . \tag{10}$$

The a_{RMS}-stress drop varies as $\sqrt{f_c}$, whereas expressions for Brune stress drop vary as f_c^3 (Equation 1). Estimates of corner frequency are often highly variable and may be very dependent on method [e.g., *Sonly and Abercrombie*, 2006; *Kane et al.*, 2011]. Insufficient attenuation corrections can also affect the measured corner frequency, and for events M < 6 with high attenuation, f_{max} becomes the observable corner frequency, placing an artificial lower bound on stress drop (*Anderson*, 1986). Based on corner frequency dependence alone, the a_{RMS}-stress drop should be much less variable than the Brune stress drop; however, we find that the eGf method reduces the uncertainties to the point that the a_{RMS} and eGf stress drops compare closely.

We use data from 52 earthquakes of two mainshock-aftershock sequences in eastern Honshu, Japan, recorded at KikNet borehole and surface stations (Figure 4.1), consistent with the data from the eGf study. Because the ground motions are larger on the horizontal components, and the a_{RMS} formulation in (10) accounts for equal partitioning, records are averaged horizontal accleration. For both earthquake sequences, the corner frequency, f_c, and seismic moment, M_o, were previously determined by *Baltay et al.* [2011]. We measure the root-mean-square acceleration of the time series from the horizontally averaged acceleration data, a very simple measurement on a single recording (Figure 4.1). We choose a window of duration $T_d=1/f_c$ for each event-station pair that maximizes

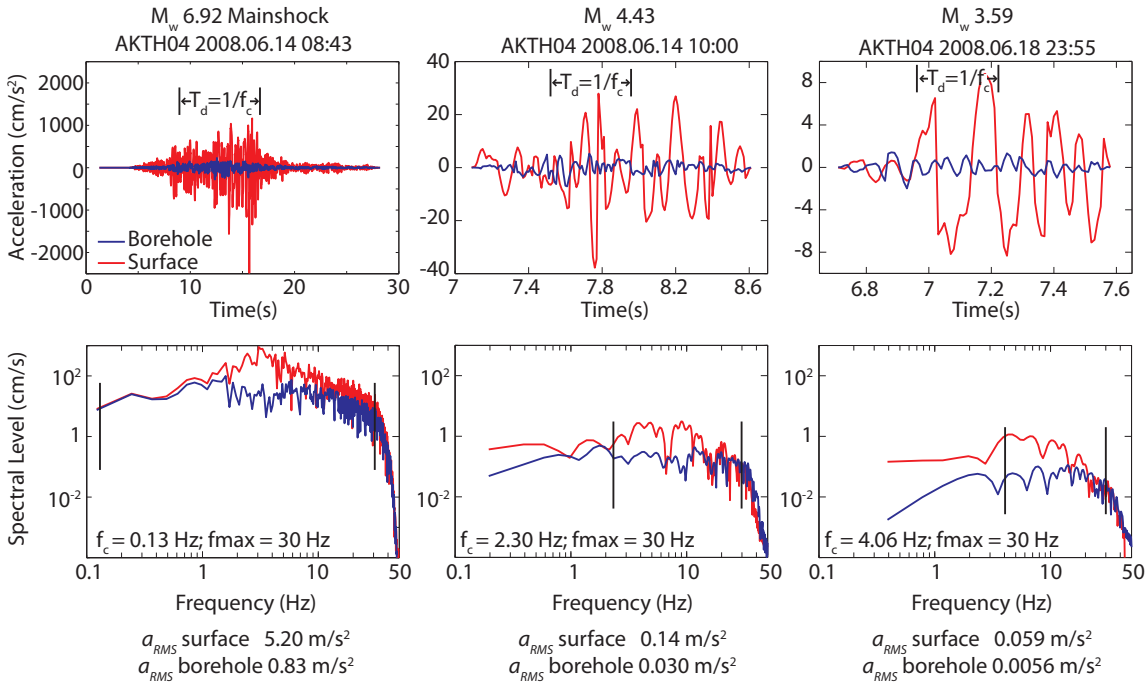

Figure 4.1 Time series (top row) and spectra (bottom row) for three events from the Iwate-Miyagi 2008 sequence, recorded at KikNet station AKTH04, with borehole recordings in blue and surface recordings in red. Note different time and amplitude scales on time-series. In each case, the faulting duration, $T_d=1/f_c$ used in the RMS-acceleration calculation is shown (top row) and the corresponding f_c and f_{max} =30 Hz (bottom row).

the *rms* of both the borehole and surface data. In practice, the apparent duration will only be equal to the true source duration at stations perpendicular to the fault trace. At other stations, the recorded duration will be longer or shorter due to directivity; however, the a_{RMS} measurement is not strongly dependent on the duration of the window used. By visually analyzing the data, we note that the acceleration spectra are relatively flat up to 30 Hz, which we define as f_{max}, for both the surface and borehole data. This is also the KikNet instrumental corner frequency, so it would be invalid to use a higher f_{max}. a_{RMS}-stress drop is determined from Equation (10) with ρ=2800 kg/m^3 and β=3600 m/s, and the previously determined corner frequencies.

Figure 4.2 (a) shows a_{RMS}-stress drops for the Iwate-Miyagi mainshock and two aftershocks of M_w *4.4* and M_w *3.6.* We find the surface a_{RMS}-stress drops to be, on average, about a factor of 4 larger than those determined from borehole measurements, which we attribute to surface amplification, lower impedance near the surface, and less near-surface attenuation effect for the borehole data (Figure 4.3a). Because the a_{RMS}-stress drop was originally formulated for, and meant to be applied to, surface

measurements, in the analysis that follows we only compare the surface measurements to the eGf-based stress drops. For the mainshock, the a_{RMS}-stress drop is stable at all source-station distances and decays slightly with R > 50 km. The M_w *4.4* aftershock, however, shows stress drop decaying at stations farther than ~20 km, and the Mw 3.6 aftershock shows even stronger decay of stress drop values with distance. Because smaller events have higher corner frequencies, and hence smaller high-frequency bandwidth compared to larger events (Figure 4.1, bottom row), their rms acceleration is more strongly attenuated at distance than it is for larger earthquakes. Taking a_{RMS}-stress drops from both sequences, as measured at stations within 10, 20 and 30 km (Figure 4.4a) highlights the loss of signal to attenuation. At R <10 km, the mean a_{RMS}-stress drop is 5.2 MPa, and log10-std = 0.34. With R<20 km, the mean decreases to 4.4 MPa due to inclusion of attenuated measurements, and the log10-std rises to 0.42. At R<30 km, the effect of attenuation is more severe, with a mean of only 4.0 MPa and log10-std = 0.43. To account for the attenuation, we compare an ideal, Brune acceleration spectrum that is flat in the frequencies of interest, [f_c, f_{max}] to a modeled attenuated acceleration spectrum. The attenuated spectrum is modified by $\exp\left(\frac{-\pi R f}{Q\beta}\right)$, with $Q=64f^{0.8}$ regionally defined and frequency

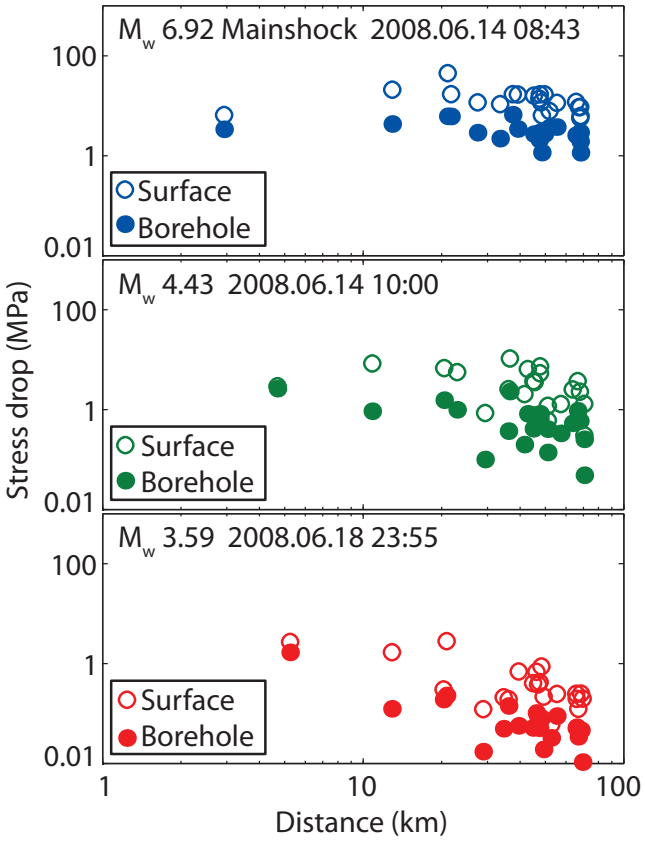

Figure 4.2 a_{RMS} stress drop as a function of distance for three earthquakes: M_w *6.9* Iwate-Miyagi mainshock; M_w *4.4* Iwate-Miyagi aftershock; and M_w *3.6* Iwate-Miyagi aftershock. a_{RMS}-stress drop estimates shown from both surface and borehole data. Surface data are a factor of ~4.5 times as large as borehole data, attributable to surface amplification and material contrast. For the mainshock, data are not attenuated much and stress drop estimate is fairly constant at far distances. For the smaller aftershocks, however, signal is highly attenuated and stress drop estimates are much lower at stations farther than ~30 km.

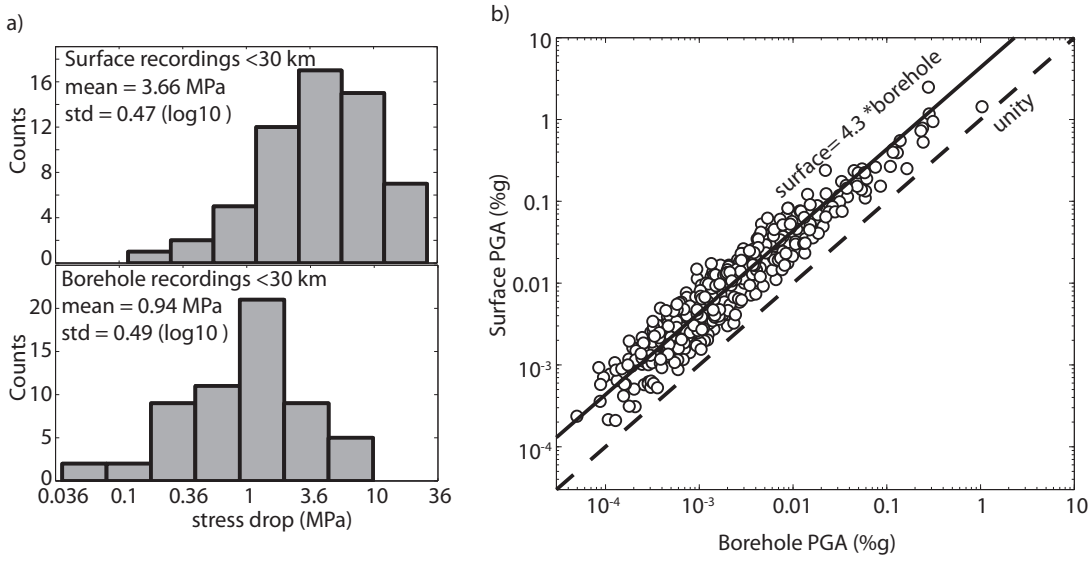

Figure 4.3 PGA measured at borehole and surface locations. Overall, the surface PGA is 4.3 times larger. (b) Stress drop measurements from the a_{RMS} method for surface (top) and borehole (bottom) recordings. The surface stress drops have a mean about 4 times larger than the borehole stress drops, but the std of the distributions is about the same.

dependent (*Nakamura,* 2010). We compute the percentage loss from the integral in [f_c, f_{max}] of the attenuated spectrum at each source-site distance compared to the ideal acceleration spectrum. We then correct each a_{RMS}-stress drop measurement by the inferred loss. We find that while this attenuation correction removes a distance dependent decay of stress drop, the correction rapidly becomes much larger than the measurement. That is, the loss ratio in many cases is greater than 75%. Rather than attempt to make this correction, we choose to restrict our stress-drop comparison to source-station distances of ≤20 km for which attenuation effects are small.

4.4 a-RMS vs eGf Stress Drops

We compare the a_{RMS}-stress drops to the eGf based stress drops *Baltay et al.* [2011] in Figures 4.4 and 4.5, using a source-receiver distances of less than 20 km for the a_{RMS}-stress drops. For each sequence, the stress drop is shown for both methods as a function of moment. In most cases the a_{RMS}-stress drop compares well to the eGf stress drop (Figure 4.4b). For some of the smaller events, the a_{RMS}-stress drop underestimates the eGf-stress drop,which may be due to the increased importance of attenuation at high

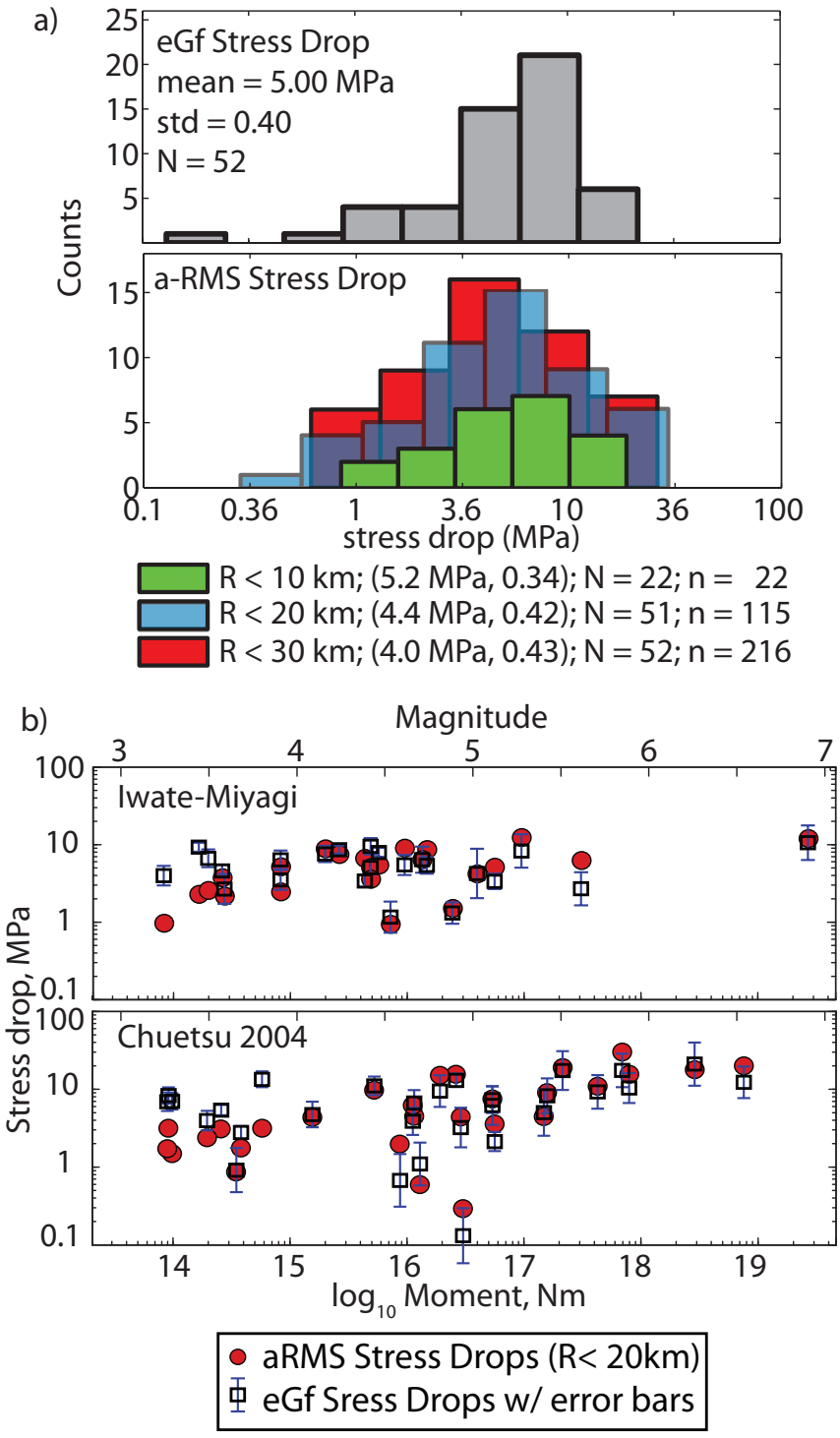

Figure 4.4 (a) Comparison of eGf stress drop distribution with a_{RMS}-stress drops, with mean and log10-std given in parenthesis, for three different distance ranges: R<30 km, R<20 km and R<10 km. As the distance range increases, measurements that are more attenuated are included into the distribution, causing the mean to decrease and the std to increase. Using only stations within 10 km yields a distribution similar to that from the eGf method. In each case, *N* is the total number of events considered and shown in the histograms; while *n* indicates the number of recordings incorporated in total. (b) a_{RMS}-stress drops compared to egf-stress drops. For most events, the a_{RMS}-stress drop is very close to the eGf stress drop.

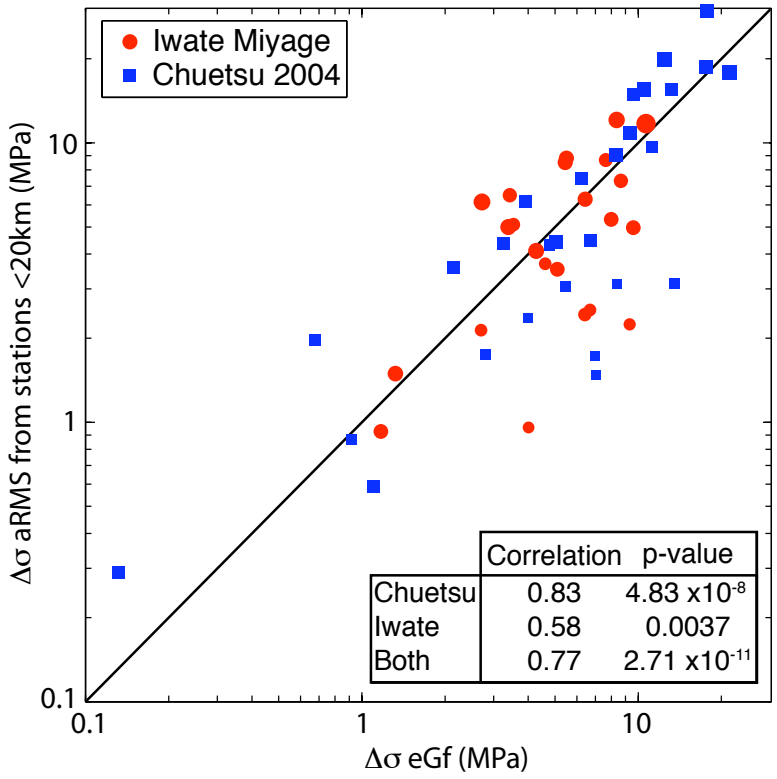

Figure 4.5 a_{RMS}-stress drop, given as the average over all stations within 20 km, compared to eGf stress drop. The correlation between the stress drops is strong for the Chuetsu and Iwate-Miyagi data separately, as well as together. In all cases, the p-value is much less than 0.05, the level of the test, indicating that the correlation is significant. Note that the a_{RMS}-stress drop recovers a similarly low stress drop, as compared to the eGf method, for the enervated earthquake in the lower left.

frequencies for the smaller earthquakes. The correlation between a_{RMS}-stress drop and eGf stress drop is 0.77 for both sequences considered together, 0.83 for the Chuetsu 2004 sequence alone, and 0.58 for the Iwate-Miyagi sequence. The P-values, or probability of obtaining the above correlation values under the null hypothesis, are 2.71×10^{-11}, 4.83×10^{-8} and 0.0037 respectively, much below the 0.05 significance level (95% confidence) of the test, substantiating the given correlations (Figure 4.5). One event, highlighted in *Baltay et al.* [2011] with an anomalously low eGf stress drop, has a similarly low a_{RMS}-stress drop, and is located in the lower left corner of the plot.

The a_{RMS}-stress drop follows a log-normal distribution with mean 4.4 MPa and log10-std of 0.42 (for R<20 km), while the eGf stress drops for the same 52 events also follow a log-normal distribution, with a very similar mean of 5.0 MPa and log10-std of 0.40 (Figure 4.4a). The variance of stress drop from the a_{RMS} method is similar to that from the eGf method, and not greatly reduced as might be expected based on the corner frequency relationship alone, even though the standard deviation of stress drop from each individual

event, based on corner frequency variation, is lower for the a_{RMS} method (Figure 4.4b). This indicates that the source of variability in stress drop measurements is reflecting inter-event variability, rather than uncertainties in the measurement method.

The comparison with a_{RMS}-stress drops illustrates that the eGf method of *Baltay et al* [2011] is robust in removing path and site effects. For close stations (R<20 km) or for larger events for which attenuation at high frequencies has less impact on the a_{RMS} measurement, the a_{RMS} method gives similar stress drops as the eGf method, at a fraction of the computational cost. The eGf method needs a mainshock and a well recorded eGf event at the same station, requiring assumptions about the corner frequency and spectra shape of the eGf, and depends on an iterative spectral flattening scheme (see *Baltay et al.,* 2010). Meanwhile, the a_{RMS} method is less computationally and algorithmically intensive, as each event record can be measured independently with fewer assumptions.

The a_{RMS} method could be used to estimate stress drop in near-real time, as only records from nearby stations with length T_d are required (although a_{RMS} is not highly dependent on T_d), and some knowledge of the moment, corner frequency, or duration of the event. Such an approach would only require low-intensity data retrieval, and ought to be straightforward to implement. Earthquakes with higher stress drop give rise to larger ground motions, so rapid assessment of earthquake stress drops could provide more reliable ground motion predictions in the immediate aftermath of an earthquake. The a_{RMS} method could also be implemented in tectonic settings with low seismic activity, as no eGf calibration event is required.

4.5 Predicting PGA

Peak ground acceleration (PGA or a_{max}), the maximum acceleration recorded from an event, is an important parameter for describing earthquake hazard and is often used in engineering to understand the forces imparted on structures from an event.

While PGA describes the maximum acceleration over an entire record, a_{RMS} describes the acceleration over the duration time window and may be more useful for some engineering applications. Using the assumption that acceleration time histories are

stationary, random, band limited, white Gaussian noise, a_{max} (PGA) and a_{RMS} can be related as below,

$$\frac{a_{\max}}{a_{RMS}} = \sqrt{2\ln\left(\frac{2T_d}{T_o}\right)} \tag{11}$$

where T_d is the duration of the signal, defined above as $1/f_c$, and T_o is the predominant period, taken here to be $1/f_{max}$, the highest frequency considered [*Hanks and McGuire*, 1981; *Vanmarcke and Lai*, 1977]. Equation (11) then becomes

$$\frac{a_{\max}}{a_{RMS}} = \sqrt{2\ln\left(\frac{2f_{\max}}{f_c}\right)}. \tag{12}$$

We measure the data PGA from the horizontally averaged KikNet acceleration data, and normalize by the right side of Eq. 12 to compare to measured a_{RMS} (Figure 4.6). Both surface and borehole recordings show that PGA is predictable from a_{RMS}. The surface recordings are about a factor of 4 larger, attributable to surface amplification and material contrast (Figure 4.3b).

We represent PGA (a_{max}) theoretically by combining Eq. 9 and 12

$$PGA = 2R_{\theta\phi}(2\pi)^2 \frac{\Delta\sigma}{106\rho R}\sqrt{\frac{f_{\max}}{f_c}}\sqrt{2\ln\left(\frac{2f_{\max}}{f_c}\right)} \tag{13}$$

and note that it is dependent on stress drop $\Delta\sigma$ and corner frequency f_c for any given earthquake with moment M_o at distance R. To avoid a distance dependence, we consider the quantity PGA·R, making Figure 4.7 visually easier to understand. To model the theoretical $PGA \cdot R$, we use an input stress drop distribution from *Baltay et al.* [2011] with a mean of 5.12 MPa and log10-std of 0.42 for the two mainshock-aftershock sequences studied here. The propagated error for $PGA \cdot R$ is log10-std = 0.51 (dashed lines in Figure 4.7). Then for a range of given moments for M_w *3* - M_w *8*, we calculate the corner frequency from Equation 1, and input the mean stress drop and corner frequency

into Equation 13. Figure 4.7 compares the theoretical $PGA \cdot R$ to the data measured $PGA \cdot R$, with R the hypocentral distance for each event-station recording.

We also note, as in *Hanks and McGuire* [1981], that the dependence of *PGA* on moment is very weak. Substituting in equation (8) to show *PGA* as a function of moment,

$$PGA = 2R_{\theta\phi}(2\pi)^2 1.43 \frac{\Delta\sigma^{5/6}}{106\rho R\beta^{1/2}} \sqrt{f_{\max}} M_o^{1/6} \sqrt{2\ln\left(\frac{2.86 f_{\max}}{\beta\, \Delta\sigma^{1/3}} M_o^{1/3}\right)} \tag{14}$$

This can be approximated to almost exactly $PGA \propto M_o^{1/5}$ for $3.0 < M_w < 6.5$. Substituting $\log_{10} M_o = 1.5\, M_w + 9.05$, we see that the dependence of *PGA* on magnitude is very weak

$$\log_{10} PGA \propto 0.3 M_w . \tag{15}$$

Figure 4.7 also highlights this trend. Over 4 orders of magnitude, from M_w *3.0* to M_w *7.0*, the measured *PGA*distance* increases less than 2 orders of magnitude, on average. The closest data which are best represented by the simple model, increase only by a factor of 10 between M_w *3.3* and M_w *6.9*.

For larger events, $M_w > 5.5$, and close stations, R < 20 km, the theoretical relationship for PGA estimates the data very well. Figure 4.7 shows R^2 goodness of fit values of the *PGA* data to the model (solid black line). For data recorded at <5 km distance, the model does an excellent job at predicting the data, with an R^2 of 0.82. For the data at farther ranges, however, the goodness of the model fit to the data is decreased, with R^2 = 0.59 for 5 – 10 km and R^2 = 0.56 for 10 – 20 km. For the smaller events, especially at farther distances, attenuation accounts for significant signal loss, as discussed above, because the smaller events have limited band-width, as compared to the more broadband records of larger events. The theoretical formulation for PGA does not model any attenuation or other loss as the waves propagate, and is thus unable to match the data at distances and magnitudes that are significantly affected by attenuation.

Overall, the theoretical relationships developed can be used to predict PGA reliably for large ($M_w > 5.5$) events at event-station distances up to 30 km, and for $M_w > 3.0$

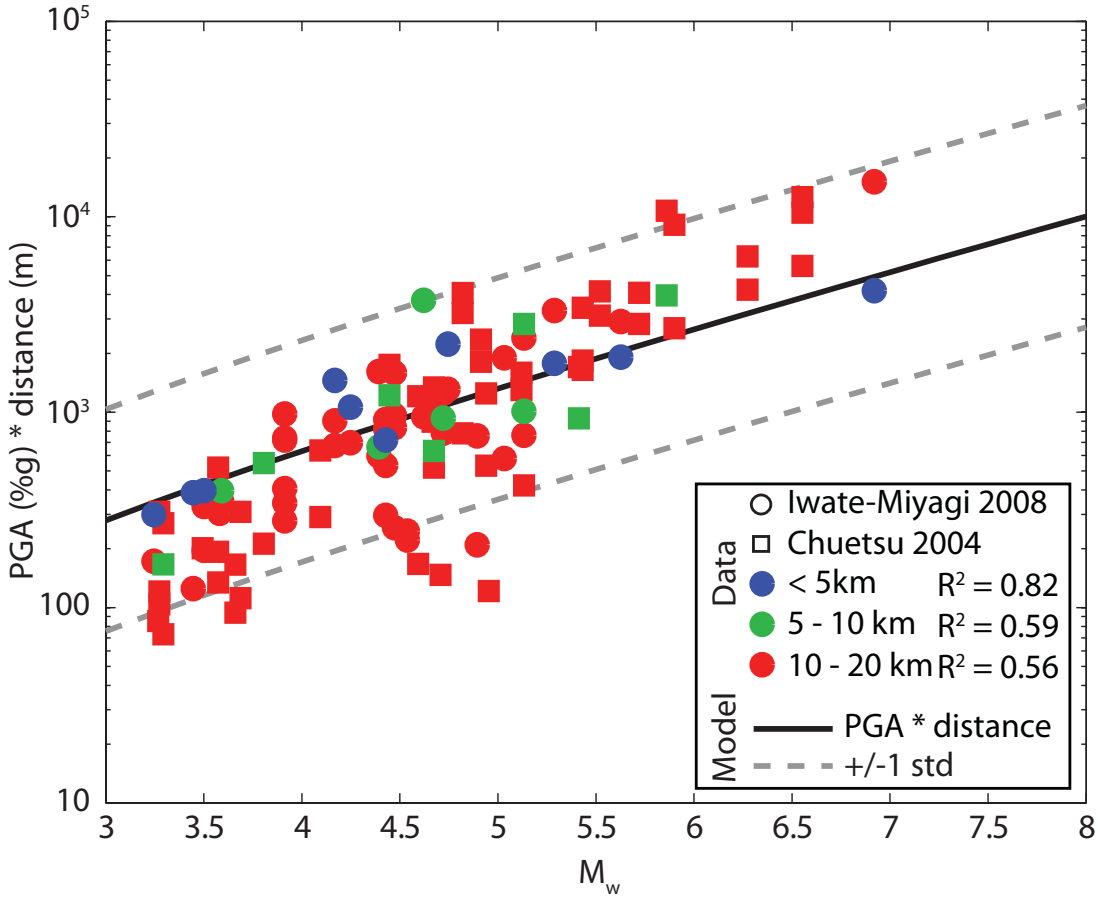

Figure 4.7 Observed PGA compared to predicted PGA from theory. Solid black line shows the theoretical PGA relation, normalized without distance. Dashed lines show theoretical standard deviation based on the input stress drop distribution. Measured PGA shown color-coded by distance, also normalized without distance. For larger events (right side of plot) and closer event-site distances (blue), the theoretical relation does a good job of predicting the data. For smaller events and farther distances, attenuation causes the measured PGA to be much lower than the theoretical predicted PGA, which does not model attenuation. The R^2 values for goodness of fit for each data distance range are given. The R^2 for the very close (<5 km) is significantly higher than the farther distances.

earthquakes at stations up to ~10 km distance. This emphasizes that earthquake acceleration time histories are band limited, white Gaussian noise, an assumption that can be used for stochastic ground motion simulation. The loss of energy from attenuation for smaller events and those farther than ~10 km emphasizes the necessity of attenuation relations in describing PGA, as well as the need for path correction when considering earthquake source measurements.

4.6 Discussion and Conclusions

We estimate stress drop directly from acceleration records from two earthquake sequences in eastern Honshu, Japan, using seismic moments and corner frequencies as determined by *Baltay et al.* [2011]. The a_{RMS} method had previously not been robustly compared to other stress drop methods using such a well-recorded data set. The a_{RMS}-stress drop is log normally distributed and compares well to the eGf method of *Baltay et al.* [2011], but suffers a loss of signal for smaller events and farther distances due to anelastic attenuation. In this study, we do not correct the time-domain, a_{RMS} measurements for any attenuation or other path effect, except a simple *1/R* spreading. Based on corner frequency uncertainty, the a_{RMS} method yields smaller errors for stress drops of individual earthquakes, but shows a similar stress drop distribution for all events together. We find the log10-std of the a_{RMS}-stress drops, 0.42 for R≤20 km, to be similar to that of the eGf method, 0.40. These two methods are measuring inherently different parts of the spectrum: frequencies near f_c are important in determining the eGf stress drop, while frequencies higher than the corner are used in the a_{RMS} method. The implication is that variability in stress drop measurements stems from inter-event source variability and is not inherent in the method. This also underscores that the eGf method is a huge improvement over traditional methods of estimating stress drop.

We also use the theoretical relationships to predict PGA (a_{MAX}), and find that for the larger events (M_w>*5.5*) at distances up to 30 km, and for smaller events at closer distances, < ~10 km, PGA is predictable given a generic input stress drop distribution and earthquake moment.

The a_{RMS} method is computationally simpler than the eGf method, and can be used to estimate stress drop quickly and easily from close stations, as it only requires one acceleration record and knowledge of the magnitude, corner frequency, or faulting duration of the event. It is possibly to adapt this method to estimate stress drop and other source parameters in real time, and also in areas where earthquake activity is lower.

The results that we find here support the analysis originally performed by *Hanks* [1979] and *Hanks and McGuire* [1981] who showed that stress drop could be computed

from acceleration records, and that PGA was predictable within 50% from source parameters. The underlying assumption that earthquake acceleration records are white Gaussian noise, with a flat power spectral density within the band limit from the corner frequency to the maximum frequency, is reinforced with these results. Furthermore, the a_{rms}-stress drop results further support a self-similar ω^{-2} earthquake model, as discussed in *Baltay et al.* [2011], in that we see a constant stress drop for all sizes of earthquakes.

The comparison between the eGf method and a_{RMS} method emphasizes the robustness of the eGf method at estimating source parameters, as it negates all source and path effects in the analysis. In the eGf analysis, more data is able to be incorporated from stations at much farther distances. In order to estimate source parameters with a method that doesn't rely on direct comparison of events with similar paths, such as the eGf method, accurate attenuation relations are absolutely necessary when incorporating data at distances farther than 10 - 20 km. Use of the a_{rms} method, however, can expand the current data set of stress drop measurements, increasing our knowledge of earthquake source parameters and associated variability.

Data and Resources

Acceleration data from KiK-net data are available online (www.kik.bosai.go.jp/kik/) through National Research Institute for Earth Science and Disaster Prevention.

Acknowledgements

This research was supported by the Southern California Earthquake Center through the Extreme Ground Motion project. SCEC is funded by NSF Cooperative Agreement EAR-0106924 and USGS Cooperative Agreement 02HQAG0008. The SCEC contribution number for this paper is 1519. A. Baltay was supported at Stanford by a Gabilan Stanford Graduate Fellowship.

References

Aki, K. (1967), Scaling law of seismic spectrum. *J. Geophys. Res. 72*, 1217 – 1231.

Anderson J. G. (1986), Implications of attenuation for studies of the earthquake source, in *Earthquake Source Mechanics*, edited by S.Das, J. Boatwright and C. H. Scholz, AGU Monograph, 37, 311-318

Baltay, A., S. Ide, G. Prieto, and G.Beroza (2011), Variability in earthquake stress drop and apparent stress, *Geophys. Res. Lett*., *38*, L06303, doi:10.1029/2011GL046698.

Beeler, N. M. (2006). Inferring earthquake source properties from laboratory observations and the scope of lab contributions to source physics, in Earthquakes: Radiated Energy and the Physics of Faulting, Geophys. Monogr. Ser., vol. 170, edited by R. Abercrombie et. al., pp. 99 - 119, AGU, Washington, DC.

Boore, D. M. (1983). Stochastic simulation of high-frequency ground motions based on seismological models of the radiated spectra, *Bull. Seism. Soc. Am., 73*, 1865-1894.

Boore, D. M. and W. B. Joyner (1989). The effect of directivity on the stress parameter determined from ground motion observations, *Bull. Seism. Soc. Am., 79*, 1984-1988.

Brune, J. N. (1970), Tectonic Stress and the Spectra of Seismic Shear Waves from Earthquakes, *J. Geophys. Res., 75*(26).

Chiou, B. S.-J. and R. R. Youngs (2008), An NGA Model for the Average Horizontal Component of Peak Ground Motion and Response Spectra, *Earthquake Spectra*, *24*, 1, pages 173–215.

Hanks, T. C., (1979), b-values and ω-γ seismic source models: implications for tectonic stress variations along active crustal fault zones and the estimation of high-frequency strong ground motion, *J. Geophys. Res., 84*, 2235-2242.

Hanks, T. C. (1982), fmax, *Bull. Seism. Soc. Am., 72*, 1867-1879.

Hanks, T. C., and W. Thatcher (1972), A graphical representation of seismic source parameters, *J. Geophys. Res., 77,* 4292-4405.

Hanks, T. C., and R. K. McGuire (1981), The character of high-frequency strong ground motion, *Bull. Seism. So. Am., 71*, 2071-2095.

Ide, S., and G. C. Beroza (2001), Does apparent stress vary with earthquake size?, *Geophys. Res. Lett., 28*(17), 3349.

Ide, S., G. C. Beroza, S. G. Prejean, and W. L. Ellsworth (2003), Apparent break in earthquake scaling due to path and site effects on deep borehole recordings, *J. Geophys. Res., 108* (B5).

Kanamori H., and D. L. Anderson (1975), Theoretical basis of some empirical relations in seismology, *Bull. Seism. Soc. Am., 65,* 1073-1096.

Kane, D. L., G. A. Prieto, F. L. Vernon, and P. M. Shearer (2011), Quantifying seismic source parameter uncertainties, *Bull. Seism. Soc. Am., 101*, 535-543.

Keilis-Borok, V. I., *Investigation of the Mechanism of Earthquakes*, (in Russian), *Tr. Inst. Geofis. Akad. Nauk, SSSR*, 40, 1957. (Engl. transl., *Sov. Res. Geophys*. Set., vol. 4, 1960.)

McGuire, R. K., and T. C. Hanks (1980), RMS accelerations and spectral amplitudes of strong ground motion during the San Fernando, California Earthquake, *Bull. Seism. Soc. Am., 70,* 1907-1919.

Nakamura, R. (2010), 3-D Attenuation structure beneath the Japanese islands, source parameters and site amplification by simultaneous inversion using short period strong motion records and predicting strong ground motion, Ph.D. Thesis, University of Tokyo, Japan.

Petersen, M. D., A. D. Frankel, S. C. Harmsen, C. S. Mueller, K. M. Haller, R. L. Wheeler, R. L. Wesson, Y. Zeng, O. S. Boyd, D. M. Perkins, N. Luco, E. H. Field, C. J. Wills, and K. S. Rukstales (2008), Documentation for the 2008 Update of the United States National Seismic Hazard Maps: U.S. Geological Survey Open-File Report 2008–1128, 61 p.

Sonley, E., and R. E. Abercrombie (2006), Effects of Methods of Attenuation Correction on Source Parameter Determination, in Earthquakes: Radiated Energy and the Physics of Faulting, Geophys. Monogr. Ser., vol. 170, edited by R. Abercrombie et. al., pp. 91 - 97, AGU, Washington, DC.

Vanmarcke, E. H., and S. P. Lai (1977), Strong-motion duration of earthquakes, Dept. of Civil Eng. Pub. No. R77-16, Massachusetts Institute of Technology, Cambridge.

Venkataraman, A., G. C. Beroza and J. Boatwright (2006), A brief review of techniques used to estimate radiated seismic energy, in Earthquakes: Radiated Energy and the Physics of

Faulting, Geophys. Monogr. Ser., vol. 170, edited by R. Abercrombie et. al., pp. 15 - 24, AGU, Washington, DC.

CHAPTER 5

Radiated Energy of Great Earthquakes from Teleseismic Empirical Green's Function Deconvolution

Abstract

We estimate radiated energy for five recent great earthquakes using teleseismic empirical Green's function deconvolution, expanding on the method of *Ide et al.* [2011]. We study the five largest earthquakes worldwide over the last 10 years: Tohoku-Oki, Japan 2011 M_w *9.0*; Sumatra, Indonesia 2004 M_w *9.1*; Maule, Chile 2010 M_w *8.8*; Nias, Indonesia 2005 M_w *8.7*; and Bengkulu, Indonesia 2007 M_w *8.5*. *P*-wave vertical arrivals and *S*-wave radial and transverse arrivals give consistent energy results, which are comparable to those found by other researchers, validating this new method. Apparent stress for the five great earthquakes is between 0.4 and 0.8 MPa, which is within the spread of apparent stress from global earthquakes over a large magnitude range. The azimuthal distribution of energy in each case shows directivity, and in some cases, shows more energy radiated down-dip and along the trench, which may suggest enhanced tsunami potential. We find that eGf's as small as ~ M 6.5 can be used for teleseismic deconvolution, and that an eGf-mainshock magnitude difference of 1.5 units yields stable results. This implies that M 8 is the minimum mainshock size for which teleseismic eGf deconvolution will work well. We propose that a database of eGf events could be used to calculate radiated energy and apparent stress of great, hazardous events in near real time.

The material in this chapter is in preparation for publication with co-authors S. Ide and G. C. Beroza

5.1 Introduction

Great earthquakes, $M_w > 8.5$, are rare and devastating events. Until the occurrence of the 2004 Sumatra M_w *9.1*, no broadband digital recordings existed for these very large events, and precise source parameters were undetermined. The Sumatra 2004 event came with surprises- an extended rupture zone of almost 1300 km in length, and a giant tsunami that caught much of the world unaware. The Tohoku-Oki 2011 M_w *9.0* earthquake had a much more compact source zone and in contrast to the Sumatra 2004 event, generated high frequencies at the deep edge of the rupture with slower, higher amplitude slip at the trench, accounting for the tsunami. Although the site of the Tohoku-Oki event was deemed the most likely location for a future magnitude 7.5 – 8 earthquake, hazard models did not account for the ~M 9 megathrust, as these giant events occur so infrequently, and seldom recur in the same locality. Because each of these earthquakes is rare and unique, we need to understand as much about them as possible.

Radiated seismic energy is a basic observable measure of the strength of an earthquake, and can be related to other physical parameters, such as fracture energy, rupture velocity and stress drop, which can aid in understanding of rupture dynamics. By studying the relationship between radiated seismic energy, a dynamic parameter, and seismic moment, a static measure of the earthquake's size, we can gain insight into the dynamic processes of an earthquake. Whether all earthquakes have the same ratio of seismic energy to moment, E_R/M_o, obeying self-similar earthquake physics, remains an open question, and how the very largest earthquakes radiate energy is not well understood.

One class of earthquakes that may display abnormal ratios of E_R/M_o are "tsunami earthquakes," those that cause a much larger tsunami than might have been expected simply given the earthquake magnitude [*Kanamori,* 1972]. *Newman and Okal* [1998] found that many of these tsunami earthquakes have anomalously low ratios of radiated energy to seismic moment, emphasizing the importance of precise determination of these source parameters. On the other hand, great earthquakes may be tsunamigenic (tsunami causing) without being deficient in radiated energy. It is imperative to understand the

relationship between radiated energy, tsunami and earthquake dynamics in order to mitigate risks associated with large earthquakes.

Radiated seismic energy is the amount of energy that would be radiated in an infinite, lossless medium [*Haskell,* 1964]. In reality, radiated seismic waves are attenuated, focused/de-focused and scattered as they travel through the Earth, encountering heterogeneous earth structure, before being recorded at a seismic station. Radiated seismic energy is measured from the integral of the squared velocity source spectrum of an earthquake, but to estimate the quantity accurately, the recorded seismogram must be corrected to remove path and site effects.

Typically, estimates of energy for large earthquakes are computed teleseismically by making path corrections to account for attenuation and geometrical spreading, as well as site and surface corrections [*Choy and Boatwright*, 1986; *Perez-Campos et al.*, 2003; *Convers and Newman,* 2011]. Empirical Green's functions have been employed as an effective means for making these corrections for local earthquakes, without explicit knowledge of the corrections. Use of eGfs assumes that a smaller, collocated event, usually at least 1 magnitude unit smaller, can be modeled as an ideal Green's function between the source and station [e.g. *Hartzell,* 1978; *Courboulex et al.,* 1996; *Hough*, 2001; *Kane et al.,* 2011]. Then, the true source time function of the larger, mainshock event can be determined simply by deconvolving the Green's function event from the bigger event.

Empirical Green's functions have been used profusely on a local scale (within a few 100's of km) to correct to source spectra of earthquakes up to ~M 7 [*Venkataraman et al.,* 2002; *Ide et al.*, 2003; *Baltay et al*, 2010; *Baltay et al.,* 2011]. However, for great earthquakes for which the rupture dimension can no longer be considered negligible compared to the source-station distance, the local empirical Green's function assumptions break down. *Ammon et al.* [1993] showed that teleseismic surface wave deconvolution could work between earthquakes of magnitude 7.2 and 7.4 with eGf events of magnitude ~6 to resolve fault finiteness. When considered at teleseismic distances ($\Delta > 30^{o}$), even very large ruptures can be considered point sources, which leads us to consider large

earthquakes (~M 6.5 – ~M 7.5) as empirical Green's functions, located near the high-slip patches of larger earthquakes, to correct for path and site effects of great earthquakes.

We develop a new, teleseismic eGf deconvolution approach [*Ide et al.,* 2011] to model source spectra of five recent great earthquakes, well recorded on the Global Seismic Network: Sumatra 2004 *Mw 9.1*; Tohoku 2011 *Mw 9.0*; Maule 2010 *Mw 8.8*; Nias 2005 *Mw 8.7*; and Bengkulu 2007 *Mw 8.5.* We find that we can accurately estimate the radiated seismic energy using either *P* or *S* waves with this new method. The scaled energy, E_R/M_o, for all five events is about 1 – 2 x10^{-5}, corresponding to apparent stress between 0.4 and 0.8 MPa, consistent with many previous studies that consider events locally and teleseismically, over many orders of magnitude. We do not see an increase of scaled energy with moment, even for these largest events, leading to further support of earthquake self-similarity, at least as measured by radiated energy.

We also study the azimuthal directivity of radiated seismic energy from these very large events. We find that some of the earthquakes, especially the Tohoku-Oki 2011, have strong directivity, while others, such as the Bengkulu 2007, show less clear patterns. In general, the energy shows directivity in the known direction of rupture, as emphasized with forward modeling by *Favrea and Archuleta* [2001]. When coupled with the time-dependent source inversion of *Ide et al.* [2011], we show that the along trench directivity of energy from the Tohoku-Oki 2011 event can be explained by the dual nature of that event. The lack of high frequency, radiated energy towards the trench may be compatible with tsunami generation, and we see a similar pattern in the other great earthquakes considered here. We model each rupture with simple Haskell line sources, and are able to fit the observations very well with these simple rupture models. We find at least a factor of two, and up to an order of magnitude, difference in energy from maximum to minimum, implying that directivity effects should be considered when estimating energy teleseismically.

Finally, we suggest that this method of radiated energy estimation can be adapted for use in real time, for rapid earthquake characterization. An eGf catalog could be built, with preprocessed, picked eGf events for each region in the world that could host to a

great earthquake. Since so little is still known about the great, hazardous events, any information learned quickly after the occurrence of the event has the potential to aid in risk mitigation.

5.2 Teleseismic eGf Deconvolution

We consider five great earthquakes recorded worldwide over the past 10 years, and nearby large earthquakes from ~M 6.0 to ~M 7.9 as potential empirical Green's

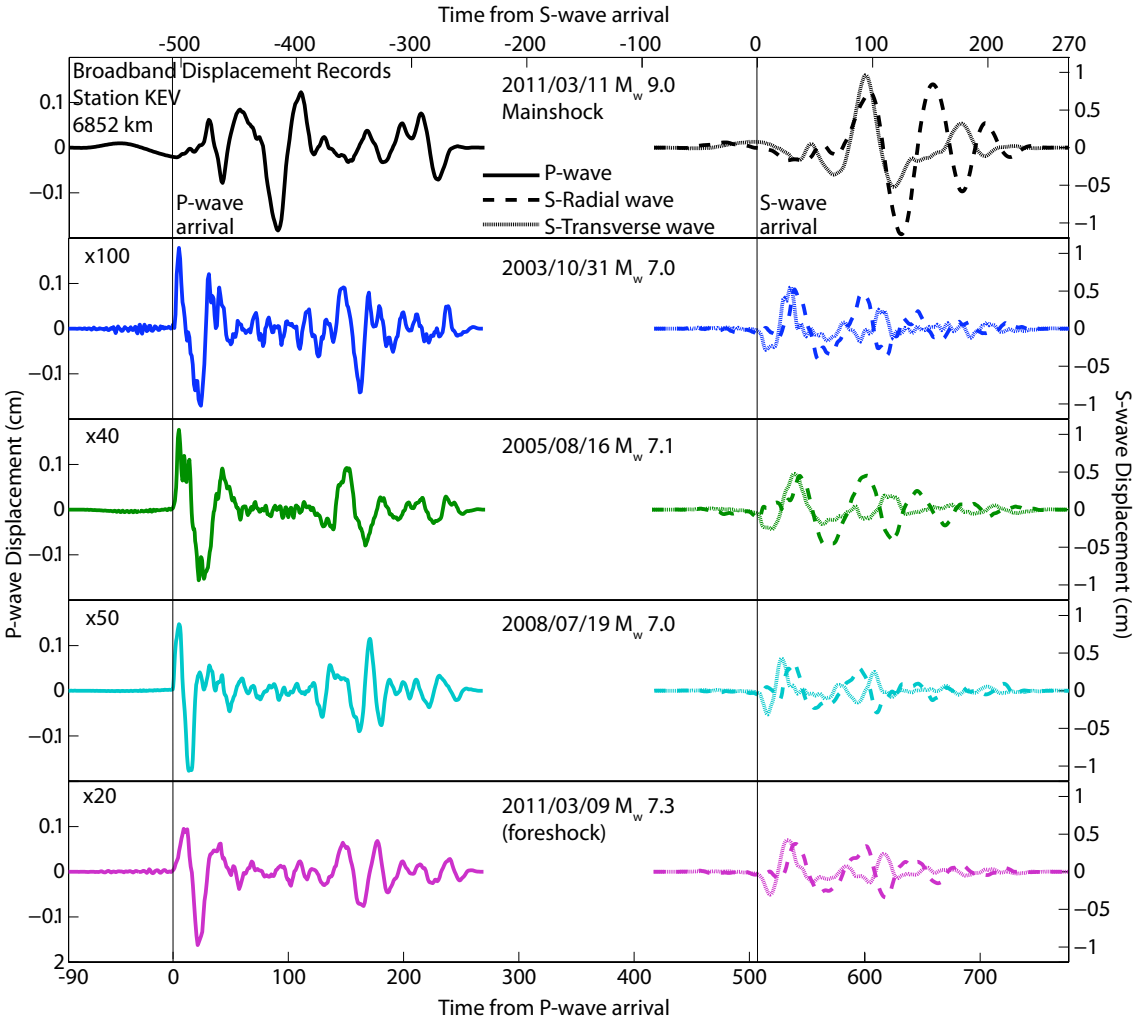

Figure 5.1 Broadband displacement waveforms from Tohoku-Oki 2011 mainshock (top panel) and 4 candidate eGf events, recorded at station KEV with a distance of 6852 km. Left seismograms are P-wave vertical recordings, right are the S-wave radial and transverse components, each windowed from 90 seconds before the first arrival to 270 seconds afterwards, and tapered. The eGf recordings are scaled by the factor shown in upper left corner of each panel.

functions. We estimate the energy of each mainshock by deconvolution of several candidate eGf's located near the mainshock, and of similar mechanism (low angle thrust, for all mainshocks). The eGfs considered occur both before and after the mainshock, except for the Sumatra 2004 and Maule 2010 eGfs, which all take place afterwards. We use data recorded by the Global Seismic Network at stations from Δ=30^o to Δ=90^o. Closer than 30^o, recordings will contain *S*-waves within 270 seconds, and beyond 90^o body waves interact with the earth's core.

Both *P* and *S* waves recorded by broadband global seismic stations in the GSN are used. For both the mainshock and eGf events, we analyze *P*-vertical (BHZ) records, windowed from 90 seconds before the *P* arrival to 270 seconds after, and *S*-horizontal components (BHE and BHN), rotated to radial and transverse directions, also windowed from 90 seconds before the *S* arrival to 270 seconds after. The spectrum from each component is then smoothed into 90 evenly log-spaced bins from 1 mHz to 10 Hz. Figure 5.1 shows example windowed *P* and *S* waveforms at one global station, KEV, for the Tohoku-Oki 2011 earthquake, and the 4 candidate eGf events.

The eGf spectra are corrected to a Brune ω-squared model, as in *Baltay et al.*, [2010] Eq. (1) (*Brune*, 1970). We use the USGS centroid moment, given in Tables 5.1-5.5, and a reference stress drop of 3 MPa (*Baltay et al,* 2010) to define the corner frequency, following *Hanks and Thatcher,* [1972], using β=3600 m/*s* (Eq 1).

$$f_o = \left(\frac{\Delta\sigma}{8.5 M_o} \right)^{1/3} \beta \qquad (1)$$

In log-log frequency space, deconvolution of the time series is equivalent to simple division of the mainshock spectra by the eGf spectra. The eGf events are corrected to be ideally Brune, and the mainshock is corrected by the same amount, so that the relative spectral levels between the two events are maintained. The lower frequency cut-off of the eGf event for each component is chosen so that there is the most coherency between the corrected mainshock spectra at all stations for each eGf, which is usually near 100 s. The absolute moment level of all spectra is set from the moment of the eGf, using the value

from the USGS Centroid Moment Tensor inversion (Figure 5.2a). Since all the eGf events are large earthquakes on their own right, reliable CMT inversions for moment exist.

Below the low-frequency cutoff of about 100s, the eGf spectra become unstable, and we are unable. We are unable to correct the mainshock from eGf deconvolution for these very low frequencies adequately, as the moment level of the mainshock is not measured through eGf deconvolution. Therefore, we extrapolate the mainshock spectrum to lower frequencies following an ω^{-2} trend, until the independent moment of both the eGf and mainshocks, from the USGS CMT solution, are recovered. It is also possible that teleseismic spectra are deficient in low-frequency energy in the time window considered, potentially due to shallow interference effect of the moment tensor components for shallow earthquakes at low frequencies [*Kanamori and Given*, 1981]. Figure 5.2 shows the extrapolated part of the spectra in light lines, implying a corner frequency between ~ .002 and .005, for Tohoku-Oki. The extrapolated portion of the

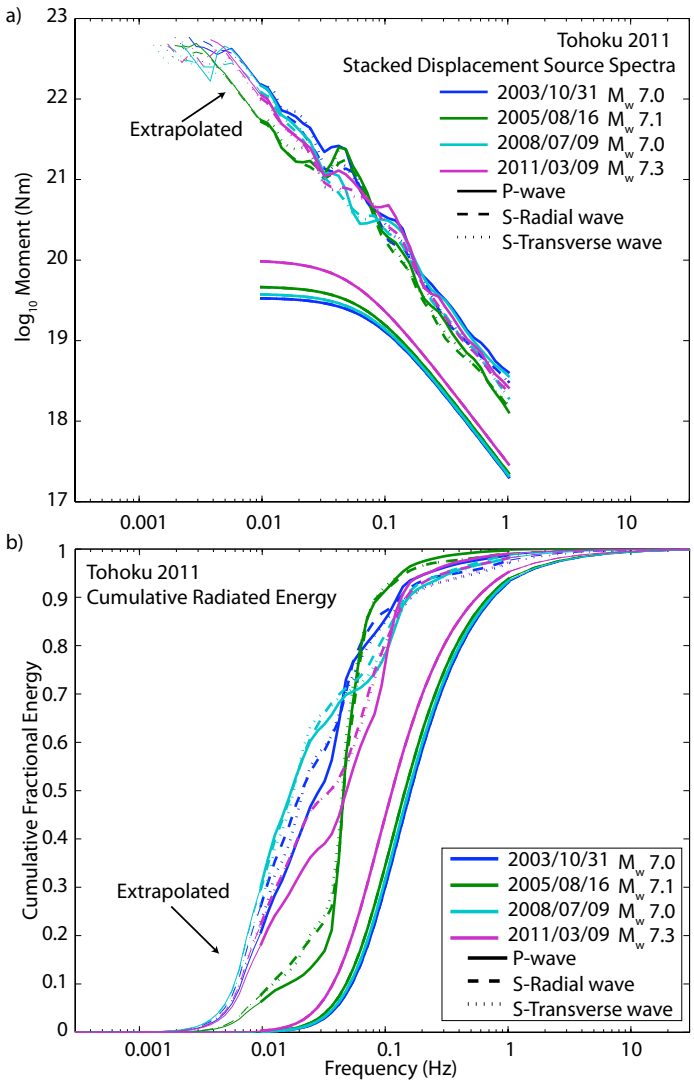

Figure 5.2 (a) Tohoku-Oki 2011 displacement source spectra for each eGf, and for the mainshock after deconvolving the different eGf events, stacked over all stations. (b) Cumulative fractional energy of the mainshock corrected individually by each eGf, and stacked over all stations. Light lines in the low frequencies of the mainshock in (a) and (b) show the missing, extrapolated energy, which amounts to ~10% - 20% on average.

spectra accounts for about 10% - 20% of the total energy of the mainshock, depending on the station and eGf used. The close correspondence of the mainshock spectra to each other, when corrected by different eGf events, indicates that the corrected source spectra and extrapolation into low frequencies are robust with respect to the eGf choice.

Radiated energy is proportional to the integral of the corrected velocity spectra squared,

$$E_R = \frac{1}{4\pi^2 \rho \beta^5} \int_0^\infty \left| \omega \cdot M(\omega) \right|^2 d\omega \tag{2}$$

where $\dot{M}(\omega)$ is the moment rate (displacement) spectrum, β=3.6 km/s, I=2/5 and ρ=3000 kg/m^3, which corresponds to ρ of other teleseismic studies so that energy results can be easily compared [*Convers and Newman*, 2011]. Once the corrected source spectra are calculated from eGf deconvolution, we estimate E_R for the mainshock as corrected by each eGf event, and for each of three components of motion. We also calculate apparent stress:

$$\tau_a = \mu \frac{E_R}{M_o} \tag{3}$$

with the shear modulus μ=39 GPa (*Wyss,* 1970).

5.3 Radiated Energy from Five Recent Great Earthquakes

For each of the five recent great earthquakes, we considered as many as 14 different empirical Green's function events, but use 4 – 5 for the final analysis. In each case, there is close correspondence of the mainshock spectra when corrected by each eGf (see corresponding figure), indicating that the corrected source spectra are robust. The cumulative fractional energy of the mainshock shows that the extrapolated energy is very small in some cases, and on average accounts for ~20% of the total energy.

We also indicate the part of the mainshock spectra that has been extrapolated into the low frequencies, below the low cut-off of the eGf, usually near 100 seconds. For an ideal Brune ω^{-2} spectrum, 80% of the energy is at frequencies below 6.25 times the corner frequency. For these very large events with corner frequencies of several hundred seconds, that value is well below 0.1 Hz, so we are certainly measuring most of the radiated energy.

We find that the use of *P*-vertical, *S*-radial and *S*-transverse waves give very similar mainshock corrected spectra and energy values, and the two *S* wave energies are even closer in value, emphasizing the precision of the energy estimates. *Boatwright and Choy* [1986] use only *P*-wave spectra for energy determination, because *S* waves become more attenuated at teleseismic distances; however, using an eGf correction, we are able to make use of *S* waves, essentially tripling the available data.

For all the events, we study the directivity of the radiated energy. Empirical Green's functions correct the mainshock for radiation patterns, but not for azimuthal variation, as the eGf events are much smaller and hence do not display their own strong directivity. The azimuthal distribution of mainshock energy is thus a source effect. The final energy estimates for each event represent an azimuthally weighted average, so that no cluster of nearby stations (in Europe or North America, for example) has too large an effect on the final radiated energy value.

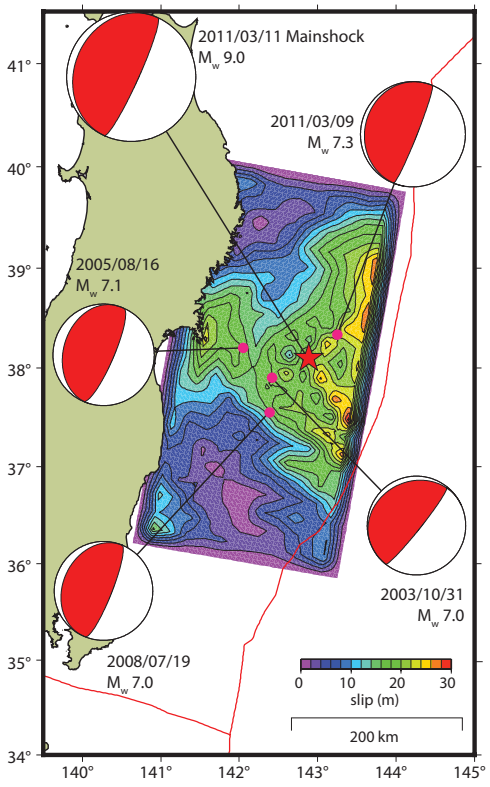

Figure 5.3 Map of Tohoku-Oki 2011 rupture area and candidate eGf events. Rupture slip plane from Ide et al. [2011]. Focal mechanisms and locations from gCMT catalog.

5.3.1 Tohoku-Oki 2011

The M_w 9.0 Tohoku-Oki earthquake of 2011 occurred on March 11 offshore of Honsu, Japan,

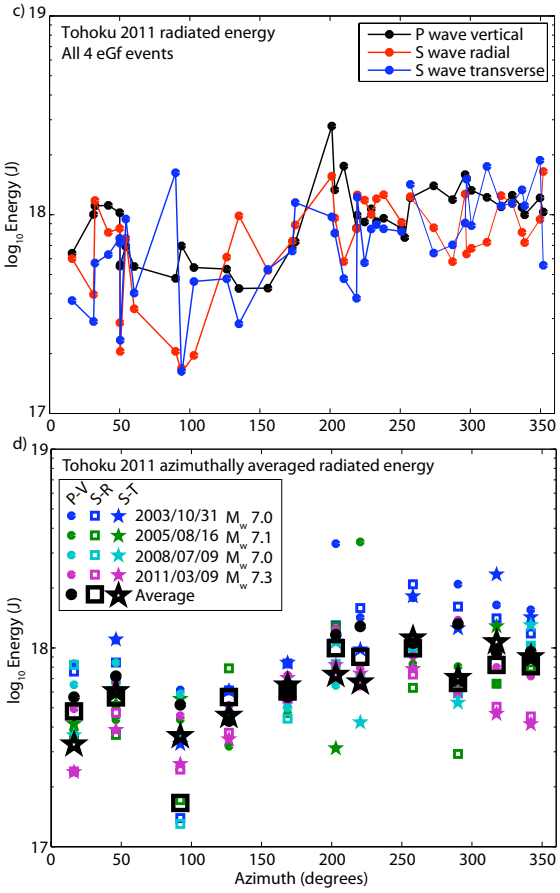

Figure 5.4 (c), (d) Mainshock radiated energy as a function of station azimuth. (c) Log10 average over all eGfs, for each component, shown at all stations. (d) Energy shown as corrected from each eGf event and each component, azimuthally weighted into 30-degree bins. Average of each bin shown in black, used for the final reported energy estimate. Different components shown with different symbol shapes.

on the Japan trench. The earthquake lasted about 160 seconds, on a rupture plane of about 240 km down dip x 440 km along strike of 200°, with prodigious shallow slip at the trench that caused a large tsunami (Figure 5.3) [*Ide et al.*, 2011]. Waveforms from the four eGf events show very similar patterns in both the *P* and *S* waves, although it is apparent that the mainshock had a much slower start before rapidly accelerating (Figure 5.1). The event was unusual in that it occurred on a compact rupture plane for an event of this size, but also had large, slow shallow slip coupled with high-frequency deep slip.

Overall, we find a radiated energy of 7.06×10^{17} J, a scaled energy $E_R/M_o = 1.57 \times 10^{-5}$, and apparent stress of 0.61 MPa (Table 5.1). This event showed strong directivity, with a minimum near 100° and a maximum near 200°, which also corresponds to energy directivity

Table 5.1 Radiated seismic energy of Tohoku-Oki 2011, corrected by each eGf, with given eGf moment and magnitude. The $\log_{10}$ average shown in right column is weighted azimuthally.

Catalog Information				Radiated Energy (Joules, x 10^{17})			
#	Date	M_o (Nm, x10^{19})	M_w	P-Vert.	S-Radial	S-Trans.	Average
4	2003/10/31	3.4	7.0	12.19	9.58	10.58	10.73
6	2005/08/16	4.7	7.1	6.56	5.25	5.84	5.86
9	2008/07/09	3.8	7.0	7.90	6.50	6.59	6.97
10	2011/03/09	9.9	7.3	7.58	4.88	4.89	5.66
Average of each component				8.32	6.32	6.68	
Average of S-components						6.50	
Overall average							7.06

found by A. Newman, using a different approach (Figure 5.4) [*pers. comm., 5/3/2011*]. Our cumulative energy shows that the extrapolated energy into the low frequencies is around 10% - 20% on average, and about 90% of the energy is measured below 0.1 Hz (Figure 5.2).

5.3.2 Sumatra 2004

The Sumatra 2004 M_w *9.1* earthquake was the first great earthquake to test the GSN, and also caused a devastating tsunami. The earthquake lasted for 450 seconds, almost three times as long as the Tohoku-Oki event, and was the longest rupture ever recorded, covering nearly 1300 km along strike, with a variable slip distribution from the epicenter in the south to the northern tip of rupture (Figure 5.5) [*Ammon et al,* 2005; *Lay et al.,* 2005]. The slip may have had a large slow component, which was probably responsible for the large tsunami [*Bilham*, 2005; *Banerjee et al.*, 2005].

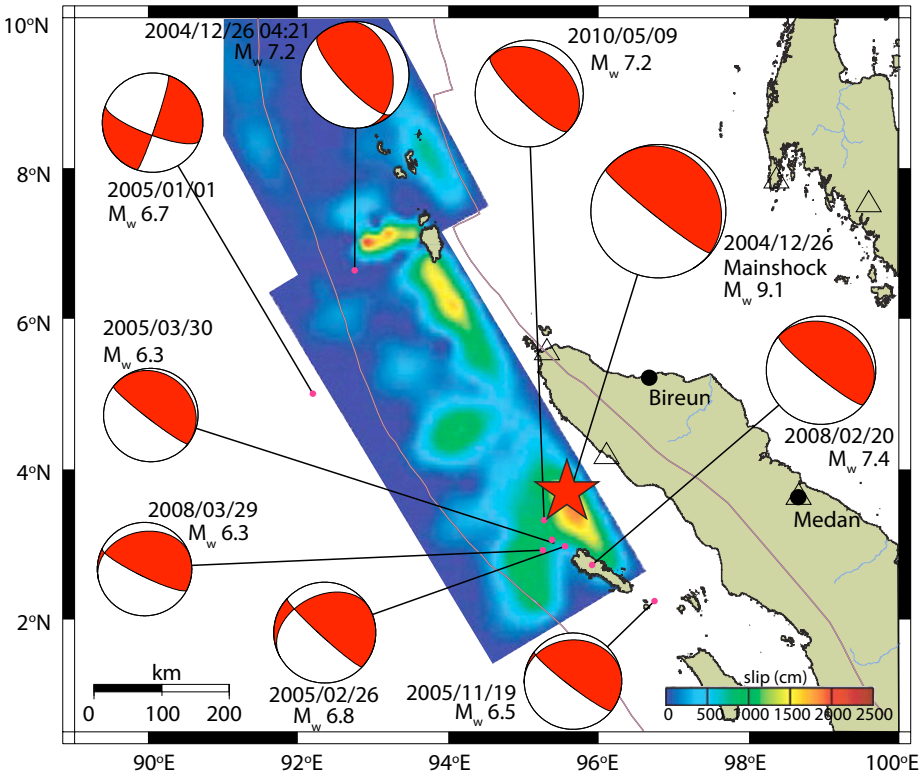

Figure 5.5 Map of Sumatra 2004 rupture area and candidate eGf events. Rupture slip plane from *Ammon et al,* [2005]. Focal mechanisms and locations from gCMT catalog.

Even at teleseismic distances, the Sumatra 2004 earthquake, with its unusually long rupture plane does not resemble a point source. However, *Lay et al.*, [2005] showed that most of the slip, up to 20 m, with an average of 5 m, occurred in the first 230 seconds, on the southern most 420 km fault plane, as seen in Figure 5.5. Since we use the first 270 seconds of *P* and *S* arrivals, we are capturing this initial intense rupture, and we are able to model the source spectrum from single eGf deconvolution, due to their location near the patches of high slip. This part of the rupture was along a plane approximately 420km x 240 km, with a strike of about 330°, and average slip of 7m, compared to much smaller (5 m, and <2 m) average slip on the northern segments. There were four events with similar mechanism to the mainshock, occurring very near the location of high slip. Figure 5.6 shows the waveform similarity of the eGf events, and the long duration of the mainshock. While the four eGf events have fairly consistent, impulsive arrivals, the mainshock again has a slower start before reaching large amplitudes (Figure 5.7).

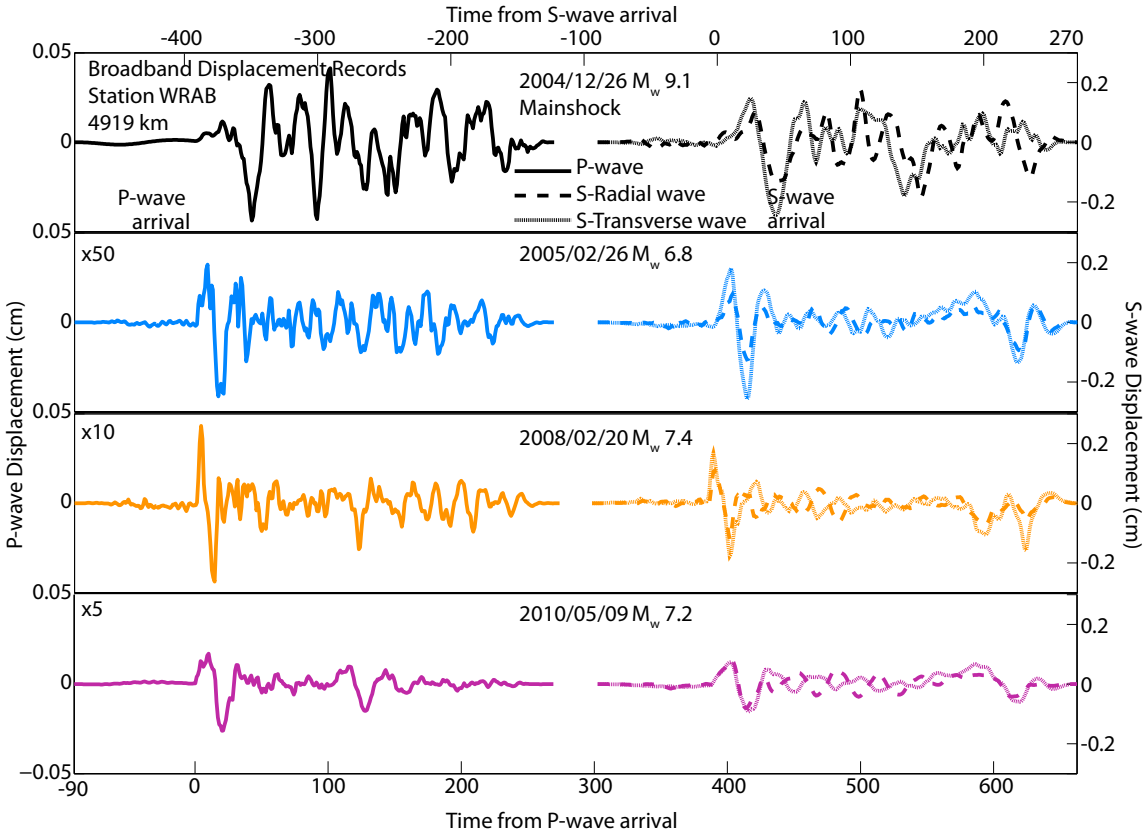

Figure 5.6 Broadband displacement waveforms from Sumatra 2004 mainshock (top panel) and 4 candidate eGf events, recorded at station WRAB with a distance of 4919 km. Left seismograms are *P*-wave vertical recordings, right are the *S*-wave radial and transverse components, each windowed from 90 seconds before the first arrival to 270 seconds afterwards, and tapered. The eGf recordings are scaled by the factor shown in upper left corner of each panel.

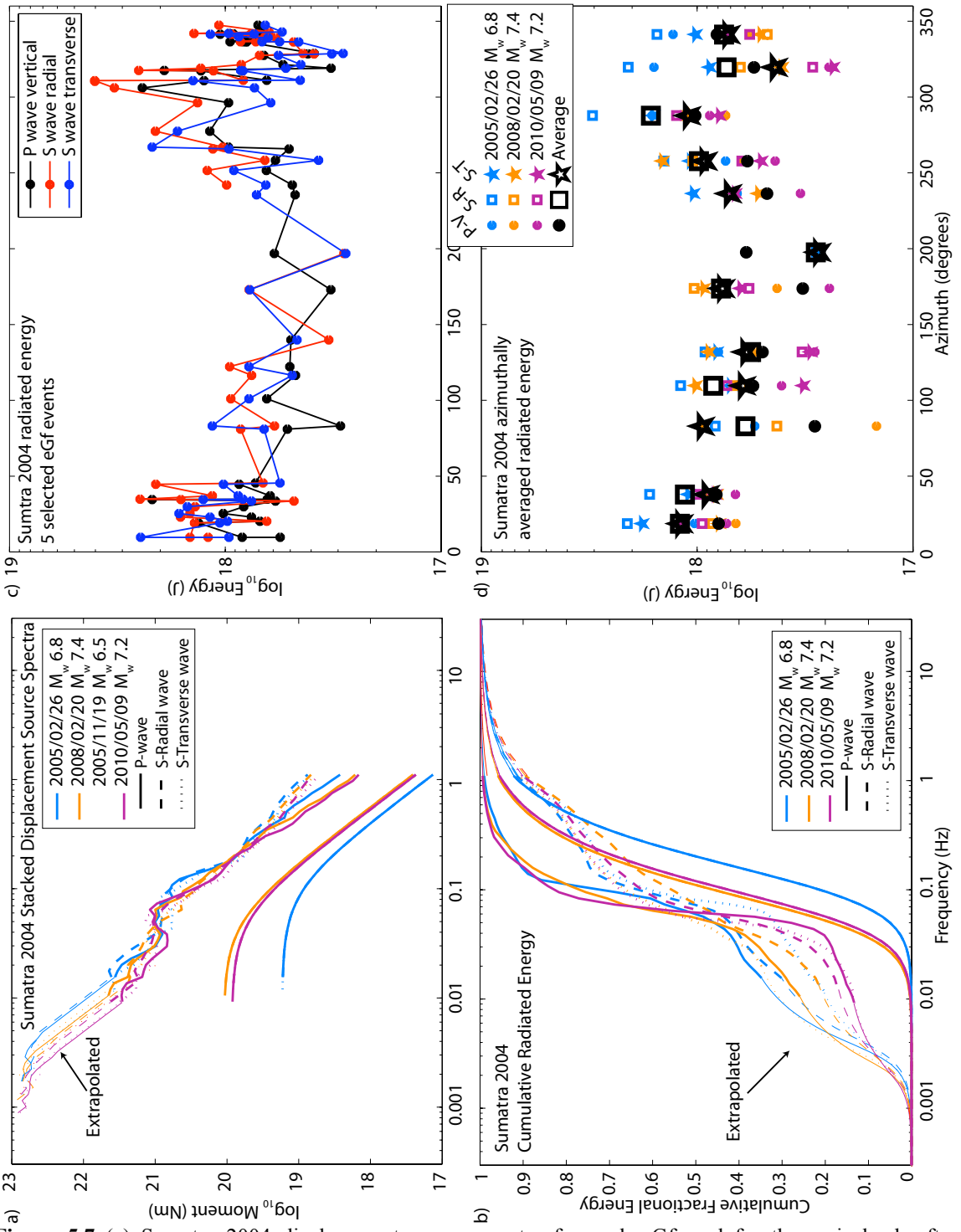

Figure 5.7 (a) Sumatra 2004 displacement source spectra for each eGf, and for the mainshock after deconvolving the different eGf events, stacked over all stations. (b) Cumulative fractional energy of the mainshock corrected individually by each eGf, and stacked over all stations. Light lines in the low frequencies of the mainshock in (a) and (b) show the missing, extrapolated energy, which amounts to ~10% - 30% on average. (c), (d) Mainshock radiated energy as a function of station azimuth. (c) Log_{10} average over all eGfs, for each component, shown at all stations. (d) Energy shown as corrected from each eGf event and each component, azimuthally weighted into 30-degree bins. Average of each bin shown in black, used for the final reported energy estimate. Different components shown with different symbol shapes.

Table 5.2 Radiated seismic energy of Sumatra 2004, corrected by each eGf, with given eGf moment and magnitude. The $\log_{10}$ average shown in right column is weighted azimuthally.

Catalog Information				Radiated Energy (Joules, x 10^{17})			
#	Date	M_o (Nm, x10^{19})	M_w	P-Vert.	S-Radial	S-Trans.	Average
2	2005/02/26	1.7	6.8	8.93	12.91	9.37	10.26
4	2005/11/19	0.62	6.5	6.52	9.48	6.67	7.45
5	2008/02/20	11	7.4	5.08	7.37	8.02	6.70
7	2010/05/09	8.5	7.2	4.46	6.38	5.56	5.41
Average of each component				6.03	8.71	7.27	
Average of S-components						7.96	
Overall average							**7.25**

We find the energy of the Sumatra 2004 event to be 7.19 x10^{17} J, a scaled energy of 1.12x10^{-5}, and apparent stress of 0.43 MPa, slightly less than that of Tohoku-Oki 2011 (Table 5.2). The *S* components of the corrected mainshock have more energy in the higher frequencies than the *P*-wave vertical, which can also be seen in the cumulative energy (Figure 5.7b). It is possible that the 360s window we use around the *S*-wave arrival is actually capturing other *P* arrivals due to the long rupture length, which would affect the frequency content. About 80% of the mainshock energy is below 0.1Hz.

The Sumatra 2004 event also shows strong directivity in radiated energy, which is expected due to the long and narrow fault plane, which ruptured primarily to the north. This directivity is consistent with that found for Rayleigh wave amplitudes, with a large peak towards ~300^o, a smaller peak near 20^o, and a minimum around 135^o [*Ammon et al.,* 2005]. While *Kanamori* [2006] states that there is little directivity effect in his estimation of radiated energy from the Sumatra 2004 earthquake, the stations that he uses show similar energy results. By including more stations, we can better resolve a clear pattern of directivity.

5.3.3 Maule 2010

The 2010 Maule M_w *8.8* earthquake occurred along the Chilean subduction zone, just north of the 1960 Chilean M_w *9.5* megathrust [*Moreno*, 2010]. The rupture occurred on a plane about 150 km along dip, up to the thrust interface, by 400 km along strike, in NNW

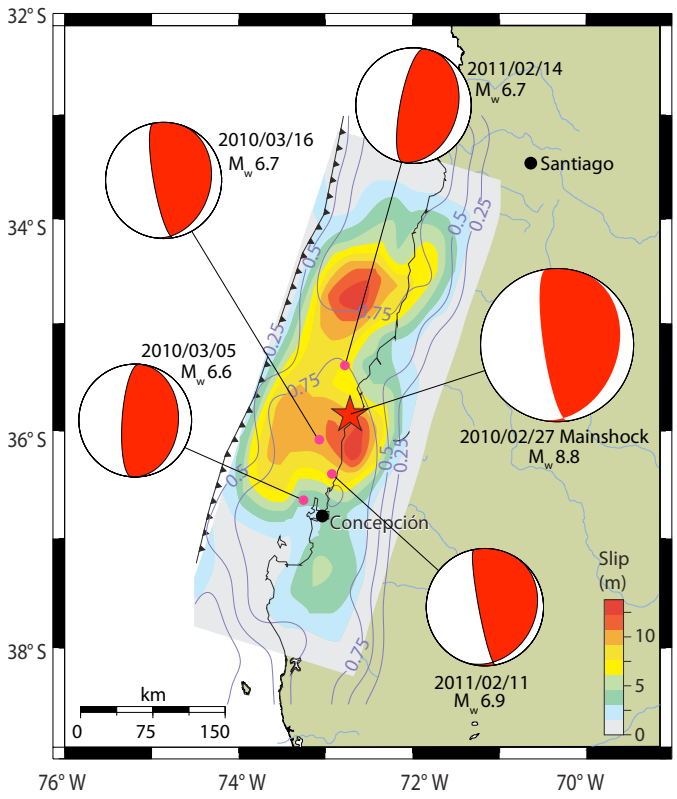

Figure 5.8 Map of Maule 2010 rupture area and candidate eGf events. Rupture slip plane from *Hayes* [2010] USGS Teleseismic model, as displayed by *Moreno et* al [2010]. Focal mechanisms and locations from gCMT catalog.

direction, and lasted 150 seconds (Figure 5.8) [*Hayes,* 2010]. This event caused a tsunami locally as well as globally, but not nearly on the same scale as either the Sumatra 2004 or Tohoku-Oki 2011 tsunami. We identify four empirical Green's functions near the area of high slip, and discard one potential eGf due to its location far from the epicenter. The Maule 2010 mainshock shows somewhat more impulsive arrivals, as compared to the Sumatra 2004 and Tohoku-Oki 2011 earthquakes, yet the eGf events are even more impulsive (Figure 5.9).

The estimated radiated energy is 1.86×10^{17} Joules, $E_R/M_o = 1.03 \times 10^{-5}$ and $\tau_a = 0.40$ MPa, averaged over all four eGf events and three components (Table 5.3). The

Table 5.3 Radiated seismic energy of Maule 2010, corrected by each eGf, with given eGf moment and magnitude. The $\log_{10}$ average shown in right column is weighted azimuthally.

	Catalog Information			Radiated Energy (Joules, x 10^{17})			
#	Date	M_o (Nm, x10^{19})	M_w	P-Vert.	S-Radial	S-Trans.	Average
1	2010/03/05	0.73	6.6	1.39	0.92	1.12	1.13
2	2010/03/16	1.20	6.7	2.28	1.80	1.77	1.93
4	2011/02/11	5.30	6.9	3.92	2.48	2.06	2.72
5	2011/02/14	1.70	6.7	2.92	1.78	1.57	2.01
Average of each component				2.45	1.65	1.59	
Average of S-components						1.62	
Overall average							**1.86**

mainshock source spectra contains a coherent bump near frequencies of 0.1 Hz that we interpret as a source effect. Again, about 20% of the total energy is from extrapolation into the low frequencies, below 100 seconds.

Figure 5.10 (a) shows the similarity of the mainshock spectra, when corrected with each different eGf event. With the exception of a small deviation near 0.1 Hz, the spectra are remarkably similar. The three components of motion show a similar pattern as a function of azimuth, with a minimum of radiated energy towards the southwest, at about 250^{o}, but the azimuthal variation is not as strong as that for the two larger events (Figure 5.10 c and d).

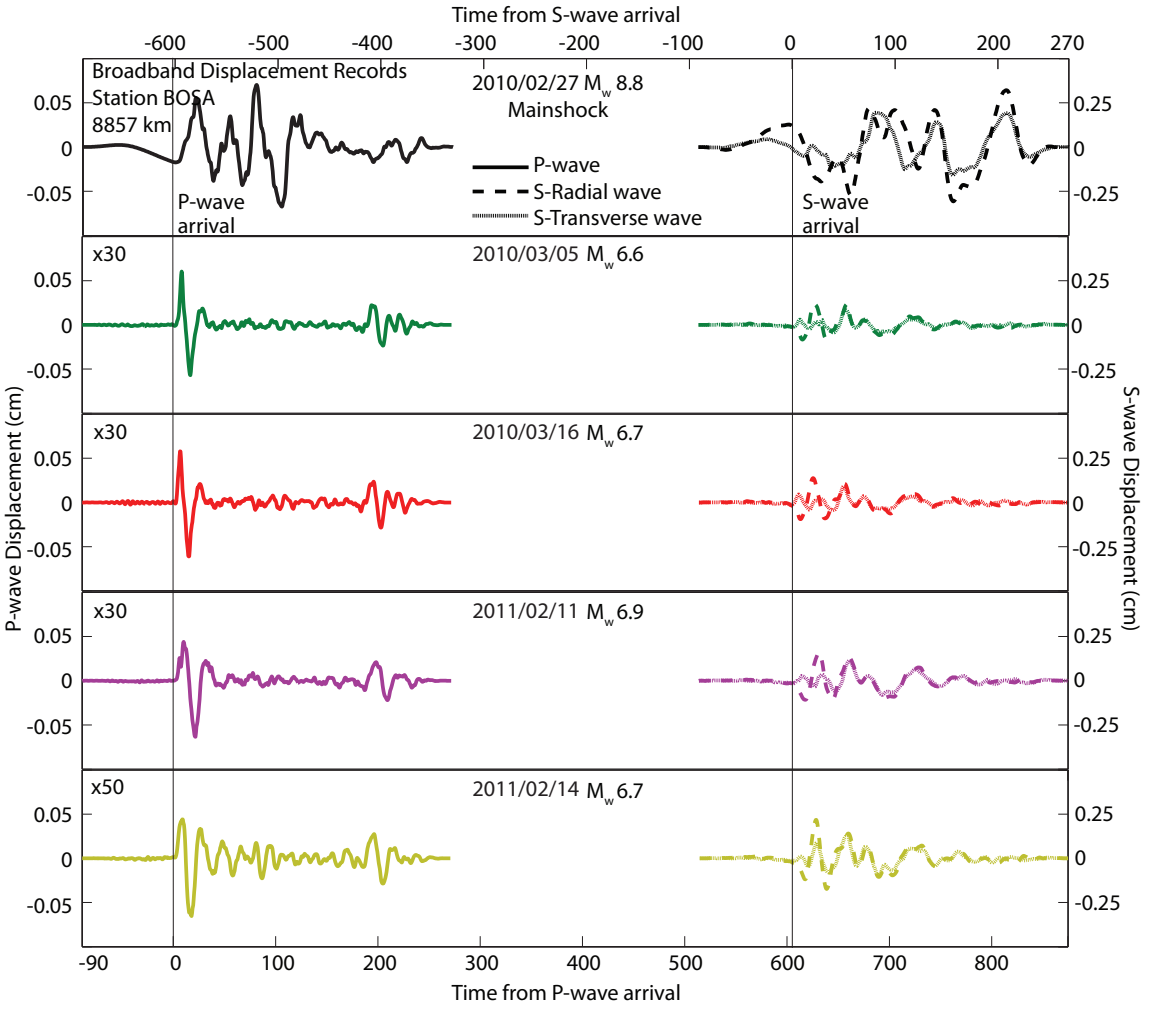

Figure 5.9 Broadband displacement waveforms from Maule 2010 mainshock (top panel) and 4 candidate eGf events, recorded at station BOSA with a distance of 8857 km. Left seismograms are *P*-wave vertical recordings, right are the *S*-wave radial and transverse components, each windowed from 90 seconds before the first arrival to 270 seconds afterwards, and tapered. The eGf recordings are scaled by the factor shown in upper left corner of each panel.

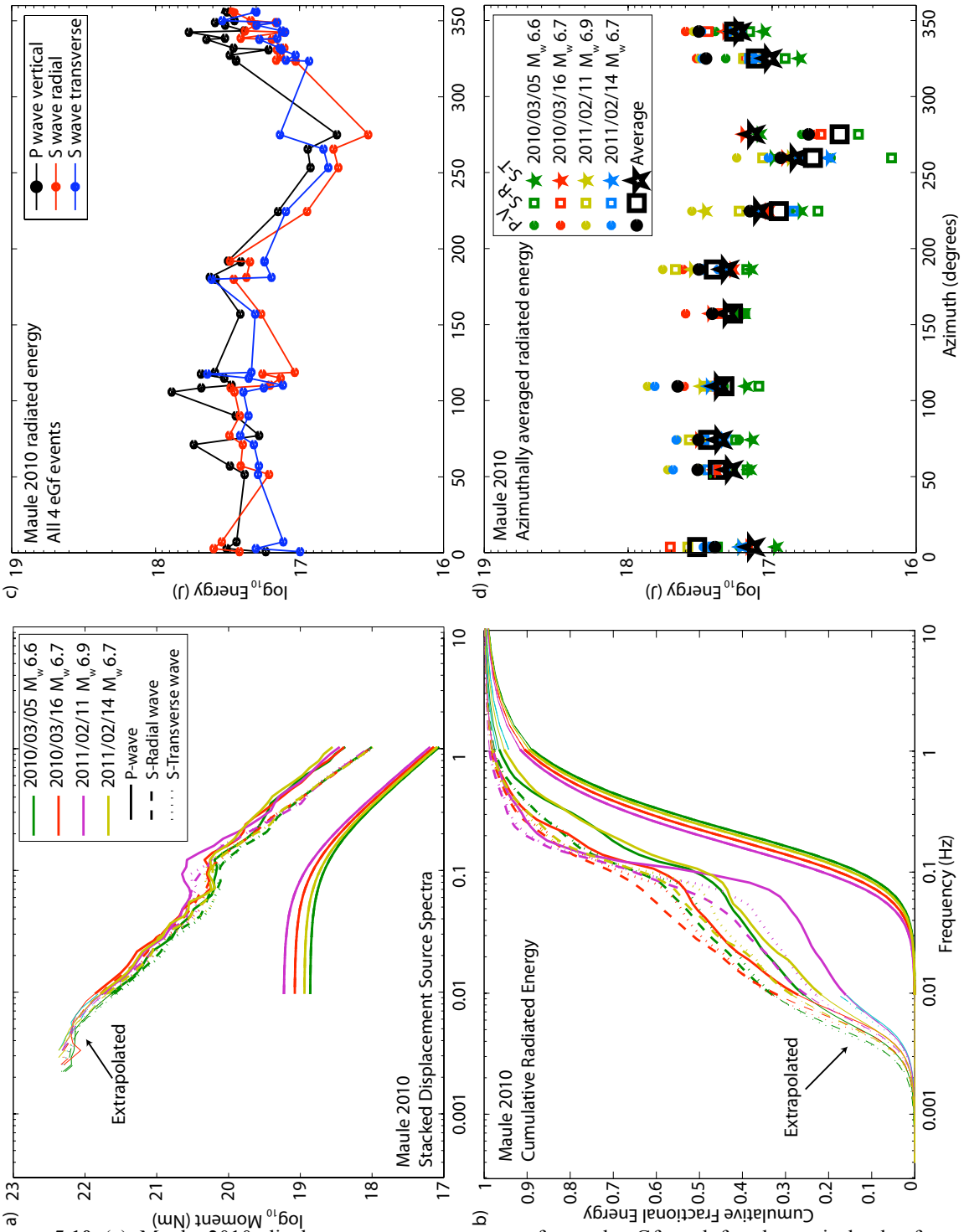

Figure 5.10 (a) Maule 2010 displacement source spectra for each eGf, and for the mainshock after deconvolving the different eGf events, stacked over all stations. (b) Cumulative fractional energy of the mainshock corrected individually by each eGf, and stacked over all stations. Light lines in the low frequencies of the mainshock in (a) and (b) show the missing, extrapolated energy, which amounts to ~10% - 30% on average. (c), (d) Mainshock radiated energy as a function of station azimuth. (c) Log_{10} average over all eGfs, for each component, shown at all stations. (d) Energy shown as corrected from each eGf event and each component, azimuthally weighted into 30-degree bins. Average of each bin shown in black, used for the final reported energy estimate. Different components shown with different symbol shapes.

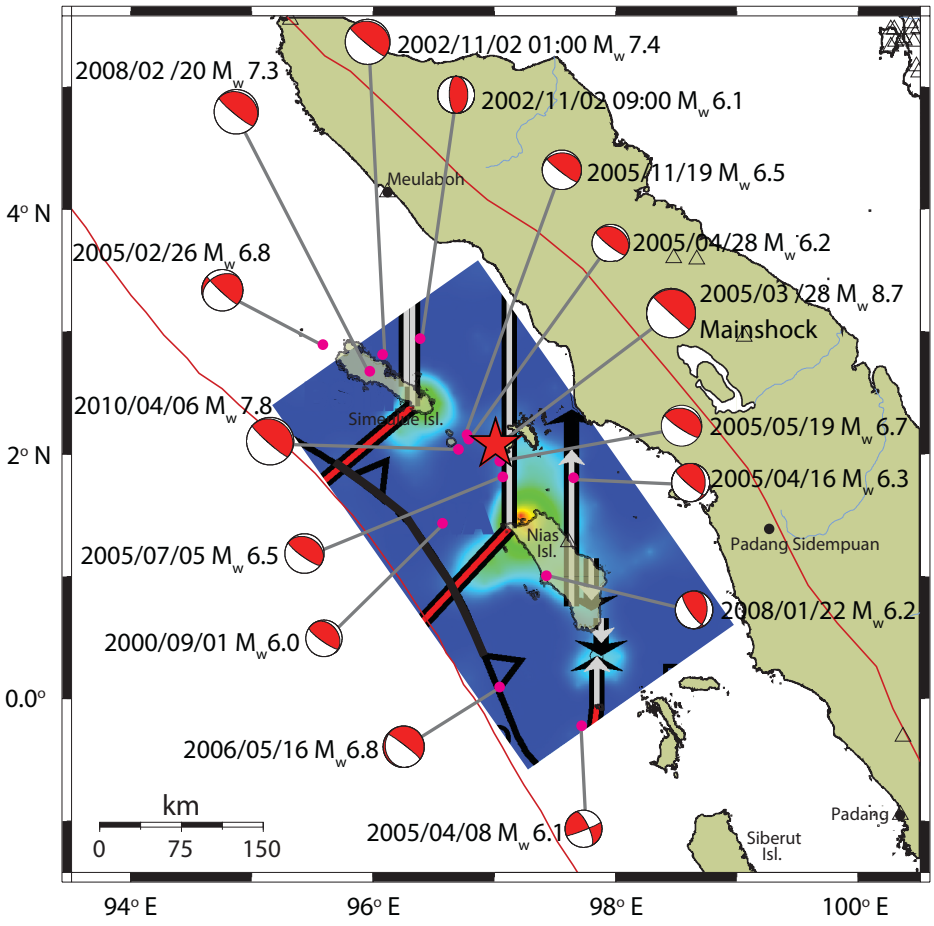

Figure 5.11 Map of Nias 2005 2010 rupture area and candidate eGf events. Rupture slip plane from *Konca et al.* [2007]. Focal mechanisms and locations from gCMT catalog.

5.3.4 Nias 2005

The Nias 2005 M_w *8.7* earthquake occurred near Nias Island, just offshore of Sumatra, Indonesia, south of the Sumatra 2004 M_w *9.1*, along the Sunda trench (Figure 5.11). The rupture plane is about 150 km wide and 300 km along strike, to the NNW. The event lasted about 120 – 150 seconds, and ruptured bilaterally, to the north and south, in two distinct patches [*Konca et al.,* 2007]. The rupture did not come as close to the trench as the Sumatra 2004 event, however, and generated a much smaller, local tsunami [*Dean et al.,* 2010]. In this case, we consider 14 different eGf events, but discard most of them to use five earthquakes, occurring both before and after the mainshock. The five chosen eGf events show very similar waveforms, as does the mainshock, for both the *P* and *S* components (Figure 5.12).

The final estimate of radiated energy, for all eGf events and azimuthally weighted, is 2.19×10^{17} Joules, with a scaled energy of 2.09×10^{-5} and apparent stress of 0.81 MPa (Table 5.4). On average, less than 20% of the energy is extrapolated into the low frequencies, and in the cumulative fractional energy, the mainshock spectra look fairly Brune-like (Figure 5.13, a and b). The azimuthal dependence of radiated energy is not as strong as that of some of the other great events, but we do see a local maximum at about 330° along strike to the north, and another near 150°, along strike to the south (Figure 5.13, c and d).

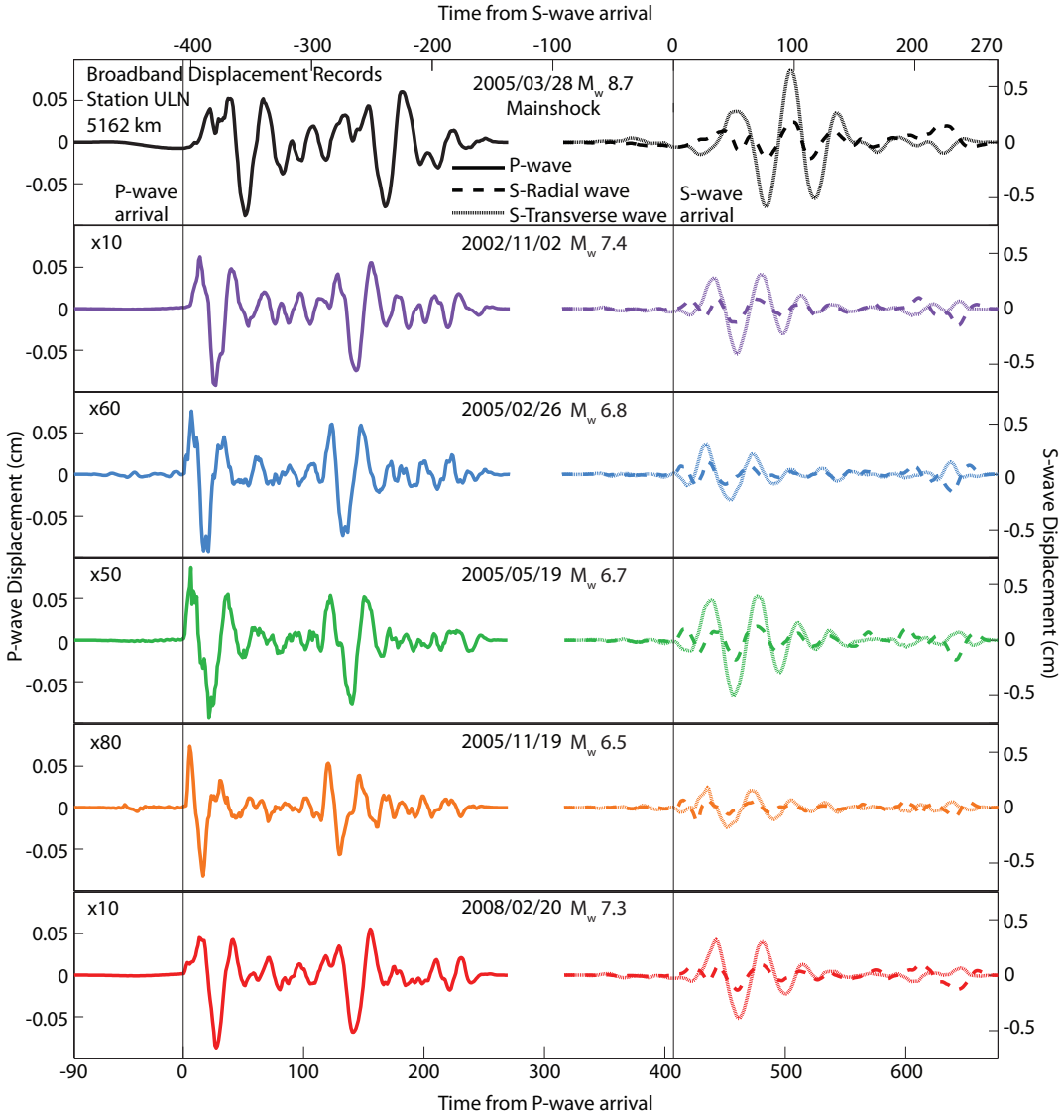

Figure 5.12 Broadband displacement waveforms from Nias 2005 mainshock (top panel) and 4 candidate eGf events, recorded at station ULN with a distance of 5162 km. Left seismograms are *P*-wave vertical recordings, right are the *S*-wave radial and transverse components, each windowed from 90 seconds before the first arrival to 270 seconds afterwards, and tapered. The eGf recordings are scaled by the factor shown in upper left corner of each panel. The *PP* arrivals are clear at this station because of the closer location.

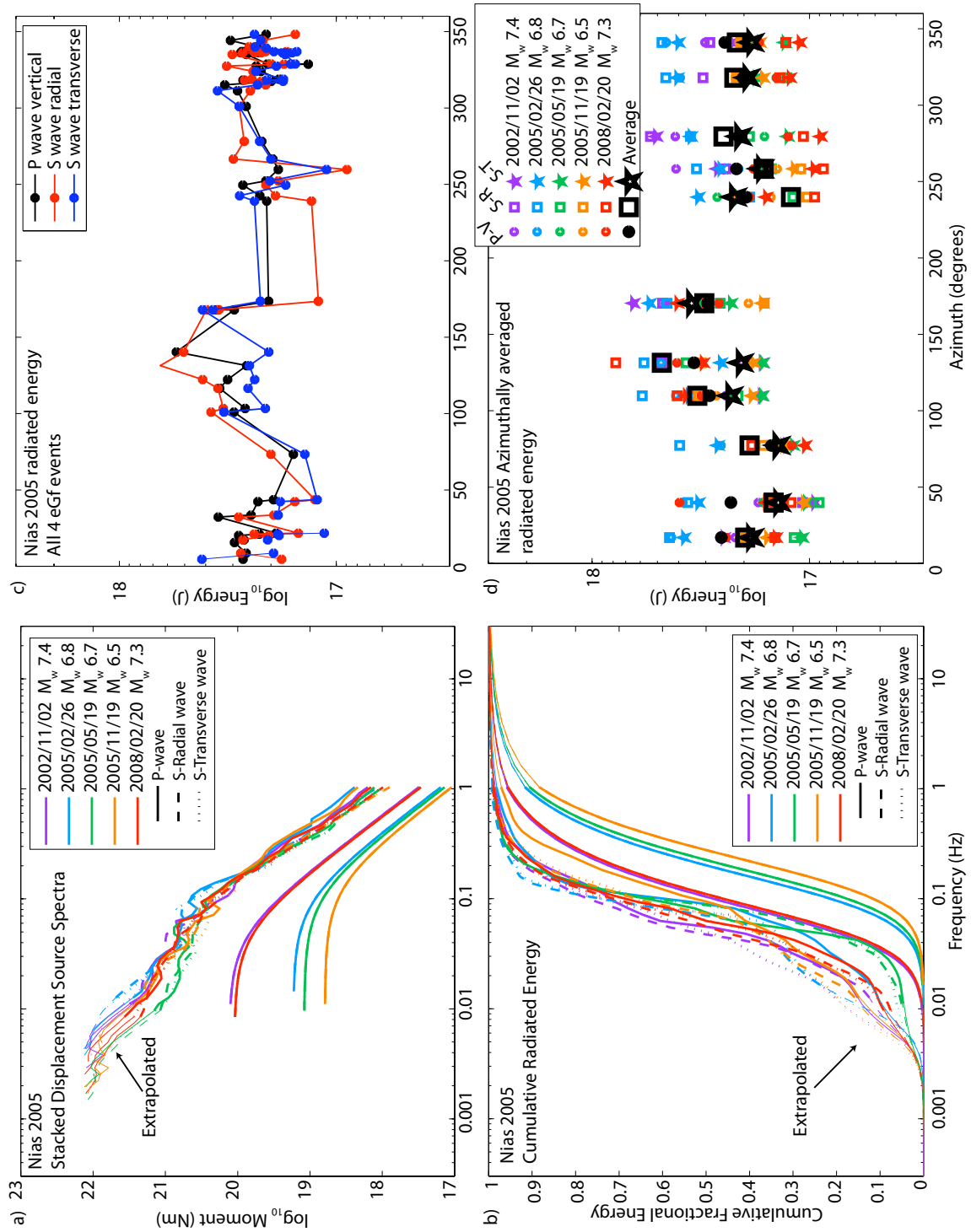

Figure 5.13 (a) Nias 2005 displacement source spectra for each eGf, and for the mainshock after deconvolving the different eGf events, stacked over all stations. (b) Cumulative fractional energy of the mainshock corrected individually by each eGf, and stacked over all stations. Light lines in the low frequencies of the mainshock in (a) and (b) show the missing, extrapolated energy, which amounts to ~10% - 20% on average. (c), (d) Mainshock radiated energy as a function of station azimuth. (c) Log_{10} average over all eGfs, for each component, shown at all stations. (d) Energy shown as corrected from each eGf event and each component, azimuthally weighted into 30-degree bins. Average of each bin shown in black, used for the final reported energy estimate. Different components shown with different symbol shapes.

Table 5.4 Radiated seismic energy of Nias 2005, corrected by each eGf, with given eGf moment and magnitude. The $\log_{10}$ average shown in right column is weighted azimuthally.

	Catalog Information			Radiated Energy (Joules, x 10^{17})			
#	Date	M_o (Nm, x10^{19})	M_w	P-Vert.	S-Radial	S-Trans.	Average
2	2002/11/02 01:26:10	13	7.4	2.56	2.69	2.26	2.49
4	2005/02/26	1.7	6.8	3.28	4.08	3.46	3.59
8	2005/05/19	1.2	6.7	2.07	1.62	1.52	1.72
10	2005/11/19	0.62	6.5	1.98	1.85	1.58	1.80
13	2008/02/20	11	7.3	2.15	1.77	1.63	1.84
Average of each component				2.36	2.25	1.98	
Average of S-components						2.11	
Overall average							**2.19**

5.3.5 Bengkulu 2007

The Bengkulu 2007 M_w *8.5* event occurred south of the Nias 2005 earthquake along the trench, and just off shore of the town Bengkulu. The rupture occurred in two distinct patches along strike, over 100 seconds (Figure 5.14) [*Konca et al.,* 2008]. The rupture plane was 100 km x 200 km, striking about 330^o, similar to the Nias 2005 and Sumatra 2004 events. For this mainshock, we considered 12 potential empirical Green's function events, ranging from M_w *6.3* to M_w *7.9,* but choose to use four, and discard those with different mechanism or magnitude too large or small (*see discussion below*). The four eGf events and the mainshock have very similar wave forms, as shown at station MDJ (Figure 5.15), comparable to the Nias mainshock and eGf events.

The corrected source spectra show a large hole at about 100 seconds (Figure 5.16a). This is likely due to the rupture occurring in two distinct bursts, one represented by a spectrum with a higher corner frequency, and one with a lower corner frequency, so that the interference of the two yields the hole we observe. This peculiar feature shows up in the cumulative fractional energy in Figure 5.16b, so that the amount extrapolated is very low, less than 10% on average.

The overall averaged radiated energy of the Bengkulu event is 1.33x10^{17} J, with E_R/M_o = 1.98x10^{-5}, and τ_a = 0.77 MPa (Table 5.5). The azimuthal distribution of energy is not as well resolved as for the other great events, but there is a slight peak to the north,

between 300° and 50°. We also note that the *P* wave spectra show consistently higher energy values than the *S* waves (Figure 5.16 c and c).

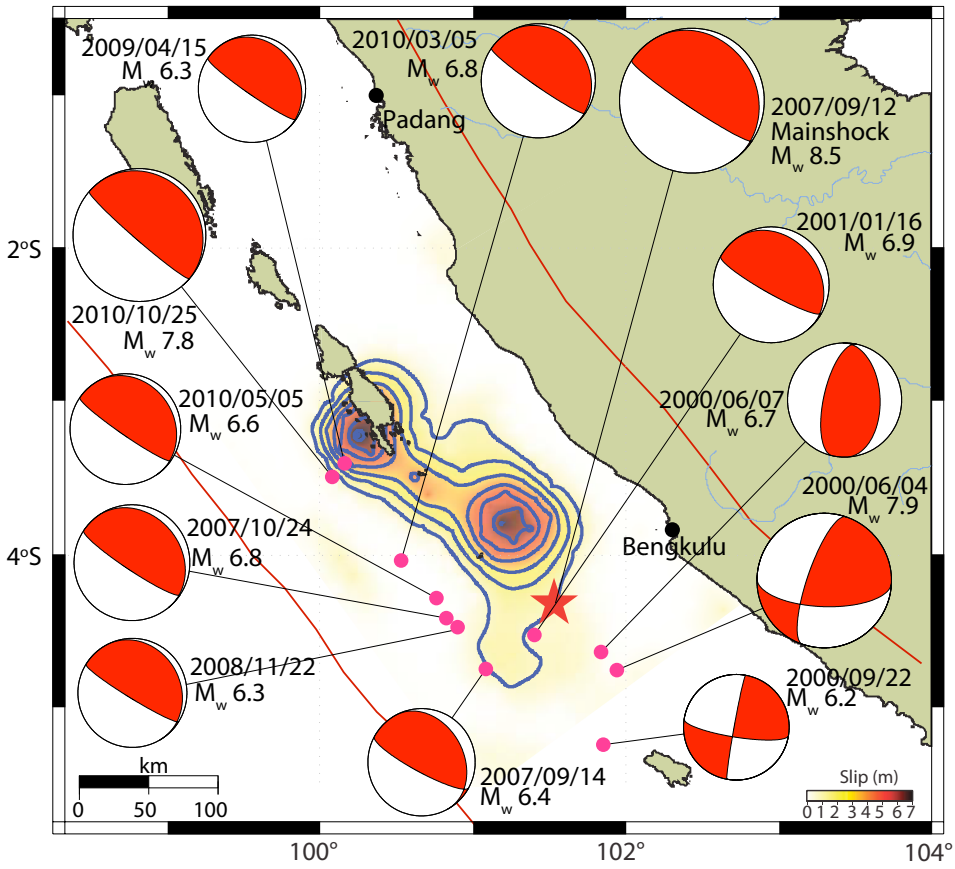

Figure 5.14 Map of Bengkulu 2007 rupture area and candidate eGf events. Rupture slip plane from *Konca et al.* [2008]. Focal mechanisms and locations from gCMT catalog.

Table 5.5 Radiated seismic energy of Bengkulu 2007, corrected by each eGf, with given eGf moment and magnitude. The $\log_{10}$ average shown in right column is weighted azimuthally.

	Catalog Information			**Radiated Energy (Joules, x 10^{17})**			
#	Date	M_o (Nm, x10^{19})	M_w	P-Vert.	S-Radial	S-Trans.	Average
4	2001/01/16	2.0	6.8	1.66	1.05	1.28	1.31
6	2007/10/24	2.3	6.9	1.56	0.88	0.73	1.00
9	2010/03/05	1.6	6.8	2.00	1.45	1.12	1.48
10	2010/05/05	0.8	6.6	2.20	1.41	1.32	1.60
Average of each component				1.84	1.17	1.08	
Average of S-components						1.13	
Overall average							**1.33**

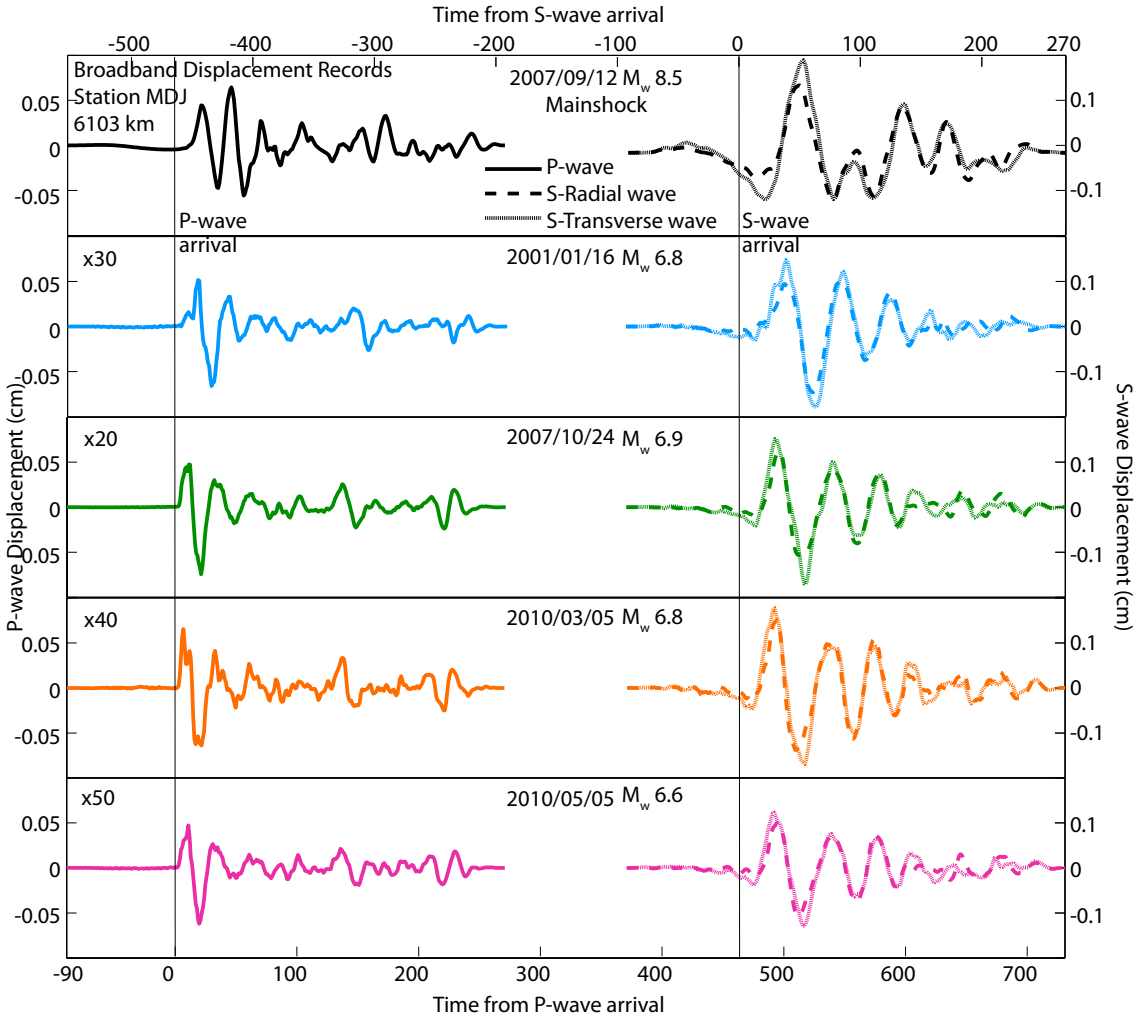

Figure 5.15 Broadband displacement waveforms from Bengkulu 2007 mainshock (top panel) and 4 considered eGf events, recorded at station MDJ with a distance of 6103 km. Left seismograms are *P*-wave vertical recordings, right are the *S*-wave radial and transverse components, each windowed from 90 seconds before the first arrival to 270 seconds afterwards, and tapered. The eGf recordings are scaled by the factor shown in upper left corner of each panel.

5.4 Constant Scaled Energy and Apparent Stress

Overall, we find that the radiated energy of the five great earthquakes to be in the expected range for their size. The scaled energy of all five events is between ~1 – 2 x10^{-5}, corresponding to an apparent stress of 0.4 – 0.8 MPa, consistent with the global distribution of scaled energy.

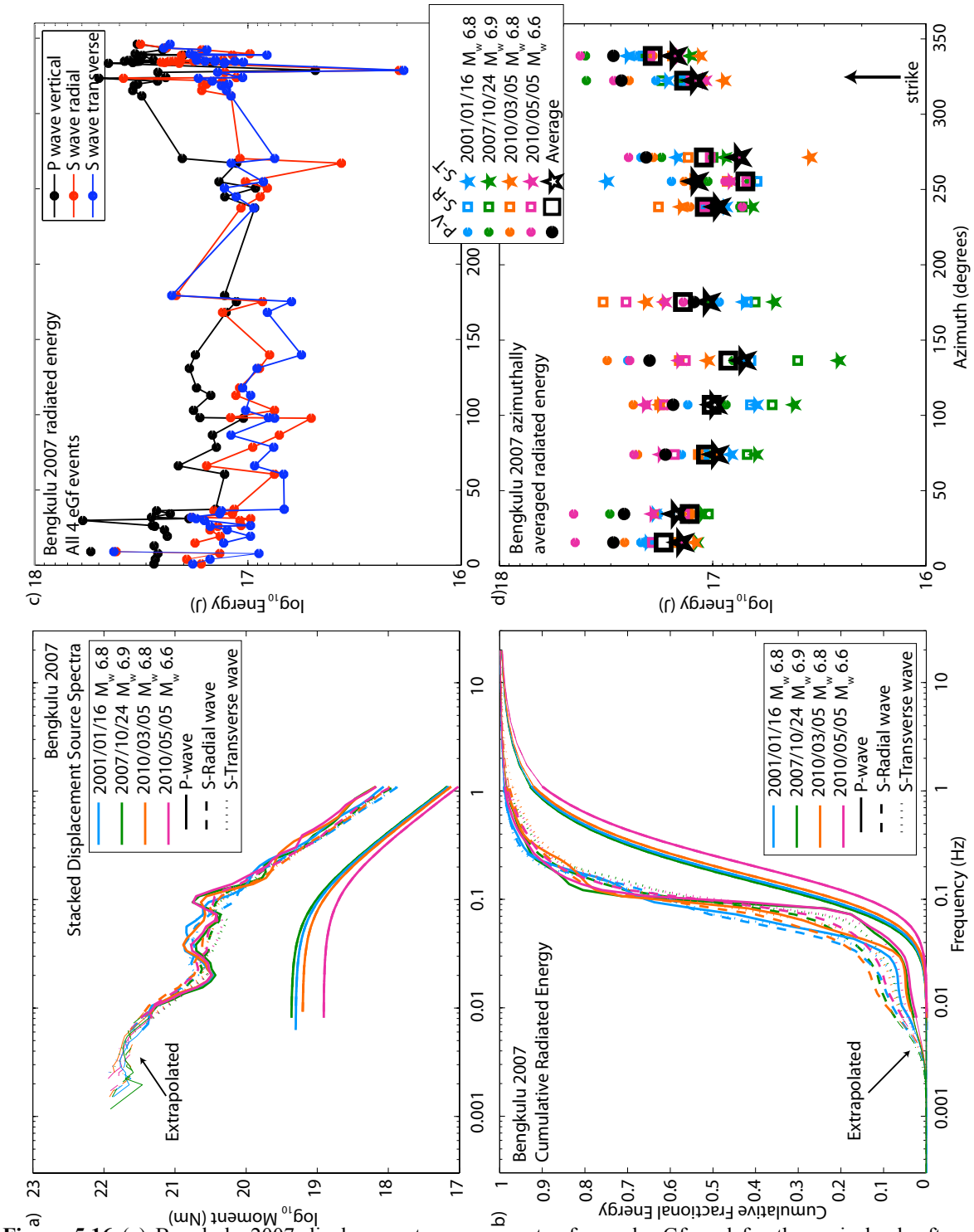

Figure 5.16 (a) Bengkulu 2007 displacement source spectra for each eGf, and for the mainshock after deconvolving the different eGf events, stacked over all stations. (b) Cumulative fractional energy of the mainshock corrected individually by each eGf, and stacked over all stations. Light lines in the low frequencies of the mainshock in (a) and (b) show the missing, extrapolated energy, which amounts to less than 10%. (c), (d) Mainshock radiated energy as a function of station azimuth. (c) Log_{10} average over all eGfs, for each component, shown at all stations. (d) Energy shown as corrected from each eGf event and each component, azimuthally weighted into 30-degree bins. Average of each bin shown in black, used for the final reported energy estimate. Different components shown with different symbol shapes.

We compare our results to other studies [*Convers and Newman*, 2011; *Kanamori*, 2006; *H. Kanamori*, *pers. comm.*, 2011; *NEIC reported radiated energy*, http://earthquake.usgs.gov; *Boatwright and Choy*, 1986] in Table 5.6. These studies make attenuation, source, and station corrections to teleseismic *P* waves to estimate source spectra and radiated energy. Results from this study compare very closely with those of Newman and Kanamori. With the exception of the Tohoku-Oki 2011 event, the USGS estimates are systematically much lower than the others, potentially due to an abbreviated time window used in the waveforms. Although we use the same value of ρ as in *Convers and Newman* [2011], there are still sources of uncertainty between the different methods, such as how the different station energies are averaged together, that could account for the small differences between the studies. Our new, teleseismic eGf deconvolution for estimating source spectra yields radiated energy results in agreement with other studies, validating this method, and implying that it can be used to estimate robust source spectra and hence other source parameters. An inherent advantage of eGf techniques is that specific source and attenuation information is not required, and the result is only dependent on the eGf assumptions. We also show that *S* waves, in addition to *P* waves, can be used in teleseismic energy calculation, which greatly increases the number of records that can be analyzed.

Table 5.6 Radiated energy for all five great earthquakes, compared to estimates from Andrew Newman[1,2], Hiroo Kanamori[3,4] and the USGS[5]. Results from this study are fairly consistent with those of Newman and Kanamori; USGS estimates tend to be lower, perhaps due to the short window length used in the analysis. All events have scaled energy, E_R/M_o near $1 - 2 \times 10^{-5}$, corresponding to apparent stresses τa between 0.4 and 0.8 MPa, very consistent with global earthquakes over a large range of magnitudes.

	Radiated Energy, E_R (Joules x10^{17})				**E_R/M_o**	**τ_a**
Event	Newman	Kanamori	USGS[5]	This study	(x10^{-5})	(MPa)
Tohoku-Oki 2011	4.2[1]	4.3[3]	5.1	7.06	1.57	0.61
Sumatra 2004	8.2[2]	3.0[4]	1.1	7.25	1.12	0.43
Maule 2010	2.6[2]	1.7[3]	0.47	1.86	1.03	0.40
Nias 2005	1.1[2]	0.83[4]	0.37	2.19	2.09	0.81
Benkulu 2007	0.69[2]	0.38[3]	0.26	1.33	1.98	0.77

[1]http://geophysics.eas.gatech.edu/anewman/research/RTerg/2011/11031100/
[2]Convers, J. A., and A. V. Newman (2011), Global evaluation of large earthquake energy from 1997 through mid-2010, *J. Geophys. Res*.,116, B08304, doi:10.1029/2010JB007928.
[3]Kanamori, H. (2011) *pers. comm.* November 6, 2011
[4]Kanamori, H. (2006) The radiated energy of the 2004 Sumatra-Andaman earthquake, in *Earthquakes: radiated energy and the physics of faulting,* Geophysical Monograph Series, 170, 59-68, doi:10.1029/170GM10.
[5]As reported on http://earthquake.usgs.gov, following Boatwright, J. and G. Choy, Teleseismic estimates of the energy radiated by shallow earthquakes, *J. Geophys. Res., 91*, 2095-2112, 1986.

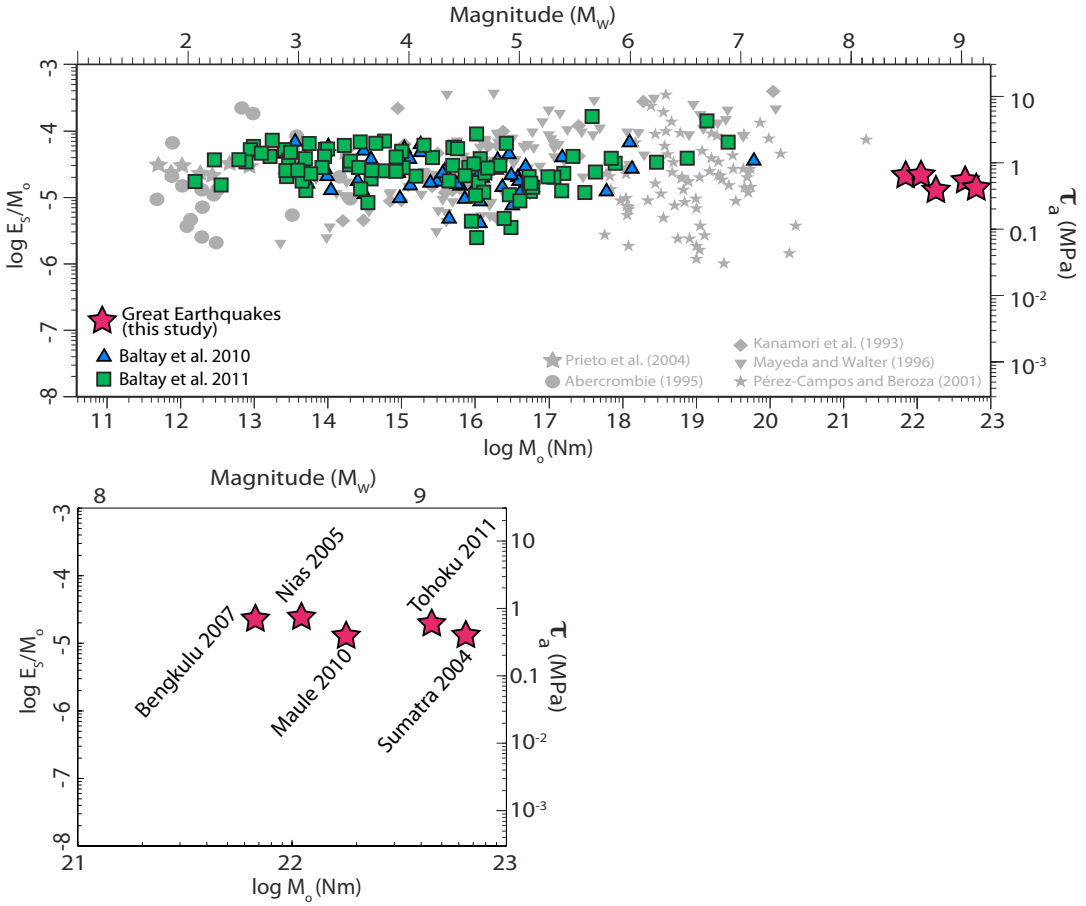

Figure 5.17 (Top) Scaled energy and apparent stress of the five great earthquakes (red stars) overlain on *Ide and Beroza* [2001] figure compiling many other studies. Also shown are the scaled energy results from *Baltay et al.* [2010] from the western US, and *Baltay et al.* [2011] from Honshu, Japan. Energy of the great earthquakes is consistent with that of other earthquakes, from ~M 2 to M 7. (Bottom) Close up of scaled energy and apparent stress of great earthquakes. Apparent stress is similar and between 0.4 and 0.8 MPa.

Convers and Newman [2011] study 342 global earthquakes with $M>6.5$, and find an average scaled energy, $E_R/M_o = 2.57\text{x}10^{-5}$ for the whole catalog, and $1.82\text{x}10^{-5}$ for thrust events, very consistent with the scaled energies found here for the five largest events.

We compare the scaled energies to previous studies of smaller earthquakes. Figure 5.17 (top) shows results of *Baltay et al.* [2010] and *Baltay et al.* [2011], who used a local empirical Green's function technique to find scaled energy of ~200 events in the western United States and eastern Honshu, Japan, ranging from magnitude ~2 to ~7. Inclusion of the five recent great earthquakes emphasizes the lack of dependence of scaled energy on moment, as all of the events show no systematic variation in apparent stress with magnitude.

5.5 Azimuthal Dependence of Radiated Energy

We investigate the patterns of azimuthally distributed radiated energy from the five great earthquakes. Because the eGf events are much smaller compared to the mainshocks, they themselves do not show much directivity. Hence, any directivity in the mainshock rupture is maintained in the deconvolved, corrected spectra, which we can then observe in the radiated energy pattern. We see the strongest azimuthal dependence and clearest trends with the largest events, Sumatra 2004 M_w *9.1* and Tohoku-Oki 2011 M_w *9.0*. While the other three events do show azimuthal variation of radiated energy, the patterns are not as well resolved. In all cases, although the initial waveforms are quite different, the *P* and *S* components show similar trends, which implies that the relative differences between the wave types is the same between mainshock and eGf events.

We model each event using Haskell line sources superimposed on one another to approximate the directivity patterns observed [*Haskell*, 1964]. In the simplest model, shown as a schematic in Figure 5.18, energy waves emitted from rupture propagating unilaterally along a linear fault will pile up in the direction of rupture. This directivity causes a higher amplitude in the observed source time function in the direction of propagation, and a lower amplitude in the opposite direction. Since energy is proportional to the squared amplitude, the energy should be greater in the rupture propagation direction as compared to the opposite direction. In this Haskell model, the strike, dip, length, moment, and rupture velocity are defined. By superimposing multiple Haskell models to represent

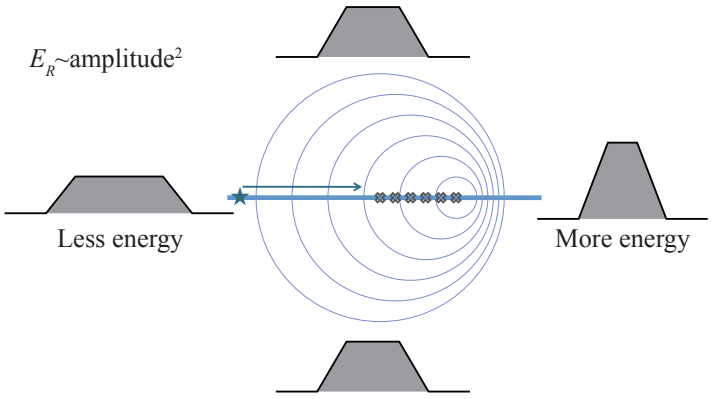

Figure 5.18 Haskell line source rupture directivity schematic. Rupture originates at the star on the left and propagates to the right, radiating waves, notated as x's, at each time point. Waves pile up towards the right, so that the source time function as measured at stations to the right has a shorter duration and higher amplitude, in contrast to the source time function observed in the anti-rupture direction. Because seismic energy is proportional to amplitude^2, higher values of radiated energy are measured in the rupture direction.

rupture propagation, we are able to capture the general features of the azimuthal variation of energy for each earthquake. The Haskell line models are shown in Figure 5.19 as the green lines.

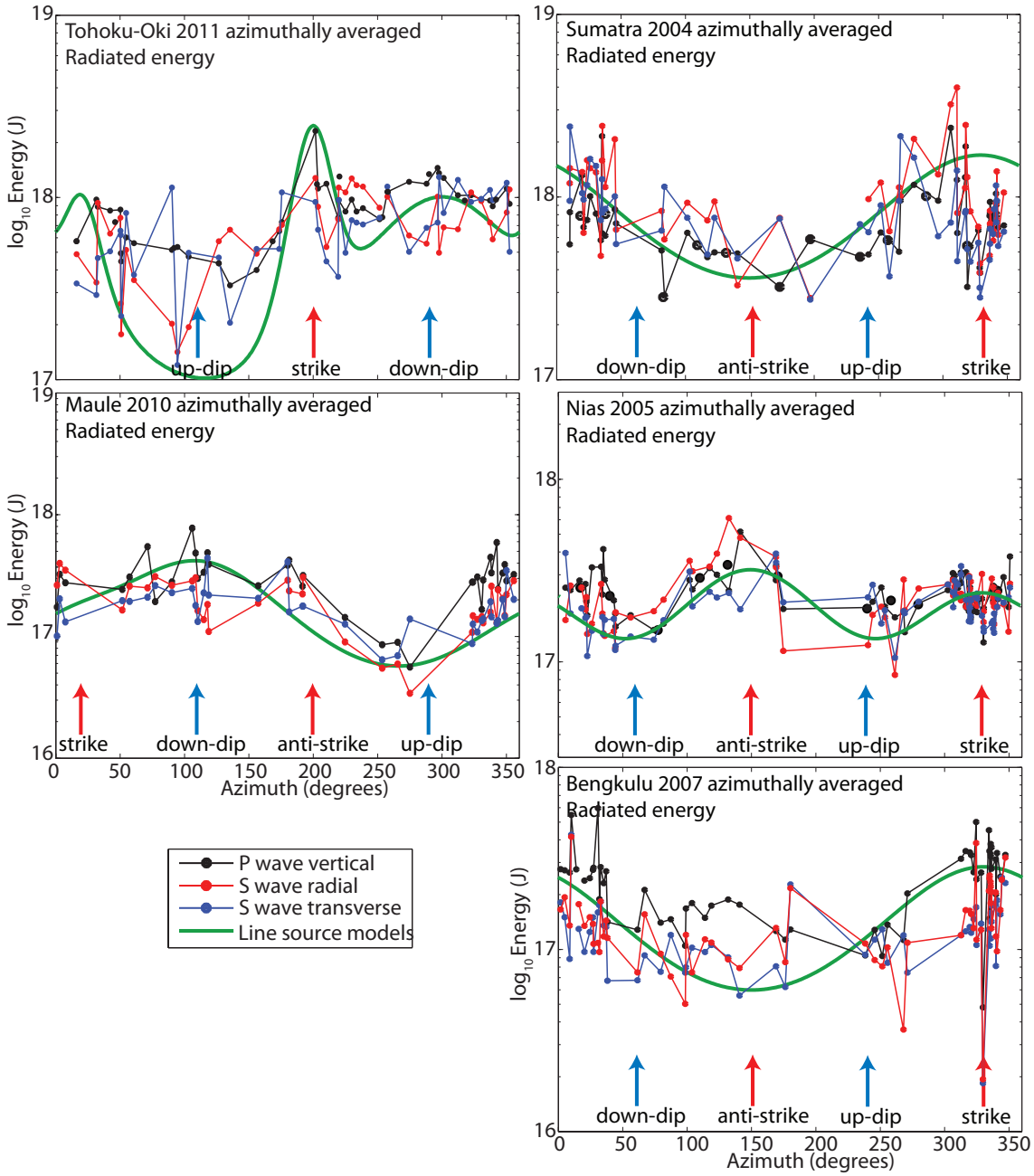

Figure 5.19 Azimuthal dependence of radiated seismic energy for all five great earthquakes, shown as the $\log_{10}$ mean overall eGf corrections, for each component. Green lines are the Haskell-type line sources. "Strike" indicates direction or rupture propagation, while "anti-strike" is along the strike in the opposite direction. "Trench" indicated the direction towards the trench, up dip.

In the Tohoku-Oki case, we see an energy peak in the strike direction at ~200^o, a small peak in the anti-strike direction (along strike in the opposite direction) at ~20^o, and a dip near ~100^o. Paired with the spatio-temporal slip inversion of *Ide et al.,* [2011], we interpret the peaks at 200^o and 20^o to be generated by high apparent velocity along and parallel to the trench causing surface rupture. The sag at 100^o is in the trench direction, which may imply that there is less high frequency radiation in that direction, and perhaps slow slip which could indicate tsunami generation. We model three Haskell-type line sources of the rupture. The main rupture with direction 300^o with 15^o dip is slow at 3.5 km/s with most of the moment (4.4x10^{22} Nm) and length 200 km, the approximate fault width. We model very fast surface rupture with apparent velocity 9.5 km/s along strike to the north at 20^o with moment 1x10^{20} Nm, and to the south at 200^o with a moment of 1x10^{21} Nm. These large apparent velocities correspond to the surface rupture seen by the slip model of *Ide et al*., [2011] and responsible for tsunami generation. While the amplitude of the up-dip minimum is not fit very well with the simple model, the line source captures the direction of the sag well. Overall, this 3-source Haskell model is able to explain the gross trends in the azimuthal energy data well for the Tohoku-Oki earthquake.

Because of the extended, 1300 km long rupture plane of the Sumatra 2004, and the rupture directivity that has been modeled, we would expect directivity along strike, to the north (*Ammon et al.,* 2005). We see this in the radiated energy, with a strong peak just west of the strike close to 330^o strike. In addition, there is a minimum of radiated energy in the opposite, anti-strike, direction, at ~150^o, strongly supporting the northward direction of rupture and energy propagation. In contrast to the Tohoku-Oki event, which occurred on a compact fault plane with rupture moving up- and down-dip, the Sumatra 2004 event started in the south and moved unilaterally to the north. In the energy estimation, we assume that we are only modeling the first part of the rupture, for 230 seconds. The rupture model shows two distinct, compact slip patches (Figure 5.5) [*Ammon et al.,* 2005]. We model these two patches as each having half of the 6.5x10^{22} Nm of moment, each with a length of 100 km, striking north at 330^o with a dip of 11^o, and rupture velocity of 2.5 km/s, consistent with rupture parameters found by *Ammon et al.,* (2005). These two sources add to the sinusoidal directivity pattern seen in Figure

5.19, and explain the overall pattern of radiated energy that we see for the Sumatra 2004 earthquake. The sag seen right at 300^o is not explained by the simple line models, however. Without better temporal resolution of the slip evolution we cannot capture the small rupture details, but this simple model have the same overall trend and amplitudes as the data.

The Maule 2010 M_w *8.8* earthquake shows a strong minimum of radiated energy to the west, at about 250^o, and a slight peak to the east, near ~90^o. The other azimuthal directions show fairly constant radiated energy. The rupture started in the south, with a concentration of slip near the epicenter, and the moved to the north with another concentration of high slip. The minimum in radiated energy to the west is in the trench-ward direction, and is similar to the trend seen in the Tohoku-Oki energy distribution. Our Haskell line model consists of a source along strike to 20^o and dip 15^o with much of the total moment (1.1x10^{22} Nm), rupturing at 3.5 km/s. This source is 175 km long, the length of the high slip area, and is consistent with the overall rupture pattern towards the north. Although we do not expressly see evidence in the slip models of a second source, we add one in the down dip direction at 100^o with the same rupture velocity, 7x10^{21} Nm of moment and of length 80 km, the down-dip width of rupture. The sum of these fits the azimuthal distribution of radiated energy very well, but a temporal slip distribution is necessary to explain our modeled line source.

Both the Nias 2005 M_w *8.7* and Benkulu 2007 M_w *8.5* earthquakes show weaker azimuthal variation in radiated energy, perhaps due to their smaller size. The Nias earthquake consisted of bilateral rupture, to the north at 330^o and to the south at 150^o. We see peaks in radiated energy in these two directions, with a stronger peak to the south, which may represent the larger slip patch in the southern portion. We model the Nias 2005 earthquake with two line sources along strike to the north, and to the south, to represent the bilateral rupture. We give the southward propagating source slightly more moment, 6x10^{21} Nm, than the northern source, 5x10^{21} Nm. Each has a length of 75 km, to sum to represent the total 150 km of concentrated slip, a dip of 15^o, and rupture velocity of 3.5 km/s. This two source, bilateral rupture models the observed pattern of radiated

energy quite well, and captures the larger amplitude of energy radiated to the south with the varied moments of the sources.

The Bengkulu rupture also occurred in two distinct south and north patched, but with rupture direction to the north only. In the radiated energy, we can only resolve a broad peak in the northerly direction. We show two Haskell line sources with the same strike, 300^o, dip 15^o, and direction of motion to the north at a rupture velocity of 2.5 km/s, each with half of the moment, 2.2×10^{21} Nm, to represent the two rupture patches. This model shows peaks in the energy to the north, but it is hard to resolve this pattern in our data.

Overall, we can distinguish general source rupture characteristics from the radiated energy. The larger events, with more complex rupture patterns, show stronger azimuthal variation. Our superimposed Haskell line sources explain the directivity we observe very well. When paired with a time dependent slip inversion, we can interpret the maxima and minima in energy as particular rupture processes. *Venkataraman and Kanamori* [2004] conclude that directivity for dip-slip events with rupture propagating along strike is less than a factor of two at teleseismic distances. However, even for the Nias 2005 and Bengkulu 2007 events, which show the smallest directivity, we see at least a factor of two difference in the radiated energy. *Favreau and Archuleta* [2003] forward modeled the energy radiated by the 1979 Imperial Valley earthquake, and found extreme directivity from a super shear rupture, showing 86% of the energy radiating in the strike direction. The Sumatra 2004, which does propagate along strike, shows nearly an order of magnitude difference of energy from station to station. Therefore, it is essential to take directivity into account when estimated radiated energy teleseismically. With our method, we calculate energy at many stations, and take an azimuthally weighted average to account for the directivity.

5.6 Limitations on Choice of Empirical Green's Function

In the Nias 2005 M_w *8.7* and Bengkulu 2007 M_w *8.5* data sets, we consider up to 14 possible eGf events each, ranging from as small as M_w *6.0* to as large as M_w *7.8,* with normal and strike-slip mechanisms, as well as thrust events that match the mechanism of

the mainshock. The locations are also more widespread over the fault plane. We use these data sets to test the limitations on choice of eGf. For the events considered, the $\log_{10}$ standard deviation of the mainshock energy between different eGf events is 0.25 (Nias 2005) and 0.40 (Bengkulu 2007). With just the chosen eGf events, shown in Tables 5.4 and 5.5, the $\log_{10}$ std drops to 0.14 and 0.09, showing that the correct choice of eGf events give much more stable and reliable mainshock energies.

We find that anything less than ~M 6.5 is too small. Energy results as corrected by these eGfs are systematically smaller than the average (Figure 5.20). Events of this size have peak amplitudes near 10^{-6} m/s (vertical) at teleseismic distances, and corner frequencies near 0.1 Hz. Microseismic noise has a peak at 8 seconds, with a median amplitude of about $3x10^{-7}$ m/s [*Aster et al*, 2008], and hence the amplitudes of eGfs of M <~6.5 are close to the microseismic background noise, and may display artificially elevated amplitudes. When these events are used as eGfs, the corrected mainshock spectrum has a bias towards low amplitudes in the microseismic band, and hence lower estimates of radiated energy.

On the other hand, we consider events as large as M_w *7.8 – 7.9* as potential eGf. A typical rule of thumb for choosing an appropriate eGf is a magnitude separation of 1.5 units between the mainshock and eGf [e.g. *Courboulex et al.,* 1996; *Hough*, 2001; *Kane et al.,* 2011]. In the case of the Nias 2005 M_w *8.7*, we find that the largest potential eGf (M_w 7.8 2010/04/06) is too large to be used as an eGf for this event, with a magnitude difference of only 0.9. For Bengkulu 2007 M_w *8.5*, we consider an eGf of M_w *7.8*, a magnitude separation of 0.7 units, and find that using this event for deconvolution it gives higher than average mainshock energies (Figure 5.20). Our teleseismic eGf deconvolution method is very sensitive to relative spectral amplitudes, and it is possible for the large eGfs to have amplitudes nearly as high, or higher, as the mainshock at some frequencies, which leads to unstable radiated energy estimates.

To test the eGf assumptions, we also consider potential eGfs with different mechanisms and locations. Overall, mainshock energies corrected by eGfs of similar location and mechanism have much smaller inter-station standard error, shown by error

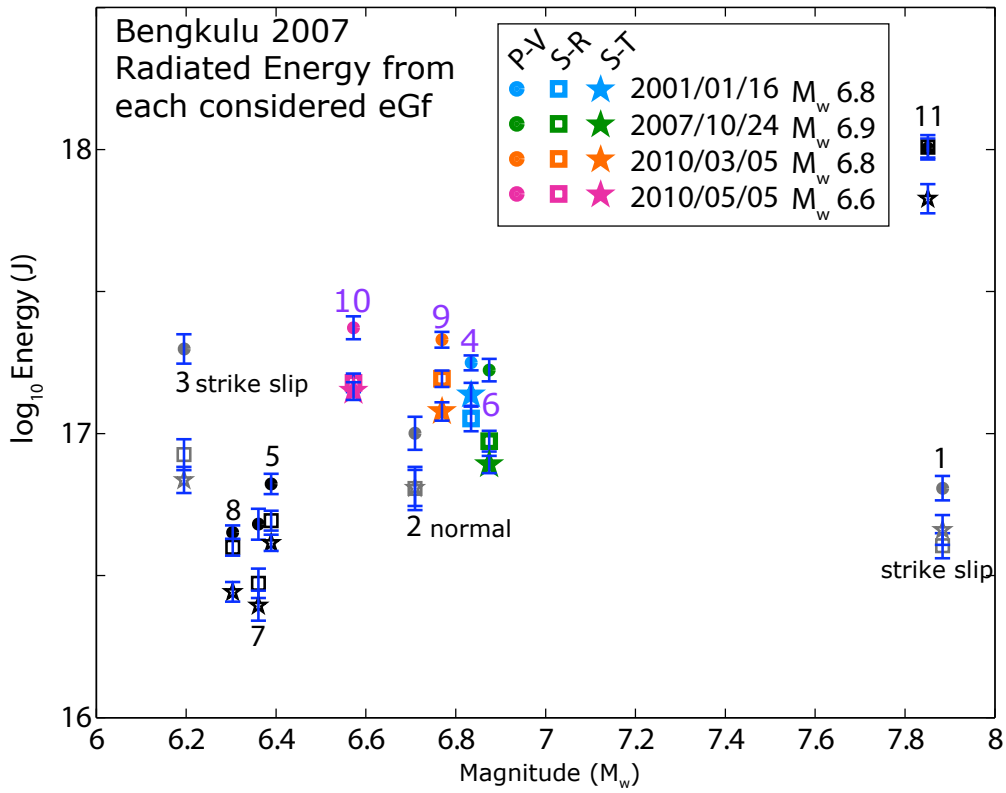

Figure 5.20 3-components of radiated energy of the Bengkulu Mw 8.5 mainshock, as measured by 11 different considered eGfs. Shown in colors are the 4 eGf's used in the analysis. Estimates from each of three components are shown in different symbols (P-wave vertical in circles; S-wave radial in squares; and S-wave transverse in stars) and blue bars show standard error of the estimate using interstation standard deviation. Events 1 and 11, ~M 7.9, are too large to be used as eGf's for this Mw 8.5 event; the magnitude separation is only 0.6, much smaller than the accepted ~1.5 magnitude units. Event number 2 is discarded due to its opposite (normal) mechanism. Events 3, 5, 7 and 8 are too small, and hence underestimate the mainshock energy. In most cases, the P wave gives slightly higher radiated energy estimates, but all three components yield similar estimates.

bars in Figure 5.20. These are the events considered in the final analysis. While on average, eGfs with normal sense of motion estimate mainshock energies consistent with the average, the azimuthal distribution of energies is much more variable. Strike-slip eGfs yield highly variable estimates of mainshock energy as compared to the other events. Corrected mainshock spectra are poorly determined and also highly variable, yielding unstable estimates of energy. EGFs with mechanisms consistent with that of the mainshock are able to estimate radiated energy robustly. In the Nias 2005 sequence, we test a M_w *6.8* with a very similar mechanism to that of the mainshock, but located much closer to the trench and nearly 150 km from the area of high slip. Mainshock energy estimated using this eGf has the highest inter-station standard error of any considered

eGf. We find that eGfs close to the epicenter (within ~100 km) yield energy estimates with much less variation between *P* and *S* components, as well as smaller interstation standard error. A radius of validity, within which eGfs are most stable for deconvolution, is thus set at ~100 km. These observations support the necessity of using eGfs with similar mechanisms to the mainshock and locations close to the areas of high slip.

5.7 Real-Time Determination of Radiated Energy

Given a standard magnitude difference of 1.5 magnitude units between the eGf and the mainshock and our found-lower limit of about M 6.5, we surmise that the smallest earthquake that could be studied teleseismically with this method is about ~M 8.

Figure 5.21 shows the distribution of magnitude 6.5 and greater earthquakes globally over the past 20 years. Each earthquake is shown as a circle of radius 100 km, which we found to be the most effective range of eGf events for mainshock deconvolution. Hence, any mainshock located within any 100km radius circle could be studied with the developed method, using the associated eGf. There is coverage of most of the world's subduction zone, where we expect large and devastating earthquakes to occur.

We propose that a global eGf database could be set up to assist in rapid radiated energy estimation of larger, more hazardous earthquakes. Potential eGf earthquakes, as shown in Figure 5.21, recorded at reliable GSN stations will be prescreened and preprocessed (quality checked, windowed and tapered) and their 3-component spectra stored in the database. Future large earthquakes that occur within 100 km of an eGf in the database can quickly be analyzed.

In our study, many of the potential eGf events occurred before the mainshock. There is dense coverage of $M_w > 6.5$ earthquakes along most of the world's subduction zones, where we expect future hazardous earthquake to occur, including all great earthquakes such as studies here. A large percentage of the total subduction zone length is covered. There is also good coverage in areas such as the Mediterranean, San Andreas fault system, and the Himalayan system. All of these global earthquakes could be considered potential eGfs and would be implemented into the database.

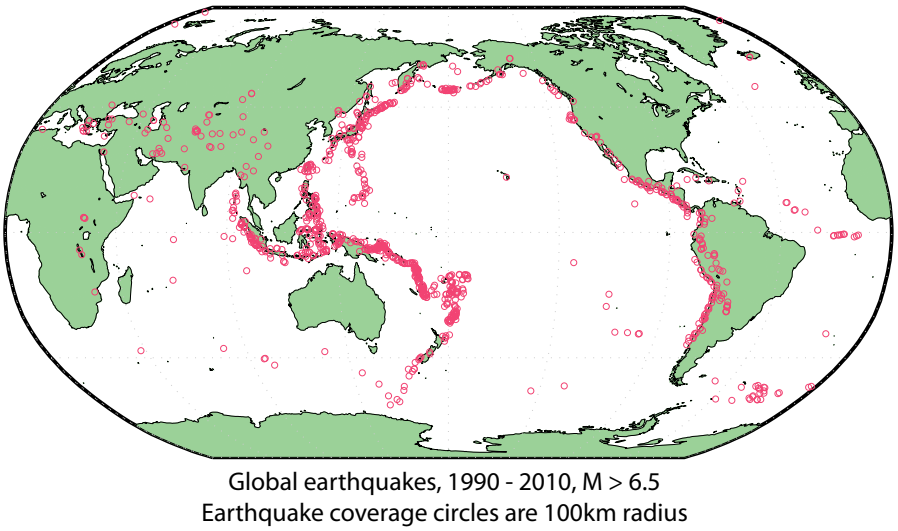

Figure 5.21 Global earthquakes > M6.5 from the past 20 years. Each earthquake is shown as a circle of radius 100 km, which we find to be the approximate radius of influence of eGf events. Mainshocks occurring within a circle can be corrected by eGf deconvolution.

Once a large earthquake occurs, it could quickly be located and matched up with appropriate eGf events. The method to estimate energy is not computationally intensive, so the mainshock energy could be determined rapidly. Most of the manual work is in screening the potential eGf events and determining their parameters, which would all be accomplished before a mainshock event occurs, cutting back significantly on the processing time.

The radiated energy could be calculated within a few minutes of the arrival of waveforms at a station. For the closest GSN stations considered here at 30^{o} distance, *P* waves first arrive 6 minutes after rupture begins, and *S* waves start to arrive at about 12 minutes. We have shown that there is no dependence of estimated energy on station distance, so that the closest stations could reliably be used, but for redundancy, at least 6 stations should be used for the estimation. A directivity correction is necessary, but is taken care of if stations are distributed evenly azimuthally. Furthermore, since energy estimated from *P* and *S* waves is consistent, the estimation could be performed in real time using only the *P* arrivals. Because energy even for very large source regions (Sumatra 2004) or very compact regions (Tohoku 2011) can be determined, this method

can be used for any large global event. Thus, an estimate of radiated seismic energy could be calculated within ~10 minutes of event occurrence.

Newman and Okal [1998] defined a tsunami discrimination parameter, $\Theta = log_{10} E_R/M_o$, finding that "tsunami earthquakes" have an anomalously low ratio of radiated energy to seismic moment. Real time determination of Θ could indicate if an earthquake will generate unusually large tsunami amplitude within ~10 minutes of occurring, as reasoned above. Tsunami are generated at the shallowest part of rupture, at the trench, which is typically 100 – 200 km off shore, so even local tsunami take about 30 minutes to reach the nearest shore. Using this method for quick tsunami determination would yield approximately 20 minutes for evacuation or early warning functions. Furthermore, the azimuthal energy dependence may quickly inform the rupture model and directivity, which could also aid in rapid hazard characterization.

Newman et al. [2011] have also developed a method for fast determination of the Θ parameter; tsunami warning from this information is not yet implemented. Moreover, this method is dependent on specific knowledge of the mainshock depth, location and mechanism. While the teleseismic eGf deconvolution requires independent knowledge of the mainshock moment, it is not dependent on the exact location or mechanism, only approximate source characteristics, so that an appropriately located eGf, with similar mechanism, can be chosen.

Radiated seismic energy is a fundamental earthquake source parameter. Rapid determination of earthquake energy could aid in other hazard mitigation efforts or deployment of emergency response teams. During the 2011 Tohoku-Oki earthquake, the Japanese early warning and information systems worked well, as many Japanese were warned of ground shaking and tsunami waves before the arrived. However, *Yamada* [2011] noted that although the system worked well, more accurate, quick determination of source parameters would increase the efficacy of all of the systems. No other country in the world is as earthquake or tsunami prepared as Japan, yet the Tohoki-Oki 2011 earthquake still caused massive destruction. Because large earthquakes, such as 2011 Tohoku-Oki with its compact source and dual rupture style, and the 1300 km long 2004

Sumatra event, are not easily characterized simply by moment, knowledge of radiated energy and apparent stress of these events can aid in rapid source assessment.

5.8 Conclusions

We find that radiated energy of five great earthquakes is consistent with self-similar source physics. The scaled energy of each event is in the range $1 – 2x10^{-5}$, and apparent stress ranges from 0.4 to 0.8 MPa. These values are very consistent with those found for a wide range of events, from micro-earthquakes to other subduction zone megathrusts. Our estimates of radiated energy for each event are very similar to those of other researchers, within a factor of 3 to those of Newman and Kanamori, though careful consideration of parameter choices and station averaging may account for the small differences that still remain.

We develop a new teleseismic empirical Green's function deconvolution approach, using eGf events as large as M_w *7.4,* which is likely the largest eGf event ever used in a deconvolution analysis. We show that both *P* and *S* waves can be used in the eGf deconvolution teleseismically to give consistent energy estimates, whereas before, only *P* waves were used teleseismically [e.g. *Boatwright and Choy*, 1986].

We showed that teleseismic eGf deconvolution is robust for removing path and site effects using both *P* and *S* waves, to measure radiated seismic energy. EGF deconvolution could thus be used in other applications to isolate source spectra or time series. *Ide et al.* [2011] used teleseismic eGf deconvolution to invert for a spatio-temporal slip distribution of the Tohoku-Oki 2011 earthquake, and this method could be applied to the great earthquakes we have analyzed as well.

The azimuthal distribution of radiated energy is generally consistent with the sense of rupture propagation for each earthquake. The larger events, which may be inherently more complicated, show stronger and more varied directivity in energy, which can be interpreted as high apparent velocity along the trench, and slow rupture in the direction towards the trench. The smaller events do still show some azimuthal dependence of energy, so that directivity effects should be considered when teleseismically estimating

radiated energy. Further work to couple time dependent rupture propagation with the energy pattern may further highlight source characteristics of megathrusts.

Data and Resources

Broadband velocity data were collected through Standing Order of Data (SOD), which also preprocessed the data to remove instrument response and transfer to displacement. SOD is available at http://www.seis.sc.edu/SOD/ [*Owens et al.*, 2004].

Acknowledgements

We thank Jesse Lawrence for help with downloading the GSN data and use of SOD, as well as general teleseismic data help.

References

Ammon, C. J., A. A. Velasco and T. Lay (1993), Rapid estimation of rupture directivity: application to the 1992 Landers (M_S=7.4) and Cape Mendocino (M_s=7.2), California earthquakes, *Geophy. Res. Lett., 20*(2), 97-100.

Ammon, C. J., C. Ji, H.-K. Thio, D. Robinson, S. Ni, V. Hjorleifsdottir, H. Kanamori, T. Lay, S. Das, D. Helmberger, G. Ichinose, J. Polet and D. Wald (2005), Rupture Process of the 2004 Sumatra-Andaman Earthquake, *Science,* 308 (5725), 1133-1139. [DOI:10.1126/science.1112260].

Aster, R. C., D. E. McNamara, and P. D. Bromirski (2008), Multidecadal climate-induced variability in microseisms, *Seismo. Res. Lett.*, 79(2):194-202.

Baltay, A., G. Prieto and G. C. Beroza (2010), Radiated seismic energy from coda measurements and no scaling in apparent stress with seismic moment. *J. Geophys. Res*. **115**, B08314 (2010).

Baltay, A., S. Ide, G. Prieto, and G.Beroza (2011), Variability in earthquake stress drop and apparent stress, *Geophys. Res. Lett., 38,* L06303, doi:10.1029/2011GL046698.

Banerjee, P., F. F. Pollitz, and R. Burgmann (2005), The size and duration of the Sumatra-Andaman earthquake from far-field offsets, *Science, 308*, 1769-1772.

Billham, R. (2005), A flying start, then a slow slip, *Science, 308*, 1126-1127.

Boatwright, J. and G. Choy (1986), Teleseismic estimates of the energy radiated by shallow earthquakes, *J. Geophys. Res., 91*, 2095-2112.

Choy, G., A. McGarr, S. Kirby and J. Boatwright (2006) An overview of the global variability in radiated energy and apparent stress, in *Earthquakes: radiated energy and the physics of faulting,* Geophysical Monograph Series, 170, 43-57, doi:10.1029/170GM10.

Convers, J. A., and A. V. Newman (2011), Global evaluation of large earthquake energy from 1997 through mid-2010, *J. Geophys. Res*., 116, B08304, doi:10.1029/2010JB007928

Courboulex, F., Virieux, J., Deschamps, A., Gibert, D. and Zollo, A. (1996), Source investigation of a small event using empirical Green's functions and simulated annealing. Geophysical Journal International, 125: 768–780. doi: 10.1111/j.1365-246X.1996.tb06022.x

Dean, S.M., L. C. McNeill, T. J. Henstock, J. M. Bull, S. P. S. Gulick, J. A. Austin, Jr., N. L. B. Bans, Y. S. Djajadihardja and H. Permana (2010*)*, Contrasting decollement and prism properties over the Sumatra 2004–2005 earthquake rupture boundary, *Science*, **329**, 207–210.

Favreau, P. and R. J. Archuleta (2003), Direct seismic energy modeling and application to the 1979 Imperial Valley earthquake, *Geophy. Res. Lett., 30*(5) 1198, doi:10.1029/2002GL015968.

Hanks, T. C., and W. Thatcher (1972), A graphical representation of seismic source parameters, *J. Geophys. Res. 77*, 4292-4405.

Haskell, N. A. (1964) Total energy and energy spectral density of elastic wave radiation from propagating faults, *Bull. Seismol. Soc. Am*., 56, 1, 125-140.

Hayes, G. (2010) *Finite Fault Model. Updated Result of the Feb 27, 2010 Mw 8.8 Maule, Chile Earthquake*. http://earthquake.usgs.gov/earthquakes/eqinthenews/2010/us2010tfan/finite_fault.php, (US Geological Survey/NEIC, 2010)

Hough, S. E. (2001), Empirical Green's function analysis of recent moderate events in California, *Bull. Seismol. Soc. Am., 91*, 456 – 467.

Ide, S., and G. C. Beroza (2001), Does apparent stress vary with earthquake size?, *Geophys. Res. Lett.*, *28*(17), 3349.

Ide, S., G. C. Beroza, S. G. Prejean, and W. L. Ellsworth, Apparent break in earthquake scaling due to path and site effects on deep borehole recordings, *J. Geophys. Res.,* 108(B5), 2271, doi:10.1029/2001JB001617, 2003

Ide, S., A. Baltay and G. C. Beroza (2011), Shallow dynamic overshoot and energetic deep rupture in the 2001 M_w 9.0 Tohoku-Oki Earthquake, *Science*, 332, 6036, 1426-1429 DOI: 10.1126/science.1207020

Kanamori, H. (1972), Mechanism of tsunami earthquakes, *Phys. Earth Planet. Interiors* 6, 346 – 359.

Kanamori, H. and J. Given (1981), Use of long-period surface waves for rapid determination of earthquake-source parameters. *Phys. Earth Planet. Inter.* 27, 8.

Kanamori, H. (2006), The radiated energy of the 2004 Sumatra-Andaman earthquake, in *Earthquakes: radiated energy and the physics of faulting,* Geophysical Monograph Series, 170, 59-68, doi:10.1029/170GM10.

Kanamori, H. (2011) *pers. comm.* November 6, 2011.

Kane, D. L., G. A. Prieto, F. L. Vernon, and P. M. Shearer (2011), Quantifying seismic source parameter uncertainties, *Bull. Seism. Soc. Am., 101*, 535-543.

Konca, O. (2007), Updated results, 05/03/28 (Mw 8.5) Sumatra Earthquake, Caltect, http://www.tectonics.caltech.edu/slip_history/2005_sumatra/sumatra_update2.html, Accessed November 11th, 2011.

Konca, A.O., V. Hjorleifsdottir, T-R. A. Song, J.-P. Avouac, D. V. Helmberger, C. Ji, K. Sieh, R. Briggs, and A. Meltzner (2007), Rupture kinematics of the 2005 Mw 8.6 Nias-Simeulue earthquake from the joint inversion of seismic and geodetic data (in The 2004 Sumatra-Andaman earthquake and the Indian Ocean tsunami), *Bull. Seismol. Soc. Am.*, 97(1A):S307-S322.

Konca, A. O., J-P Avouac, A. Sladen, A. J. Meltzner, K. Sieh, P. Fang, Z. Li, J. Galetzka, J. Genrich, M. Chlieh, D. H. Natawidjaja, Y. Bock, E. J. Fielding, C. Ji and D. V. Helmberger (2008), Partial rupture of a locked patch of the Sumatra megathrust during the 2007 earthquake sequence, *Nature*, 456 doi:10.1038/nature07572.

Lay, T., H. Kanamori, C. J. Ammon, M. Nettles, S. N. Ward, R. C. Aster, S. L. Beck, S. L. Bilek, M. R. Brudzinski, R. Butler, H. R. DeShon, G. Ekstrom, K. Satake, and S. Sipkin (2005). The great Sumatra- Andaman earthquake of 26 December 2004, *Science* **308 ,**1127 – 1133.

Moreno, M., M. Rosenau and O. Oncken (2010), 2010 Maule earthquake slip correlates with pre-seismic locking of Andean subduction zone, *Nature* 467, 198–202 doi:10.1038/nature09349

Newman, A. V., Feng, L., Fritz, H. M., Lifton, Z. M., Kalligeris, N. and Wei, Y. (2011), The energetic 2010 M_W 7.1 Solomon Islands tsunami earthquake. *Geophys. J. Int.*, 186: 775–781. doi: 10.1111/j.1365-246X.2011.05057.x.

Newman, A. V., and E. A. Okal (1998), Teleseismic estimates of radiated seismic energy: The E/M_0 discriminant for tsunami earthquakes,*J. Geophys. Res.*, *103*(B11), 26,885–26,898, doi:10.1029/98JB02236.

Newman, A. V., G. Hayes, Y. Wei, and J. Convers (2011), The 25 October 2010 Mentawai tsunami earthquake, from real‐time discriminants, finite‐fault rupture, and tsunami excitation, *Geophys. Res. Lett*., 38, L05302, doi:10.1029/2010GL046498.

Newman, A. (2011) Real-Time Earthquake Energy and Rupture Duration Determinations, http://geophysics.eas.gatech.edu/anewman/research/RTerg/2011/11031100/, Accessed November 6, 2011.

Owens, T.J., H. P. Crotwell, C. Groves, and P. Oliver-Paul (2004), SOD: Standing Order for Data. *Seismol. Res. Lett.*, 75:515–520.

Perez-Campos, X., S. K. Singh and G. C. Beroza (2003) Reconciling teleseismic and regional estimates of seismic energy, *Bull. Seismol. Soc. Am. 95*(5), 2123 – 2130.

Venkataraman, A., L. Rivera, and H. Kanamori (2002), Radiated energy from the 16 October 1999 Hector Mine earthquake: Regional and teleseismic estimates, *Bull. Seismol. Soc. Am*., 92, 1256–1265, doi:10.1785/0120000929.

Venkataraman, A. and H. Kanamori (2004), Effect of directivity on estimates of radiated seismic energy, *J. Geophys. Res., 109*, B04301, doi:10.1029/2003JB002548.

Wyss, M. (1970), Stress estimates for South American shallow and deep earthquakes, *J. Geophys. Res.*, *75*(8), 1529-1544, doi:10/1029/JB075i008p01529.

CHAPTER 6

Conclusion

While we may never know the true source characteristics of an earthquake, more precise estimates of earthquake source parameters yield a better quantitative knowledge of earthquake physics. Radiated energy and stress measurements can be directly related to fault slip, fracture energy, rupture velocity and other basic quantities that can help us understand the way earthquakes start, evolve, and arrest.

This thesis comprises a comprehensive study of precise earthquake source parameter estimation, utilizing relative spectral measurements to negate path and site effects, and also investigates the limitations of measurements that do not make attenuation corrections. I find that empirical Green's functions are robust at making path and site corrections; direct measures of ground motion can also be used to estimate source parameters, but must be made at close distances, <~20 km. Otherwise, attenuation corrections are essential to precisely recover source spectra.

Throughout this thesis, I estimate several source parameters. From corrected source spectra, I am able to model seismic moment, M_o, radiated seismic energy E_R, and the corner frequency f_c. From those parameters, scaled energy E_R/M_o, the apparent stress τ_a, and Brune stress drop, $\Delta\sigma$, can be calculated. As well, by utilizing acceleration records and the corner frequency, a_{RMS} stress drop is also computed.

Seismic energy analysis using coda waves had systematically shown a dependence of apparent stress on earthquake moment. In Chapter 2, I developed a method that also makes use of coda waves, yet with many fewer assumptions and following a much simpler logic. This empirical Green's function coda approach corrects co-located earthquakes for path and site effects using a small event (~M 3) as an eGf, and still takes advantage of the averaging properties of the coda wave to create more stable spectra. I developed this method originally for earthquakes in the western US; application of the same method to Honshu, Japan required even fewer assumptions due to the availability of higher quality data with fewer inconsistencies, which I discussed in Chapter 3.

In total, I analyzed 314 earthquakes from magnitude ~2 to M_w *7.1*. I find that all of the source parameters considered follow self-similar physical models. In particular, neither apparent stress nor stress drop are dependent on magnitude, in contrast to previous studies employing the seismic coda.

In Chapter 4, I estimate earthquake stress drop directly from acceleration records, without making any path or site corrections. These estimates of stress drop measure an inherently different part of the earthquake spectrum, frequencies higher than the corner frequency. The eGf coda method, on the other hand, utilizes information in the frequency range near to the corner frequency. Stress drops for each earthquake under the two

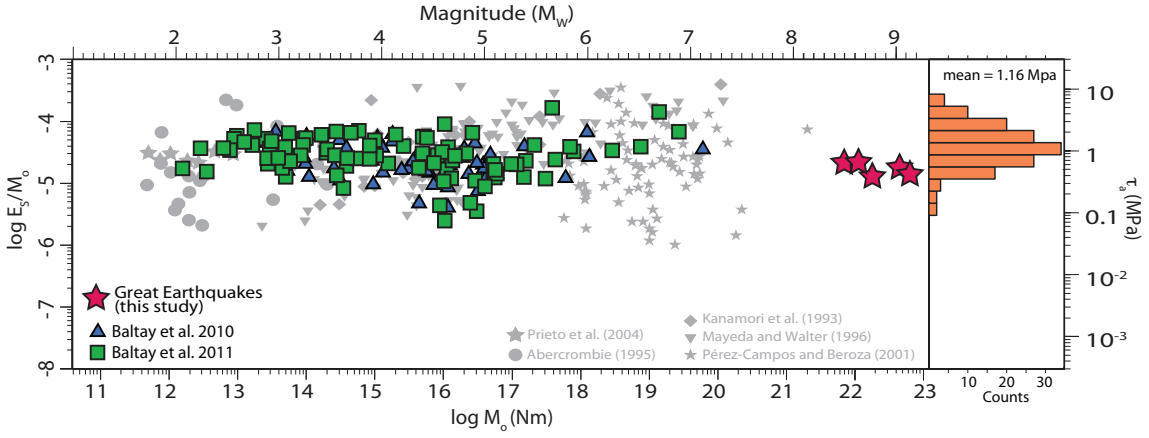

Figure 6.1 Scaled energy and apparent stress for all earthquakes studied in this thesis. Events in blue (*Baltay et al.* 2010) are from the western US, and events in green (*Baltay et al.* 2011) are from eastern Honshu, Japan. The pink stars are the five great earthquakes studied in Chapter 5 of this thesis. All are overlain on data from other studies, as compiled by *Ide and Beroza* [2001]. Histogram shows apparent stress is log-normally distributed, with a $\log_{10}$ mean of 1.16 MPa.

methods compare well, affirming that any observed variability is reflecting true source variation. The a_{RMS} stress drop is computationally and logistically simpler to calculate, as it can be determined from simple measurements on a single record, while the eGf coda method requires co-located small earthquakes and employs an iterative correction scheme. However, the a_{RMS} method cannot be used at distances greater than 20 km in Honshu, Japan, as signal is generally too attenuated at greater distances. It is possible that the distance range may be greater in less attenuating regions, such as the central and eastern United States. This study also reaffirms the inference that earthquake acceleration spectra can be considered white Gaussian noise, with a flat power spectral density, band limited in the range from the corner frequency to f_{max}, an assumption often employed in stochastic ground motion modeling.

The final chapter in this thesis develops a new method of teleseismic empirical Green's function deconvolution. At teleseismic distances, I assume that earthquakes of magnitude 6.5 – 7.5 can be approximated as circular sources with known fault dimension, estimated from a given stress drop. The eGf events are then used to correct the spectra of five great earthquakes: Tohoku-Oki 2011 M_w *9.0*; Sumatra 2004 M_w *9.1*; Maule 2010 M_w *8.8*; Nias 2005 M_w *8.7*; and Bengkulu 2007 M_w *8.5.* These eGf events are some of the largest that have ever been used in deconvolution to estimate source spectra. I show that both *P* and *S* waves can be used to estimate precise radiated seismic energy; previous teleseismic methods only employed *P* waves, but with the relative eGf technique, *S*-wave dependent estimates of energy, as expected from overall patterns of rupture, which I model with Haskell-type line sources. I also find that energy directivity should be considered when making teleseismic energy estimates, as variations between stations can be an order of magnitude.

All of the events studied in this thesis show self-similar scaling behavior, as there is no compelling evidence for a dependence of scaled energy, apparent stress or stress drop on seismic moment (Figure 6.1, 6.2). I show that both apparent stress and stress drop are log-normally distributed and independent of moment when considering the entire population of events studies. Scaled energy ranges from 2.5×10^{-6} to 1.7×10^{-4}; apparent stress from 0.09 MPa to 16.6 MPa; and stress drop from 0.11 MPa to 36.8 MPa.

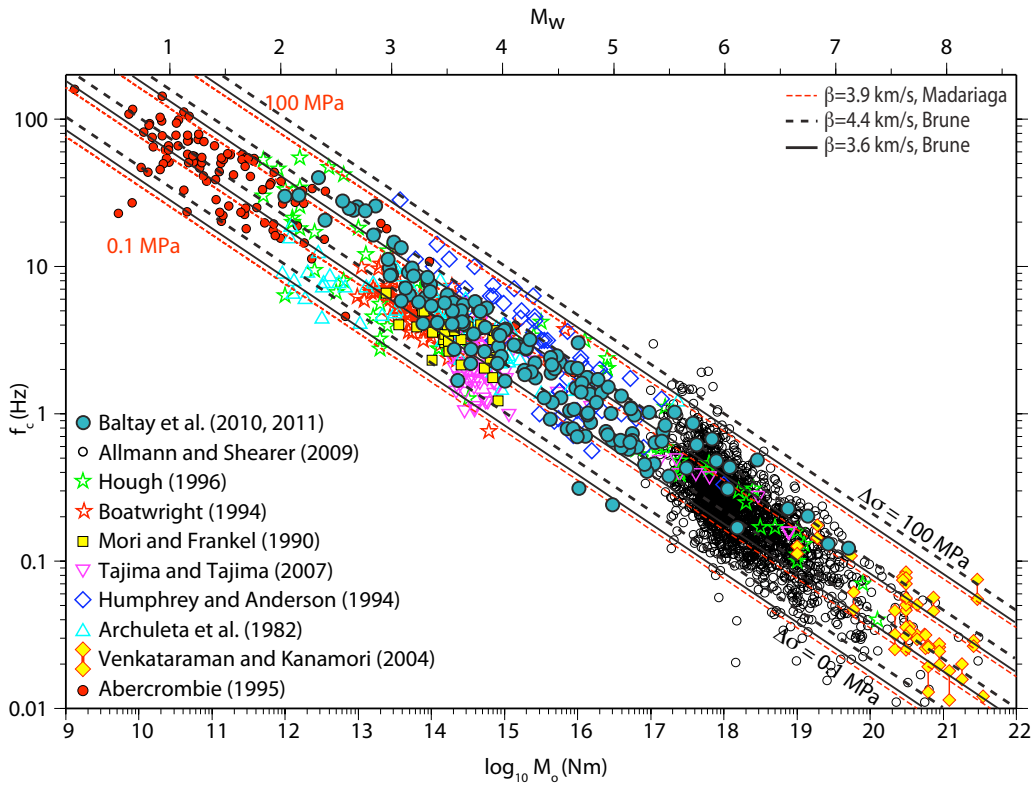

Figure 6.2 Corner frequency, f_c as a function of moment. Self similarity predicts that $f_c \sim M_o^{-1/3}$, which is shown as the dashed and solid lines, for different stress drop models. Results from this thesis are shown in turquoise circles, overlain on a compilation study by *Allmann and Shearer* [2009]. From ~M_w *0* to M_w *8*, we see that all of the events have corner frequencies consistent with a constant stress drop model, between ~1 to ~10 MPa, with very few outliers less than 0.1 MPa or greater than 100 MPa.

However, I identify several enervated and energetic earthquakes of magnitude 4 – 5 that represent statistically significant differences in energy, apparent stress and stress drop. While the majority of our events follow a constant apparent stress, the anomalous events are outside of these ranges and are not predictable simply given their moment. Further understanding of these events will be important to completely quantify their associated hazard.

Our results support an earthquake model of self-similarity, also implying that other parameters, frictional energy and rupture velocity, do not vary strongly with earthquake size. The parametric scaling relations used to predict the level of high-frequency strong ground motion for potentially damaging earthquakes are largely based on measurements from earthquakes of more modest size. In such estimates, self-similarity is assumed.

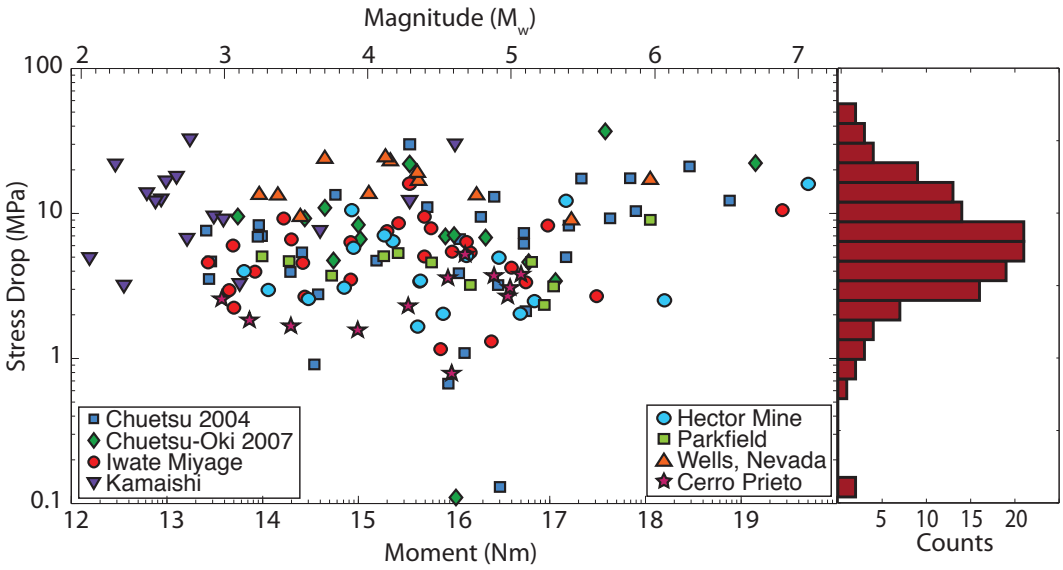

Figure 6.3 Brune stress drop measurements from the eGf coda method, for the earthquake sequences in both the western US and Honshu, Japan. Overall, I find stress drop to be log-normally distributed, with a mean near 5 MPa. Most of the events have stress drops between 1 – 10 MPa, and we observe an upperbound at about 30 MPa. The two enervated events are obvious with anomalously low stress drops.

A comparison of my apparent stress and corner frequency estimates with previous studies confirms the observation of self-similarity over the range of earthquakes studied here, from ~ M2 to M_w *9.2*. Scaled energy and apparent stress estimates are in the same range as the compiled results of *Ide and Beroza* [2001] (Figure 6.1). Corner frequencies of the events studied here are follow the same trend as those compiled by *Allmann and Shearer* [2009] for events as small as M_w *0*, up to great earthquakes of M_w *8.5*. This implies a constant stress drop for all events, shown for both the Brune and Madariaga models, for different values of β (Figure 6.2).

Mean earthquake stress drop has been typically thought to be in the range of 1 – 10 MPa [ex. *Kanamori and Anderson,* 1975]. *Thatcher and Hanks* [1973] and *Hanks* [1977] found a well-defined lower limit on stress drops of ~0.1 MPa, with an upper limit of about 20 MPa, for a population of earthquakes in southern California. *Allmann and Shearer* [2009] found stress drops to range from 0.3 MPa to 50 MPa for global earthquakes of M_w*5.2* to M_w 8.3. Our stress drop range of 0.11 MPa to 36.8 MPa is very consistent with all of these observations (Figure 6.3).

This thesis represents several contributions to the earthquake source physics field.

- I show that use of the seismic coda in local studies does not give rise to scaling of earthquake energy with moment as previous coda studies had; I find that scaled energy is constant and independent of moment. The method I developed uses many less assumptions that the previous coda methodology of *Mayeda et al.* [1996] and employs many more stations.

- I use more rigorous statistics to show independence of scaled energy on moment (Figure 2.5), including non-parametric box plots, least squares fits of E_R/M_o, and confidence intervals on those fits. I also give error bars on corner frequency and stress drop from fitting parameters (Figure 3.4). The use of many stations for each energy measurement gives a more robust estimate of the mean. In the teleseismic case, I use several different eGf events to show that while eGf choice is important, the final seismic energy is independent of specific eGf event.

- I compare stress drop to apparent stress for a large population of earthquakes, and find that the average ratio of the two is very close to the theoretical approximation.

- I revisit a_{RMS} stress drop to investigate the limits of the method which was proposed by *Hanks* [1979] and quickly adopted, but which had not been rigorously tested since *Hanks and McGuire* [1981]. Greater availability of high-quality data allows me to compare these stress drops to those found with the eGf coda method. I determine that a_{RMS} stress drop compares well to the eGf stress drop at close distances.

- I develop a new teleseismic eGf deconvolution using large eGfs of M_w *6.5 – 7.5* to estimate radiated energy of great earthquakes. This is the first teleseismic eGf deconvolution for seismic energy, and shows that we can extend the local eGf assumptions to much greater distances. I also demonstrate that both *P* and *S* waves give consistent energy estimates; previously, only *P* waves were used to determine teleseismic energy [ex. *Boatwright and Choy*, 1986].

- I model the observed azimuthal dependence of radiated energy with simple approximations of Haskell line sources, even for complex ruptures such as the Sumatra 2004 and Tohoku-Oki 2011 earthquakes. I find that even for dip-slip ruptures that propagate along strike, directivity corrections should be considered when studying seismic energy.

- I suggest that two of the developed methods can be applied to rapid source approximation: a_{RMS} method to determine stress drop or local earthquakes; and the teleseismic eGf deconvolution to estimate radiated energy of great earthquakes. Both of these methods could quickly indicate energetic, more hazardous earthquakes, or enervated, potential tsunami earthquakes.

Several areas of future investigation based on this research are possible. While stress drop is model dependent, and different formulations can lead to a difference of up to a factor of ~5 (between the Brune model and the Madariaga model), neither scaled energy nor corner frequency are model dependent. However, they can vary based on the constants assumed, such as density, shear wave velocity, and shear modulus. A complete compilation of global results needs to take model and constant parameters into consideration, and would be useful to completely understand the distribution of earthquake source parameters for different tectonic regimes, which could be implemented into ground motion prediction equations.

Although not undertaken in this thesis, stress drop and apparent stress can be related to determine the fracture energy of earthquakes [*Abercrombie and Rice, 2005*]. Other processes, such as melting, weakening, and pore pressure effects, can be constrained from fracture energy. Understanding how these small-scale phenomenon effect ruptures, and whether or not they are scale dependent can shed light onto earthquake nucleation and termination.

In Chapter 3, I determined a relationship between the moment magnitude, M_w, and the Japan Meterological Agency's magnitude, M_{JMA}. The eGf coda methodology robustly estimates relative magnitudes, between smaller earthquakes and a give independent M_w of

a larger, mainshock. Since the JMA does not compute moment magnitudes for all small earthquakes, it is possible to extend the eGf method to routinely find M_w for these events.

Both the a_{RMS} and teleseismic eGf deconvolution method could be adapted to run in near-real time, to rapidly determine earthquake source parameters. Early knowledge of how energetic an earthquake is may enhance early warning capabilities and our ability to respond to disaster. While the teleseismic eGf deconvolution cannot currently estimate corner frequency, due to the large source size of great earthquakes, the low frequency observational limit can place an upper limit on the corner frequency, which in turn puts an upper bound on stress drop, which could be useful to predict strong ground motion. Earthquakes that radiate proportionally more energy, and those with higher stress drops, cause more ground motion and are more destructive. On the other hand, tsunami earthquakes, subduction events that are deficient in radiated energy for their magnitude, can cause unusually large tsunami. The ability to quickly determine to which class an earthquake belongs could aid in determining its hazard.

References

Abercrombie, R. E. and Leary, P. C., 1993, Source parameters of small earthquakes recorded at 2.5 km depth, Cajon Pass, southern California: implications for earthquake scaling, *Geophys. Res. Lett., 20*, 1511-1514.

Abercrombie, R. E. and J. R. Rice (2005), Can observations of earthquake scaling constrain slip weakening? *Geophys. J. Int*, *162*, 406-424, doi:10.1111/j.1365-246X.2005.02579.x.

Allmann, B. P., and P. M. Shearer (2009), Global variations of stress drop for moderate to large earthquakes, *J. Geophys. Res.*, *114*(B1).

Baltay, A., S. Ide, G. Prieto, and G.Beroza (2011), Variability in earthquake stress drop and apparent stress, *Geophys. Res. Lett*., *38*, L06303, doi:10.1029/2011GL046698.

Thatcher, W., and T. C. Hanks (1973), Source parameters of southern california earthquakes, J. Geophys. Res, 78, 35, 8547 – 8676

Hanks, T. C. (1977), Earthquake stress drops, ambient tectonic stresses and stresses that drive plate motions, in *Pure and Applied Geophysics*, vol. 115, pp. 441-458-458, Birkhäuser Basel.

Hanks, T. C., and R. K. McGuire (1981), The character of high-frequency strong ground motion, *Bull. Seism. So. Am., 71*, 2071-2095.

Ide, S., and G. C. Beroza (2001). Does apparent stress vary with earthquake size?, *Geophys.Res. Lett.,* 28, 3349-3352.

Kanamori H., and D. L. Anderson (1975), Theoretical basis of some empirical relations in seismology, *Bull. Seism. Soc. Am., 65,* 1073-1096.

Mayeda, K., and W. R. Walter (1996), Moment, energy, stress drop, and source spectra of western United States earthquakes from regional coda envelopes, *J. Geophys. Res., 101*(B5), 11195 – 11208.